Moein Mohammadi

Cloud Microphysical Measurements with Shadowgraph Imaging Technique

Submitted to Scientific Council of Physical Sciences Discipline
in fulfillment of the requirements for the degree of
Doctor of Philosophy

Supervisor:
Prof. dr hab. Szymon P. Malinowski

Institute of Geophysics, Faculty of Physics
University of Warsaw

Warsaw 2022

Acknowledgements

Foremost, I would like to express my sincere gratitude to my advisor Prof. Szymon Malinowski for the continuous support of my PhD study and research, for his patience, motivation, enthusiasm, and immense knowledge. His guidance helped me in all the time of research and writing of this thesis.

Besides, I would like to specially thank my friend and colleague, Dr. Jakub L. Nowak, with whom I had the closest collaboration during this study. He is always willing to share his knowledge and ideas, as well as offer assistance. I also appreciate all help and supports I received during my research from other colleagues: Dr. Wojciech Kumala, Dr. Marta Wacławczyk, Dr. Krzysztof Markowicz, and Katarzyna Nurowska from Institute of Geophysics, University of Warsaw (IGF-UW); Dr. Jan Moláček, Dr. Guus Bertens, and Dr. Gholamhossein Bagheri from Max-Planck Institute for Dynamics & Self-Organisation (MPI-DS); and Dr. Till Rehm from Schneefernerhaus environmental research station (UFS).

My research was supported by the European Union's Horizon 2020 research and innovation programme under the Marie Skłodowska-Curie Actions (COMPLETE (grant agreement no. 675675)).

I also thank my other fellows at IGF-UW: Emmanuel, Dongxiang, Kasia, Piotr, Daniel, Robert, Stanisław, and Grzegorz. Special appreciation to Małgosia who kindly supported me with language editing.

Last but not least, I would like to thank Karolina for her assistance with the abstract and, more importantly, for her constant spiritual support throughout the whole period of writing this thesis.

Statement of Originality

I hereby confirm that the content of this thesis is composed by myself. The work presented herein is my own except where explicitly stated otherwise. I distinctly indicate the presence of all materials I quote from other sources, including any diagrams, charts, tables, or graphs. Moreover, all paraphrased materials are indicated with appropriate references. This thesis has not been published/submitted to any other university or institution.

My colleagues and I conducted a series of laboratory and field studies with a shadowgraph instrument, VisiSize D30, to collect the data presented in this dissertation. Laboratory experiments explained in chapter 3 were conducted by me. My colleague, J. L. Nowak, performed another series of lab tests which was briefly explained in Appendix A. The in situ measurements presented in chapter 4 were conducted by me together with G. Bertens, J. Molacek and W. Kumala. I was mainly in charge of data collection with the VisiSize D30 during the course of measurements. Moreover, I performed in situ measurements of raindrops and precipitation particles described in chapter 5.

I conducted the data analysis in collaboration with J. L. Nowak and under supervision of S. P. Malinowski. All analyses and interpretations provided in chapters 3, 4 & 5 are carried out by myself. However, I briefly mentioned J. L. Nowak's work in Appendices A & B.1, since I used those results later in my analyses.

Part of this research was published in articles below, where I played a signific ant role reflected in the author contributions statement of the articles:

- Nowak*, J. L., Mohammadi*, M., & Malinowski, S. P. (2021). Applicability of the VisiSize D30 shadowgraph system for cloud microphysical measurements. *Atmospheric Measurement Techniques*, 14(4), 2615-2633. (*co-first authors)

  Author contributions. JLN, MM and SPM designed the study. JLN planned and carried out the detection experiment (Sect. 3). MM planned and carried out the sizing experiment (Sect. 4). MM carried out the field experiment, while MM and JLN analyzed the collected data. JLN and MM wrote the manuscript with contributions from SPM.

- Mohammadi, M., Nowak, J. L., Bertens, G., Molacek, J., Kumala, W., & Malinowski, S. P. (2022). Cloud microphysical measurements at a mountain observatory: comparison between shadowgraph imaging and phase Doppler interferometry. *Atmospheric Measurement Techniques*, 15(4), 965-985.

  Author contributions. SPM conceptualized the research. MM, GB, JM and WK performed the measurements during the campaign. MM and JLN analyzed and interpreted the collected measurement data. MM wrote the original manuscript with contributions from JLN, GB, JM and SPM.

In addition, the below article about precipitation measurements with the VisiSize D30 was recently accepted for publication:

- Mohammadi, M., Nowak, J. L., & Malinowski, S. P. (2022). Microphysical measurements of hydrometeors using shadowgraph imaging technique. *J. Phys.: Conf. Ser.* [Accepted].

The materials presented in the above publications are expanded with additional details here. I did not quote these articles explicitly within the thesis, However, at the beginning of each chapter, a description was provided explaining which sections were already included in the papers.

Abstract

Deficiency in understanding some key cloud-related processes is the major source of uncertainty in weather prediction, climate science, and atmospheric circulation modeling. Clouds are predominantly composed of water droplets. The size distribution of these droplets is a crucial parameter for quantitative microphysical characterization of clouds. It is indispensable for studying cloud lifetimes, radiative effects, and precipitation formation.

The in situ measurements are crucial for cloud microphysical research as they provide direct experimental access to individual droplets in a given sample volume. Shadowgraph imaging stands out as a relatively inexpensive yet highly effective optical method for in situ sampling of hydrometeors. It performs direct measurements of particles/droplets by capturing shadow images of them.

In this study, a commercial shadowgraph instrument, VisiSize D30 (hereafter called "VisiSize"), originally designed for characterization of industrial sprays, was adapted to in situ atmospheric measurements. The cloud microphysical properties, such as the droplet size distribution (DSD), droplet number concentration (DNC), and liquid water content (LWC) were measured by the VisiSize.

First, a series of laboratory tests were conducted using polydisperse cloud-like water droplets. A suitable correction method was developed to improve estimations of droplet number concentration and size distribution. The minimum droplet diameters providing uniform detection were obtained. Then, the sizing accuracy of VisiSize was verified using a monodisperse droplet generator while the effects of collisions and evaporation of generated droplets

were also observed during the lab experiments.

Next, a series of field experiments were performed at Umweltforschungsstation Schneefernerhaus (UFS), an environmental research station in the German Alps. While turbulent orographic clouds were passing the UFS, the VisiSize was measuring the size and velocity of cloud droplets together with a Phase Doppler Interferometer (PDI) device. A comparison of the results after applying modifications to the built-in software algorithms showed a reasonable agreement regarding the droplet sizing and velocimetry between VisiSize D30 and PDI for diameters larger than 13 µm. However, discrepancies were observed concerning the droplet number concentration results, especially in smaller sizes. Further investigation by applying appropriate filters to data has allowed the attribution of discrepancies to two phenomena; different optical performance of the sensors regarding small droplets, and high turbulent velocity fluctuations relative to the mean flow, which results in an uncertain estimate of the volume of air passing through the PDI probe volume.

Finally, the VisiSize was utilized alongside an optical laser disdrometer, "OTT Parsivel^2", to perform simultaneous precipitation measurements during different weather events in Warsaw. Disdrometers, as the common tools for measuring DSD of rainfall, face serious challenges in the drizzle mode (small drop size ranges). The capability of VisiSize to accurately measure a broad range of droplet sizes, especially drizzle drops, was used to prevent the DSD truncation and acquire more precise results.

In general, the VisiSize D30 shadowgraph instrument was successfully applied to cloud microphysical measurements. It performed satisfactorily under windy, cloudy, and humid weather conditions. Moreover, it could be shown that the VisiSize, itself, can not only be used for direct measurement of hydrometeors, but also can be considered as a reliable tool to verify new droplet/particle sizing systems in atmospheric physics.

Streszczenie

Niedostatki w zrozumieniu niektórych procesów fizyki chmur sa główna przyczyna problemów zwiazanych z trafnościa prognoz pogod, klimatu i z modelowaniem cyrkulacji atmosferycznej. Chmury składaja sie przede wszystkim z kropel wody, których rozkład wielkości jest kluczowym parametrem ilościowej charakterystyki mikrofizycznej chmur, niezbednym do badania czasu ich życia, efektów radiacyjnych i formowania sie opadów.

Pomiary in situ maja w tym kontekście kluczowe znaczenie dla badań, ponieważ zapewniaja bezpośredni wglad w strukture i rozmiary kropel w danej objetości chmury. Obrazowanie cieniem (Shadowgraph imaging) wyróżnia sie jako stosunkowo niedroga, ale zarazem bardzo skuteczna metoda optyczna do próbkowania hydrometeorów in situ. Pozwala wykonać pomiary czastek/kropelek na podstawie analizy obrazow cieni rzucanych przez oświetlone czastki.

W niniejszej pracy przyrzad VisiSize D30 (zwany dalej "VisiSize"), pierwotnie zaprojektowany do celów przemysłowych, został zastosowany do wykonania pomiarów atmosferycznych in situ. Umożliwiło to pomiar właściwości mikrofizycznych chmur, takich jak rozkład wielkości kropel (ang. Droplet Size Distribution - DSD), gestość kropel (ang. Droplet Number Concentration) i zawartość wody w stanie ciekłym (ang. Liquid Water Content - LWC).

W ramach pierwszego etapu badań przeprowadzono dwie serie testów laboratoryjnych z użyciem VisiSize na polidyspersyjnych i monodyspersyjnych kroplach wody. Opracowano odpowiednia metode korekcji pomiarów, aby właściwie skalibrować narzedzie i poprawić szacowanie koncentracji kropel

i rozkładu ich wielkości. W pracy oszacowana została również minimalna średnica kropel zapewniajaca ich detekcje w calym obszarze obrazowania. Dokładność pomiarów wykonanych za pomoca VisiSize weryfikowano z użyciem monodyspersyjnego generatora kropel. Uwzgledniono również skutki zaobserwowanych zderzeń i parowania kropel.

Nastepnie przeprowadzono serie eksperymentów terenowych w Umweltforschungsstation Schneefernerhaus (UFS), stacji badań środowiskowych znajdujacej sie tuż pod szczytem Zugspitze w niemieckich Alpach. Przyrzady VisiSize oraz interferometer dopplerowski (PDI) mierzyły rozmiar kropel i ich predkość w turbulentnym przepływie wewnatrz chmur orograficznych. Porównanie wyników z obu instrumentów (VisiSize i PDI), przy zastosowaniu modyfikacji w fabrycznych algorytmach oprogramowania, wykazało dobra zgodność pomiarów wielkości i predkości kropel o średnicach wiekszych niż 13 mikronów. Równocześnie zaobserwowano rozbieżności w wynikach pomiaru koncentracji kropel, zwłaszcza przy ich mniejszych rozmiarach. W toku analizy ustalono, że rozbieżności sa skutkiem wystepowania dwóch zjawisk: różnych własności optycznych czujników w odniesieniu do małych kropel oraz dużych wahan predkości turbulentnej w stosunku do średniego przepływu, co skutkowało niepewnościami w oszacowaniu objetości powietrza przechodzacego przez sondy PDI.

W ostatniej fazie badań wykorzystano VisiSize umieszczony na dachu Instytutu Geofizyki UW obok z optycznego disdrometru laserowego OTT Parsivel^{2}" do równoczesnych pomiarów czastek opadowych . Disdrometry, jakkolwiek powszechne stosowane do mierzenia DSD opadów atmosferycznych, maja ograniczona skuteczność w przypadku małych rozmiarów kropli (np. mżawki). Synchroniczne wykorzystanie VisiSize pozwoliło uzyskać bardziej precyzyjne wyniki pomiarów szerokiego spektrum rozmiarów kropel, z naciskiem na krople mżawki i poszerzyć zakres DSD podlegajacy pomiarowi.

Podsumowujac, VisiSize D30 został z powodzeniem wykorzystany do pomiarów mikrofizycznych chmur. Sprawdzał sie zadowalajaco w wietrznych, pochmurnych i wilgotnych warunkach pogodowych. Co wiecej, można było wykazać, że VisiSize może być nie tylko używany do bezpośredniego pomiaru hydrometeorów, ale także może być uważany za wiarygodne narzedzie do weryfikacji nowych systemów klasyfikacji kropel/czastek w fizyce atmosfery.

Contents

List of tables **xv**

List of figures **xvi**

1 Introduction **1**

1.1 Experimental approaches in cloud microphysics 1

1.1.1 In situ measurement methods 5

1.2 In-situ measurements at Schneefernerhaus 22

2 Instrumentation and methodology **29**

2.1 VisiSize D30 shadowgraph system 29

2.1.1 Droplet sizing 31

2.1.2 DNC calculations 37

2.1.3 Velocimetry 39

2.2 Other instruments alongside VisiSize 40

2.2.1 Phase Doppler Interferometer Probe 40

2.2.2 Laser optical disdrometer 46

3 Laboratory experiments with monodisperse droplets **49**

3.1 Experimental set-up 49

3.2 Results and discussion 51

3.3 Summary 58

4 Field measurements of cloud droplets **59**

4.1 Zugspitze measurement campaign 59

4.2 Results and discussion 64
4.2.1 Sample measurement case 65
4.2.2 Sizing and Velocimetry 68
4.2.3 DNC 72
4.2.4 LWC 82
4.3 Summary 88

5 In situ precipitation measurements 91
5.1 Precipitation measurements 91
5.2 Results and discussion 94
5.3 Summary 99

6 Conclusion and outlook 101

Appendices 107

A Laboratory experiments with cloud-like droplets 107
A.1 Experimental set-up 107
A.2 Detection properties 109

B Applied modifications and Filters to PDI data 117
B.1 Modified swept method 117
B.2 Coincidence filter 118
B.3 D_{min} cutoff 120

C PDI channel 1 121

References 125

List of Tables

2.1 Properties of the VisiSize D30 shadowgraph system for three different lens magnification settings provided by Oxford Lasers Ltd. 30
2.2 Explanation of the parameters reported in output droplet file together with corresponding symbols used to denote them in the text. 33
2.3 Technical data of OTT Parsivel^2 Laser-Optical disdrometer provided by OTT HydroMet. 48

3.1 Settings of the FMAG droplet generator used during sizing experiments. 50

4.1 Statistics of the VisiSize measurements at the UFS during 2019 campaign listing the number of selected measurement cases for different modes and lens magnification settings. . . . 62
4.2 Comparison between the cloud droplet measurement data from the VisiSize and PDI probe collected on 13th July 2019 15:36' - 15:51'. 66

A.1 Statistics of the laboratory experiment with poly-disperse droplets for different lens magnification settings. 109
A.2 Results of the laboratory experiment with poly-disperse droplets: comparison of different methods used for estimating size-dependent sample volumes. 115

List of Figures

1.1 Examples of in situ sampling for cloud microphysical experiments: (a) ground-based measurements at High Altitude Research Station Jungfraujoch (JFJ) in the Bernese Alps, Switzerland (3580 m MSL; 7°59'2"E, 46°32'53"N) (Schlenczek et al., 2017b); (b) airborne measurements with a Twin Otter aircraft of British Antarctic Survey (BAS) on "Meteorological Airborne Science Instrumentation" (MASIN) trials in Calgary 2004. This image is associated with 2005-2010 BAS science programme: ACES – Antarctic Climate and the Earth System (source: BAS). 3

1.2 Examples of remote sensing in cloud microphysical experiments: (a) An artist's illustration of NASA's Cloudsat satellite (Photo credits: Graeme L. Stephens; NASA); (b) The Wyoming Cloud Radar (WCR) deployed on the Wyoming King Air research aircraft (source: AS Dept. UW); (c) A Doppler Cloud Radar manufactured by Radiometer Physics GmbH (source: RPG GmbH), (d) a Doppler lidar system Stream Line (METEK GmbH; source: IGF-UW-a) manufactured by Halo Photonics Ltd, and (e) a microwave radiometer HATPRO-G2 used for ground-based measurements(source: IGF-UW-b). . 4

1.3 Examples of spectrometers using light scattering for droplet detection and sizing: (a) The Forward Scattering Spectrometer Probe, Model 100 (FSSP-100; source: EOL, a); (b) The Cloud Droplet Probe (CDP), and (c) The Cloud and Aerosol Spectrometer (CAS) both used during the Tropical Warm Pool International Cloud Experiment (TWP-ICE; source: McFarquhar et al., 2007). 6

1.4 Three photos showing the Flight Phase Doppler Interferometer (F/PDI) manufactured by Artium Tech Inc.: (a) The instrument mounted vertically on board the CIRPAS Twin Otter; (b) A pre-flight test where a spray paint nozzle produces a distilled water spray at reasonably high velocity ($\sim$ 5 $m.s^{-1}$). The crossing laser beams are clearly visible. The beams emerge from the upper arm and are stopped by a beam stop on the lower arm. The scattered light enters the lower arm and is sensed by three photo-detectors; (c) A front-on view of the two arms and the relative location of the view volume. The instrument body is 28×56×6.6 cm; each arm is 30 cm long and 3 cm in diameter; the arms are 15 cm apart (source: Chuang et al., 2008). 8

1.5 Comparisons of the shape of the drop size distribution as measured by the F/PDI and a FSSP-100. Panels A, B, and C represent the mean diameter percentiles: d_{50}, d_{10}, and d_{90}, respectively, for the measured size distributions. In each of these panels, the line terminated by two circles represents 5 µm. Panel D represents the spectral width ($= d_{90}–d_{10}$). In all panels, a 1:1 line is drawn. Each dot represents 1 s of data. Approximately 7000 s worth of data is shown.(source: Chuang et al., 2008). 9

1.6 Comparison of the measured drop number concentration by the F/PDI and FSSP in six different nominal size bins. In all cases, the F/PDI distributions have been shifted towards a smaller size by 5 µm to account for the sizing discrepancy shown in Fig. 1.5. This was more convenient than shifting the FSSP distributions upwards by the same amount and is not meant to imply that these represent the actual drop sizes.(source: Chuang et al., 2008). 10

1.7 Examples of holographic instruments used in cloud microphysical measurements: (a) The Holographic Detector for Clouds (HOLODEC) carried on an NSF/NCAR C-130 airplane (photo credit: Raymond Shaw; source: Vice); (b) A schematic representation of HOLODEC (source: MTU); (c) The holographic imaging instrument, ICEMET (Icing Condition Evaluation Method; Kaikkonen et al.; Molkoselkä et al., 2021) mounted on Puijo measurement station in Kuopio, Finland, during ground-based measurements of liquid clouds. The wind wing is used to align the sensor according to the wind direction (photo credit: Ari Leskinen; Tiitta et al., 2022). 12

1.8 Example of instruments using shadowgraph imaging technique for in situ cloud microphysical measurements: (a) 2D-C probe (source: EOL, b); (b) 2D-S and CPI probes installed on NCAR C130 research aircraft (source: SPEC Inc.). 14

1.9 Optical Diagram of a 2D-C probe. Additional mirrors and lenses are not shown here. The shadow of the hydrometeor passes over the diode array as the aircraft moves in the flight direction, so rapid sampling of that array records the image of the hydrometeor(source: Baumgardner and Korolev, 1997). . . 15

1.10 Examples of images captured by 2D-S, 2D-C, and CPI probes in a mixed-phased upslope cloud investigated by the NCAR C-130 research aircraft. All of the particle images in this figure have been hand-picked and placed using a graphic tool; i.e., the spatial relationships of the particles are not as observed by the probes (source: Lawson et al., 2006). 16

1.11 Schematic representation of the CPI (a) and 3V-CPI (b) where two PDS detectors in CPI are replaced by two 128-photodiode linear arrays in 3V-CPI probe (Source: SPEC Inc.). 17

1.12 Schematic representation of the threshold method showing shadow images of two sample droplets – an in-focus droplet (left) and a defocused droplet (right) – above greyscale intensity profiles illustrating the applied thresholds (source: Kashdan et al., 2003). 20

1.13 Topography near the UFS: (a,b) The UFS is located near the German-Austrian border, immediately south-west of Mountain Zugspitze in the German Alps (source: Google Earth); (c) View of UFS from the east during summer, showing also the Schneefernerkopf, a mountain ridge at the west of the UFS with its low spot named ”wind hole”; (d) View of UFS from the south during summer where all 12 floors of the building, as well as the direction of Zugspitze summit, are shown (Credits: UFS GmbH, source: schneefernerhaus.de). 24

1.14 PDFs of the horizontal wind direction (left panel) and the wind speed (right panel). In the plot of the horizontal wind direction,0° corresponds to the wind coming from the north, and 90 and 270° correspond to the wind from the east and the west, respectively. The condition for “clouds” is that the relative humidity be above 99% (source: Risius et al., 2015). . 26

1.15 Fraction of time during which the UFS is covered by clouds during any month of the year. The red curve is the average cloud fraction, and the green curves are the maximum and minimum monthly values over the period of data analyzed. From the top to the bottom, the three panels are the total fraction of cloud covering, the fraction of clouds from the east and the fraction of clouds from the west (source: Risius et al., 2015). 27

1.16 Comparison of inferred cloud droplet size distributions with those obtained with an Artium dual range flight probe phase-Doppler interferometer (PDI-FPDR). The size distributions compare well for both narrow (a) and broad (b) size distributions (source: Bertens et al., 2021). 28

2.1 (a): A schematic of the system configuration for sizing; (b): Main components of the VisiSize, an infrared pulse laser with a diffuser (left) and a CCD camera with lens objective enclosed in a water-proof housing (right). 31

2.2 A typical shadowgram of droplets produced by an ultrasonic droplet generator in the laboratory and captured by the VisiSize. The image was taken during laboratory tests with a camera lens magnification settings of $\times 2$. 32

2.3 Illustration of the thresholds used in PDIA method, showing two actual sample droplets captured by the VisiSize: in-focus droplet [left] and defocused droplet [right]. The grayscale intensity profiles below them illustrates applied thresholds as well. 35

2.4 (a): Configuration of a basic phase Doppler interferometer (PDI) system; (b): Calculated interference fringe pattern with the segmented receiver placed over the pattern showing how the fringe spacing can be measured using the phase shift information (Source: Artium Tech. Inc.). 41

2.5 (a) The PDI probe manufactured by Artium Tech. Inc.(Source: Artium Tech. Inc.); (b) The photo was taken during a ground-based cloud measurement in the UFS while both PDI channels were on; (c) A magnified schematic illustration of the cylindrical probe volume (PV) within the intersection of two laser beams. 42

2.6 (a): Schematic representation of the cylindrical effective probe volume (PV) and probe area (PA) of the PDI for two different sizes of three passing droplets; (b): side view of the panel (a) showing trajectories of the droplets located at different positions (x) from the yz plane; (c): relations between size (D) and position (x) of the droplets along with the formula of scattered intensity (I_s) as a function of x and D (where k is an instrumental constant); (D): qualitative graphs of $I_s - x$ illustrating the scattered intensity of each droplet based on its x and D as well as minimum I_s below which the droplet cannot be detected. 44

2.7 (a): A photo of OTT Parsivel^2 Laser-Optical disdrometer showing its symmetrically arranged measuring heads; (b): A schematic illustration of the functional principle of the disdrometer showing the measuring area between the transmitter and receiver. 47

3.1 Experimental setup for studying sizing performance of the VisiSize; (a) The VisiSize D30 is located above the exit of the FMAG droplet generator to measure droplets; Two different configurations are used: (b) with the cylindrical case above the nozzle or (c) without the cylindrical case. 51

3.2 Sample shadow images captured with the VisiSize D30 showing droplets of different sizes generated with the FMAG. . . . 52

3.3 Probability distributions of droplet size measured by the VisiSize D30 in the configuration as in fig. 3.1 panel (c) (distance between sample volume and nozzle head is $\sim 4.5\,\mathrm{cm}$), for different camera lens magnifications and different FMAG output droplet sizes. The initial size of the generated droplets as well as the size after double and triple collisions are marked with vertical lines. 53

3.4 All analyzed measurement cases from the second series of lab experiments with the VisiSize D30. Top: Comparison of generated flow rate (Q) with the FMAG and the measured average droplet velocity by the VisiSize among the analyzed cases. Bottom: Corresponding percentage of each droplet size category in the measurements based on DSD histogram peaks (single droplet, double collision, and triple & more collision). . 55

3.5 Probability distributions of droplet size measured by VisiSize D30 in configuration as in fig. 3.1 panel (b) (distance between sample volume and nozzle head is $\sim$18.5 cm), for camera lens magnification setting $\times 1$. The initial size of the generated droplets as well as the size after double and triple collisions are marked with vertical red lines. 56

3.6 Comparison of droplet sizing between VisiSize D30 and FMAG: scatter plot illustrating the position of the first peak in size histogram and arithmetic mean diameter with respect to FMAG generated droplet sizes for different lens magnification settings (left). Red boxes (a, b, c) are enlarged in panels on the right. Each pair of points (filled and empty) represents a single measurement. 57

4.1 Cloud field experiment at the Schneefernerhaus: (a) View of the UFS from Zugspitzplatt on a sunny day, pointing out the measurement site on the 9th-floor rooftop; (b) The same view while the UFS is immersed in clouds; (c) Main instruments: the VisiSize, and the PDI probe mounted next to each other, while clouds are approaching the UFS from the west side. . . . 60

4.2 The schematic representation of the experimental setup orientation during the Zugspitze measurement campaign at the UFS. This configuration allows to optimally measure the clouds coming with the wind from the "wind hole" located on the Schneefernerkopf in west of the UFS. 61

4.3 Local weather conditions at the UFS, obtained from recordings by German Weather Service (Deutscher Wetterdienst, DWD) during the measurement campaign including temperature, relative humidity, wind speed and wind direction. Each single point in the plots represents a mean of DWD data collected during a selected measurement case (over a 15 minute interval). The selected cases in each day are shown in chronological order from left to right, however, all two adjacent points do not necessarily represent two consecutive measurements. Wind direction is measured relative to the northerly orientation, with easterly, southerly, and westerly winds being assigned 90°, 180°, and 270° angle respectively. 63

4.4 Probability distributions of cloud droplet sizes for data collected with the VisiSize and the PDI probe during measurement on 13th July 2019, 15:36' – 15:51'. The distributions have been truncated at progressively large values of droplet diameter for each plot: $(a) D > 0\,\mu m, (b) D > 9\,\mu m, (c) D > 11\,\mu m, (d) D > 13\,\mu m$. The resulting arithmetic mean diameters for each instrument are shown in the legend. 67

4.5 Comparison of cloud droplet mean diameter between the VisiSize and the PDI probe. Scatter plots of arithmetic mean ($\bar{D}$), surface mean (D_2) and volume mean (D_3) are shown from left to right respectively. Each pair of blue/red circles indicates raw/modified data for a selected measurement of ∼15 min long. Pearson correlation coefficients (PCC) also shown in the legend as an index of linear correlation. 68

4.6 Comparison between the VisiSize and the PDI probe regarding the diameter size percentiles (D_{10}, D_{50}, and D_{90}) as well as spectral width ($D_{90} - D_{10}$) of cloud droplets. Each pair of blue/red circles indicates raw/modified data for a selected measurement of ∼15 min long. Pearson correlation coefficients (PCC) also shown in the legend. The second row shows each plot after applying the D_{min} cutoff to the data. 69

4.7 Comparing the droplet mean velocity between the VisiSize and the PDI probe. Each pair of blue/red circles indicates raw/modified data for a selected measurement of ∼15 min. The least squares regression (LSR) lines are displayed with dash, and the Pearson correlation coefficient (PCC) are shown in the legend. 71

4.8 Comparison of the DNC results between the VisiSize and the PDI probe. From top - left to top - right, the plots respectively show the raw data, the data after modification, and the modified data after applying the coincidence filter to the PDI results. The scatter plots after applying the D_{min} cutoff are shown in the second row. Each PDI method for the DNC computation is shown with a different color within the plots (each pair of blue/red circles: a selected measurement of ∼15 min long). The least squares regression (LSR) lines are displayed with dashed lines blue/red, and the Pearson correlation coefficient (PCC) are shown in the legend. 74

4.9 The DNC ratio of the VisiSize to the PVC-PDI as a function of arithmetic mean diameter size. Panels (a-c) show the raw data (using the default SV for the VisiSize), the results after the SV correction and the $D_{\min}$ cutoff, and the results after additionally applying the coincidence filter to the PDI data. Each circle represents a single measurement of ∼15 min. The reciprocal fit curves ($y = \frac{a}{x+b}$) and the 1:1 ratio are shown with the dashed and horizontal black lines, respectively. 75

4.10 The DNC comparison between the two instruments, with cases using different lens magnification settings for the VisiSize (×2 and ×4) are plotted separately. The results after applying all modifications and filters to the data and application of PVC factor on PDI swept volume method are used here. Each circle/star represents a single measurement of ∼15 min. Dashed red lines show the LSR, and the PCC is shown in the legend. . 77

4.11 The DNC comparison between the two instruments, with the mean diameter spectra (top panel) and the standard deviation of velocity spectra (bottom panel) compared between the selected cases. The results after applying all modifications and filters to the data and with application of the PVC factor to the modified PDI swept volume method are used here. The mean diameters and the velocity standard deviations are calculated using the VisiSize and PDI data, respectively. Each circle represents a single measurement of ∼15 min. 79

4.12 Comparison of the DNC results between the VisiSize and the PDI probe with and without data collected during easterly wind events. The modified data after applying the coincidence filter to the PDI results as well as $D_{\min}$ cutoff on both instruments are shown here. 81

4.13 Comparison of the LWC results between the VisiSize and the PDI probe. From top - left to top - right, the plots show the raw data (based on the default sample volume for the VisiSize and the original DNC methods for the PDI), the data after modification, and the modified data after applying the coincidence filter to the PDI results. The scatter plots after applying the D_{min} cutoff are shown in the second row. Each PDI method for the LWC computation is shown with a different color within the plots (each pair of blue and red circles: a selected measurement of ∼15 min). Dashed blue/red lines show the LSR, and the PCCs are displayed in the legend. . . . 83

4.14 The LWC comparison between the two instruments, with cases using different lens magnification settings for the VisiSize (×2 and ×4), plotted separately. The results after applying all modifications and filters to the data, and application of PVC factor to the modified swept volume method of the PDI, are shown here. Each circle/star represents a single measurement of 15min. Dashed red lines show the LSR, and the PCC is shown in the legend. 85

4.15 The LWC comparison between the two instruments, while the mean diameter spectra (top panel) and the standard deviation of velocity spectra (bottom panel) are also compared between the selected cases. The results after applying all modifications and filters to the data, and with application of PVC factor to the PDI swept volume method, are shown here. The mean diameters and the velocity standard deviations are taken from the VisiSize and the PDI data, respectively. Each circle represents a single measurement of ∼15 min. 86

4.16 Comparison of the LWC results between the VisiSize and the PDI probe after adjusting the DNCs from the PDI using the reciprocal fit ($y = \frac{a}{x+b}$; see Fig. 4.9). The data are shown after correction of the SV, applying the coincidence filter to the PDI results, and D_{min} cutoff to both instruments' data. Each PDI method for the LWC computation is shown with a different color within the plot (each pair of blue and red circles: a selected measurement of ∼15min). Dashed blue/red lines show the LSR, and the PCCs are displayed in the legend. 88

5.1 Sample shadowgrams captured during a cloud-rain mixed event at the UFS observatory on 13th of August 2019: (a) a captured rain drop; (b) and (c) a couple of cloud droplets from the same captured series. 92

5.2 "VisiSize D30" shadowgraph instrument (front) and "OTT Parsivel^2" laser disdrometer (back) deployed next to each other at Meteo-station on the rooftop of the Institute of Geophysics, University of Warsaw (IGF-UW). 93

5.3 Sample cropped shadowgrams of raindrops, ice particles, and snowflakes captured during different weather events of Warsaw with the VisiSize deployed on the rooftop of IGF-UW. 94

5.4 The DSD histograms of raindrops collected on the rooftop of IGF-UW on 18th of November 2018, 20:26' - 23:54'. 95

5.5 The DSD histogram of the same measurement as Fig. 5.4, while drops out of common measuring range (0.25 - 2.25 mm) were excluded. 95

5.6 The DSD histogram of precipitation particles collected on the rooftop of IGF-UW on 24th of December 2018, 21:28' - 24:00'. 97

5.7 The DSD histogram of the same measurement as Fig. 5.6, while particles out of the common measuring range (0.25 - 2.25 mm) were excluded. 97

5.8 DSD histogram of raindrops collected on the rooftop of IGF-UW on 13th of November 2018, 19:27' - 24:00', while drops out of common measuring range (0.25 - 2.25 mm) were excluded. . 98

5.9 DSD histogram of precipitation particles collected on the rooftop of IGF-UW on 31st of January 2019, 11:10' - 12:46', while particles out of common measuring range (0.25 - 2.25 mm) were excluded. 98

A.1 Experimental setup for studying the detection properties. The main parts of the VisiSize D30 are an infrared pulse laser with a diffuser (top right) and a CCD camera with the lens objective enclosed in a waterproof housing (top left). Water droplets produced with an ultrasonic droplet generator are measured while passing through the sample volume (top middle) located close to the camera. 108

A.2 A typical shadow image of droplets produced by ultrasonic droplet generator taken during laboratory tests with the camera lens magnification ×2. 109

A.3 Maximum range of defocus distance z for each size bin: derived from the volumes listed in summary file from VisiSize software (shown with ×) versus the actual maximum values $z_{\mathtt{max}}$ found in the experimental data (shown with ∘), together with two analytical approximations - default $z_{\mathtt{def}}$ and corrected $z_{\mathtt{95}}$. Measurement series for lens magnification settings: (a) ×1, (b) ×2, (c) ×4. 111

A.4 Schematic illustration of the difference between the default and the corrected/individual sample volumes while having the same field of view $S = (L_x - D_i)(L_y - D_i)$, but different depths of fields ($z_{\mathtt{def}}$ vs. z_{95}). 112

A.5 Comparison of droplet size distributions obtained with three methods, default (def), corrected (cor) and individual (ind), during the three measurement series differing in lens magnification settings. The same data are plotted in (a) linear and (b) logarithmic scales. 114

C.1 Comparison of droplet arithmetic mean diameters between the VisiSize and the PDI probe channel 1. The blue circle represents measurement cases where the VisiSize lens magnification $\times 2$ was used, while the red star shows the measurements with magnification $\times 4$. Each measurement case was between ~ 7 - 14 minutes long, while both instruments were collecting cloud droplets data simultaneously. The Pearson correlation coefficient (PCC) is also shown in the legend. 122

1 Introduction

This chapter is divided into two parts. The first part introduces experimental approaches in cloud microphysical research, including elaborating on the shadowgraph imaging technique (shadowgraphy). The second is a literature review of cloud measurements performed at Umweltforschungsstation Schneefernerhaus (UFS) - an environmental research station in the German Alps, where most of the data used in the current study were collected. A concise summary of each part has been already published by Nowak et al. (2021) and Mohammadi et al. (2022a), and the subjects are elucidated further within this chapter.

1.1 Experimental approaches in cloud microphysics

Cloud-related processes are the most unpredictable in weather forecasting and climate research. They continue to be a weak link in atmospheric circulation models as well (Bodenschatz et al., 2010). Atmospheric clouds mainly consist of water droplets. The cloud droplet number concentration (DNC) and droplet size distribution (DSD) play a significant role in the quantitative microphysical description of clouds. They are also considered as critical properties of clouds during research on cloud lifetime, radiative effects, and precipitation formation (Devenish et al., 2012).

As the cloud droplets grow, they can form raindrops and ultimately fall as precipitation to the ground. The microstructure of precipitation (i.e. the characteristics of individual raindrops) is controlled by the intricate interplay between cloud microphysics and atmospheric dynamics (Testik and Barros, 2007). A fundamental property of rainfall for the investigation of its microstructure is also the DSD. All bulk rainfall variables of interest can be derived as weighted moments of the DSD (Ulbrich, 1983; Testud et al., 2001). It is of paramount importance not only for the remote sensing of precipitation but also for the numerical weather modeling, rainfall infiltration, soil erosion, and pollutant dispersal, both on the ground and in the atmosphere (Salles et al., 2002; Uijlenhoet and Torres, 2006; Jaffrain and Berne, 2011; Raupach and Berne, 2015). Hence, in order to study microphysics of hydrometeors effectively, accurate measurement of the DSD is essential.

There are two general approaches to measuring the microphysical properties of hydrometeors, particularly cloud droplets:

- in situ sampling,
- remote sensing.

The in situ sampling requires the instrumentation to be located directly at the point of interest and in contact with the hydrometeors (source: Britannica). It can be conducted at airborne platforms (e.g., Jen-La Plante et al., 2016; Gerber et al., 2016; Siebert et al., 2021) or ground-based stations (e.g., Markowicz et al., 2019; Markowicz and Chiliński, 2020) as shown in Fig. 1.1.

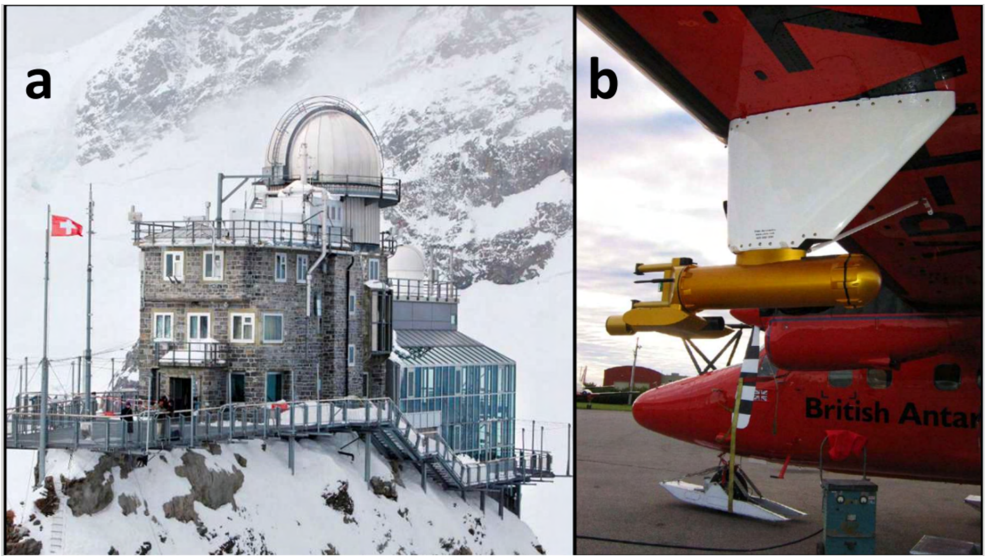

Figure 1.1: Examples of in situ sampling for cloud microphysical experiments: (a) ground-based measurements at High Altitude Research Station Jungfraujoch (JFJ) in the Bernese Alps, Switzerland (3580 m MSL; 7°59'2"E, 46°32'53"N) (Schlenczek et al., 2017b); (b) airborne measurements with a Twin Otter aircraft of British Antarctic Survey (BAS) on "Meteorological Airborne Science Instrumentation" (MASIN) trials in Calgary 2004. This image is associated with 2005-2010 BAS science programme: ACES – Antarctic Climate and the Earth System (source: BAS).

On the other hand, the remote sensing involves applying inverse retrieval techniques to data collected without coming into direct contact with clouds (e.g., Zawadzka-Manko et al., 2020; Wang et al., 2020). It can be conducted with satellite, aircraft or ground-based measurements using radar, lidar, sodar, and radiometer systems. Fig. 1.2 shows some examples of remote sensing instruments.

Intrinsic difficulties are involved in both strategies. For instance, in situ methods often have to account for:

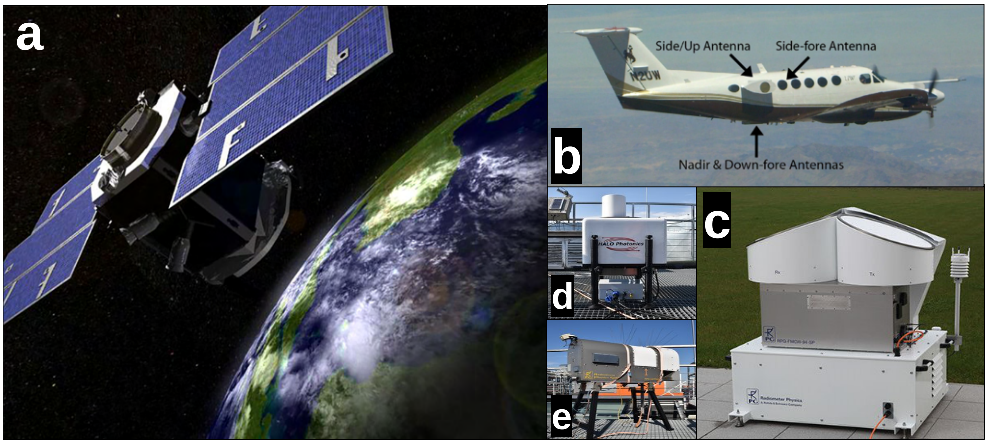

Figure 1.2: Examples of remote sensing in cloud microphysical experiments: (a) An artist's illustration of NASA's Cloudsat satellite (Photo credits: Graeme L. Stephens; NASA); (b) The Wyoming Cloud Radar (WCR) deployed on the Wyoming King Air research aircraft (source: AS Dept. UW); (c) A Doppler Cloud Radar manufactured by Radiometer Physics GmbH (source: RPG GmbH), (d) a Doppler lidar system Stream Line (METEK GmbH; source: IGF-UW-a) manufactured by Halo Photonics Ltd, and (e) a microwave radiometer HATPRO-G2 used for ground-based measurements(source: IGF-UW-b).

- dependence of sample volume on particle size or air flow velocity,
- non-linearity of Mie scattering intensity regarding droplet size,
- aerodynamic effects related to flow around instrument or aircraft,
- exposure of instrument to harsh conditions (including icing, wetting, and temperature changes).

These challenges can necessitate handling of large data set or instantaneous data processing during the course of measurements.

On the other hand, remote sensing provides information with limited spatial resolution. Acquired this way, microphysical properties of clouds represent only averages or integrals over relatively large volumes. Results might be too simplistic to characterize inhomogeneous or multilayered cloud fields.

Furthermore, the result depends on the assumption of a specific size distribution of droplets/particles or specific vertical structure of the atmosphere.

Nevertheless, the in situ measurements are considered fundamental for cloud microphysics studies, as they offer instrumental access to individual droplets in a sampling volume. The results obtained in situ can be used to derive and validate inversion routines implemented in remote sensing applications (e.g., Jakubiak et al., 2014).

1.1.1 In situ measurement methods

The in situ measurement instruments, for cloud microphysics research, can be categorized by the sampling style into two groups:

- Instruments which detect and count droplets one by one almost continuously while passing through a very small sample volume. The result includes each droplet's properties and the inter-arrival time,
- Instruments which capture images or another spatial representation of a larger sampling volume (containing multiple droplets). The result includes individual droplet properties and information about the spatial arrangement of droplets.

The first branch is represented by a number of spectrometers that use light scattering for droplet detection and sizing, e.g. Forward Scattering Spectrometer Probe (FSSP; e.g., Cooper, 1988; Brenguier et al., 1998; Gerber et al., 1999; de Araújo Coelho et al., 2005), Cloud Droplet Probe (CDP; e.g., McFarquhar et al., 2007; Lance et al., 2010; Lance, 2012), Cloud and Aerosol Spectrometer (CAS; e.g., Lance, 2012; Glen and Brooks, 2013; Barone et al.,

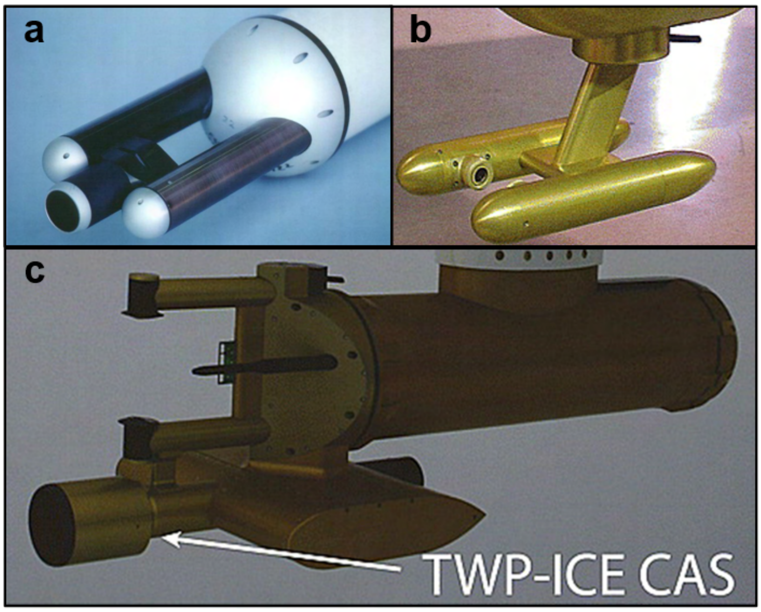

Figure 1.3: Examples of spectrometers using light scattering for droplet detection and sizing: (a) The Forward Scattering Spectrometer Probe, Model 100 (FSSP-100; source: EOL, a); (b) The Cloud Droplet Probe (CDP), and (c) The Cloud and Aerosol Spectrometer (CAS) both used during the Tropical Warm Pool International Cloud Experiment (TWP-ICE; source: McFarquhar et al., 2007).

2019), and Phase Doppler Interferometer (PDI; e.g., Bachalo and Houser, 1984; Chuang et al., 2008; Kumar et al., 2019), as is shown in Fig. 1.3.

In practice, they sample a quasi-one-dimensional portion of air whose orientation and length depend on its velocity relative to the instrument. Therefore, essential for the DNC estimation is precise information on air velocity. Moreover, for droplet size measurement, there is an upper limit due to having a small probe volume cross-section in this type of instruments. For instance, the CDP can measure droplet sizes up to 50 µm.

Phase Doppler Interferometry is a common technique within the one-by-one droplet counting methods. The PDI probe is a spectrometer using phase Doppler interferometry to obtain the droplet size from an interference fringe pattern produced by the scattered light. The PDI was used first by Bachalo and Houser (1984) for spray droplet size and velocity characterization.

Later, Chuang et al. (2008) tested Artium Flight-PDI (F/PDI) as a cloud droplet sizing instrument for airborne measurements (see Fig. 1.4). They used a new model for determining the probe volume, then performed an inter-comparison among instruments: PDI, FSSP-100 (Lu et al., 2007) and a Particulate Volume Monitor (PVM-100A; Gerber et al., 1994) based on the Liquid Water Content (LWC), DSD, and DNC measurements.

Results showed good agreements between the PDI and the PVM regarding the LWC in spite of highlighting some differences. However, comparing the DSDs obtained from the PDI and the FSSP revealed an approximately 5 µm difference in sizing between them. In addition, about 20 to 50 % difference in spectral breadth ($= d_{90} - d_{10}$) was observed between the data collected with the PDI and the FSSP (see Fig. 1.5). Considering the sizing bias, the DNC results were found to be correlated, yet typically differed by a factor of 1.2 - 2.0, with consistently higher values for the FSSP (see Fig. 1.6). This discrepancy in the DNC was believed to be due to either the FSSP triggering noise, resulting in false droplet detections, or uncertainties in the PDI counting or probe volume.

In contrast to the instruments mentioned above (the FSSP and the PDI), there is a second group of instruments using the volumetric method in measuring cloud droplets. Devices that work based on shadowgraphy and holography techniques belong to this group. These techniques allow for obtaining the droplet properties from its images captured inside a larger sample volume. The sample volume does not depend on the velocity of the flow. Consecutive

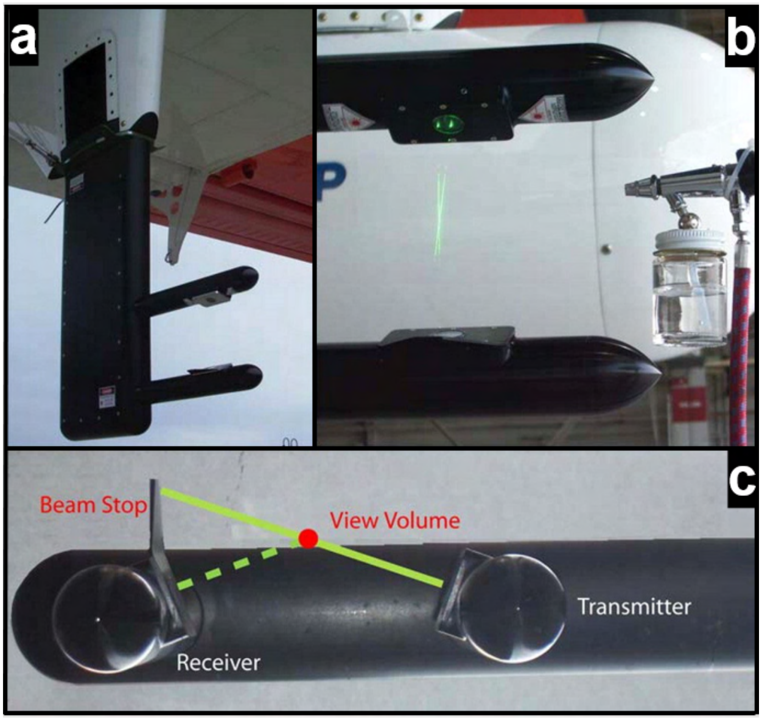

Figure 1.4: Three photos showing the Flight Phase Doppler Interferometer (F/PDI) manufactured by Artium Tech Inc.: (a) The instrument mounted vertically on board the CIRPAS Twin Otter; (b) A pre-flight test where a spray paint nozzle produces a distilled water spray at reasonably high velocity (~ 5 m.s^{-1}). The crossing laser beams are clearly visible. The beams emerge from the upper arm and are stopped by a beam stop on the lower arm. The scattered light enters the lower arm and is sensed by three photo-detectors; (c) A front-on view of the two arms and the relative location of the view volume. The instrument body is $28\times56\times6.6$ cm; each arm is 30 cm long and 3 cm in diameter; the arms are 15 cm apart (source: Chuang et al., 2008).

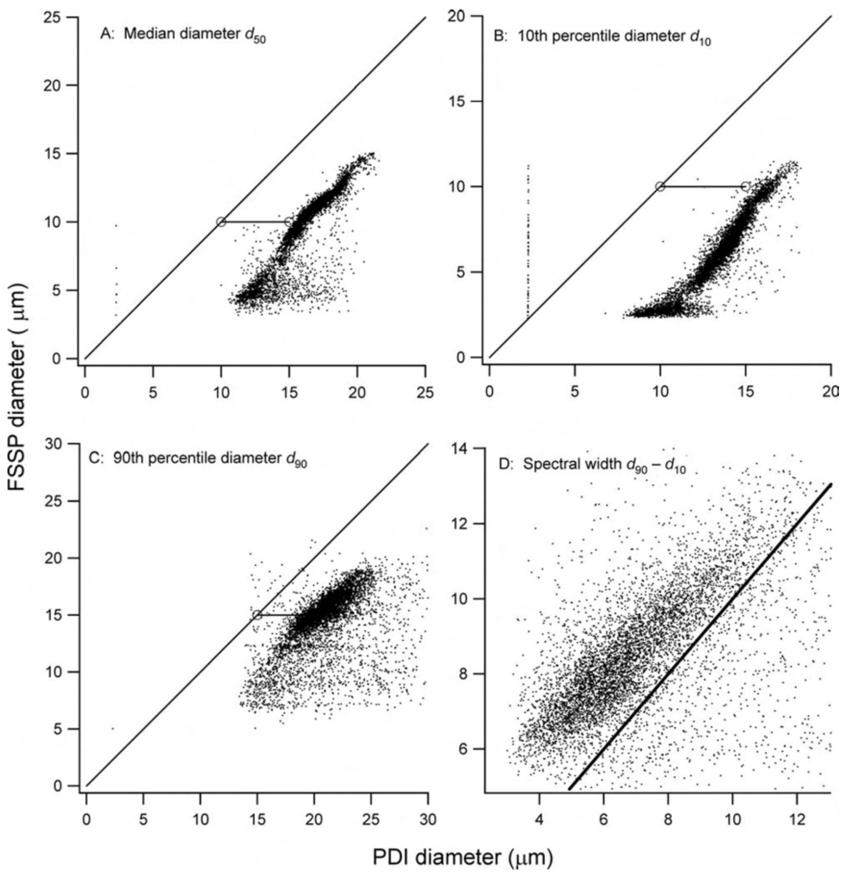

Figure 1.5: Comparisons of the shape of the drop size distribution as measured by the F/PDI and a FSSP-100. Panels A, B, and C represent the mean diameter percentiles: d_{50}, d_{10}, and d_{90}, respectively, for the measured size distributions. In each of these panels, the line terminated by two circles represents 5 µm. Panel D represents the spectral width $(= d_{90} - d_{10})$. In all panels, a 1:1 line is drawn. Each dot represents 1 s of data. Approximately 7000 s worth of data is shown.(source: Chuang et al., 2008).

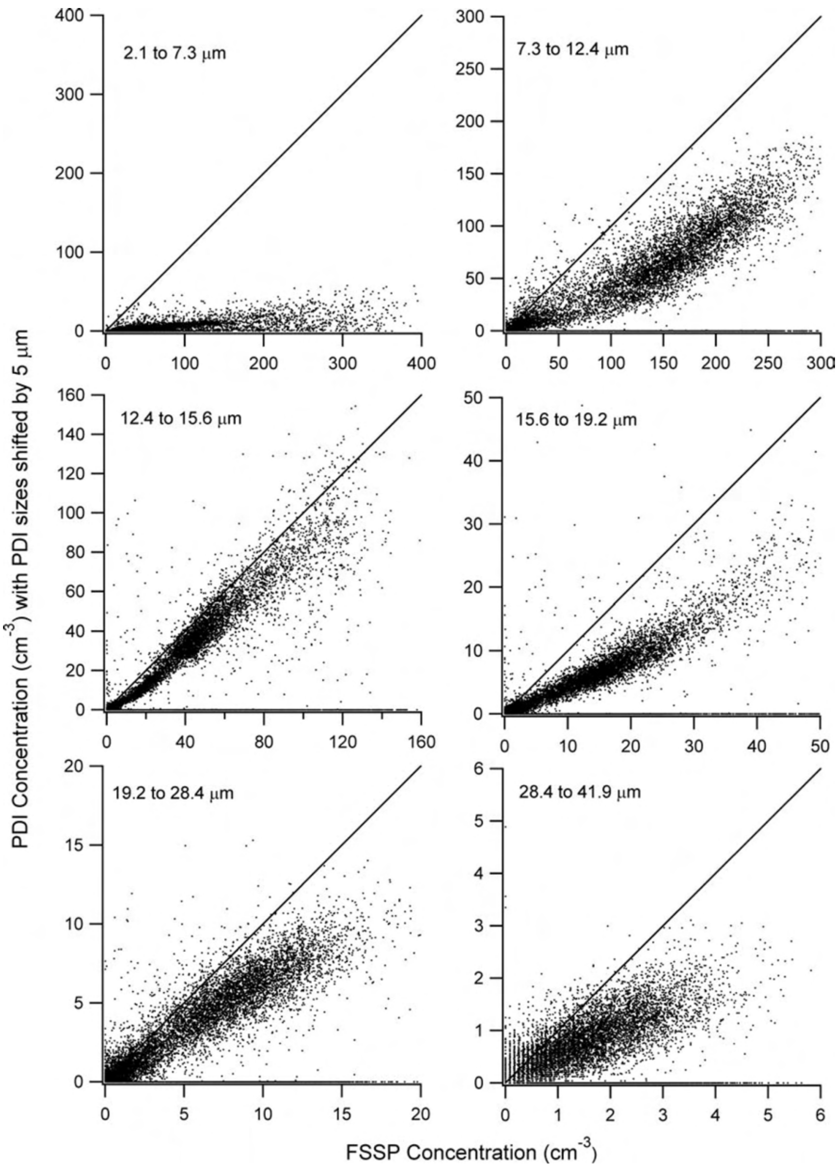

Figure 1.6: Comparison of the measured drop number concentration by the F/PDI and FSSP in six different nominal size bins. In all cases, the F/PDI distributions have been shifted towards a smaller size by 5 µm to account for the sizing discrepancy shown in Fig. 1.5. This was more convenient than shifting the FSSP distributions upwards by the same amount and is not meant to imply that these represent the actual drop sizes.(source: Chuang et al., 2008).

air samples might be quite distant, particularly when used on fast-moving airborne platforms. Both techniques allow us to study the position, size, and shape, thus not only spherical droplets but also e.g. ice crystals.

Holography requires extensive processing to digitally reconstruct the shape and arrangement of the objects digitally in three dimensions (Fugal et al., 2009). There are several studies on cloud microphysics that use holography technique during airborne campaigns (HOLODEC and HALOHolo; e.g., Fugal et al., 2009; Beals et al., 2015; Glienke et al., 2017; Schlenczek, 2017a; Larsen and Shaw, 2018; Desai et al., 2019). It has also been used on cable car platforms (HoloGondel; e.g., Beck et al., 2017), and for ground-based experiments (HOLIMO; e.g., Raupach et al., 2006; Henneberger et al., 2013; Schlenczek et al., 2017b).

Ramelli et al. (2020) investigated inhomogeneities in the microphysical properties of stratus clouds by using holography in a tethered balloon system (TBS). The inhomogeneities were defined by the variability in the DNC and the DSD, which measured up to $200\,\mathrm{cm}^{-3}$, and between 6 and 24 µm, respectively. The results showed that the instrument limit in measuring small cloud particles ($D < 6$ µm) could lead to an underestimation of DNC. This effect was observed during the measurements close to the cloud base, in fog, or in case of clouds with a small mean droplet diameter.

Fig. 1.7 shows two examples of holographic imaging instruments used for airborne and ground-based cloud microphysical measurements.

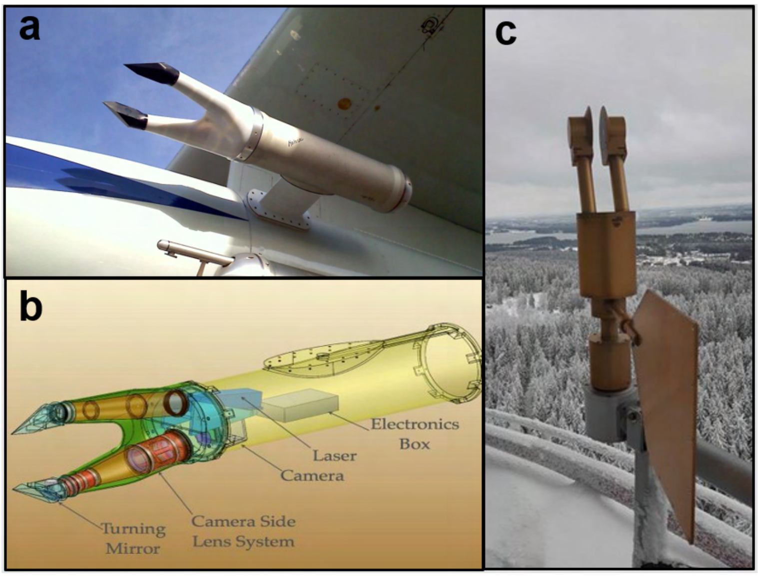

Figure 1.7: Examples of holographic instruments used in cloud microphysical measurements: (a) The Holographic Detector for Clouds (HOLODEC) carried on an NSF/NCAR C-130 airplane (photo credit: Raymond Shaw; source: Vice); (b) A schematic representation of HOLODEC (source: MTU); (c) The holographic imaging instrument, ICEMET (Icing Condition Evaluation Method; Kaikkonen et al.; Molkoselkä et al., 2021) mounted on Puijo measurement station in Kuopio, Finland, during ground-based measurements of liquid clouds. The wind wing is used to align the sensor according to the wind direction (photo credit: Ari Leskinen; Tiitta et al., 2022).

Shadowgraph Imaging Technique

Among the various optical techniques used to study particles, liquids, or gases in motion, shadowgraph imaging stands out as a relatively inexpensive yet highly effective method. Shadowgraphy has traditionally been used to qualitatively investigate the dynamics of fluids through the visualization of flows or the recording of flow streamlines (Castrejón-García et al., 2011).

In general, shadowgraphy highlights the difference in refractive index between a body and its environment (medium) or between media (Settles, 2001). With back-illumination, the light that does not interact with the object creates a luminous background, whereas the light that is refracted at the interface is dispersed, resulting in a dark interface. Consequently, shadowgraph images consist of a bright background and shadows of the interfaces between regions with varying refractive indices. In general, shadowgraphy is applicable when the medium under study is transparent and when there are significant changes in refractive index e.g., air and water (Castrejón-García et al., 2011).

The two primary components of most shadowgraph systems are the illumination source and the recording element. Briefly, the objective of the illumination source is to achieve a uniform background at the recording sensor and to deliver the light that is refracted by the object or medium under investigation. The recording system includes the optical components necessary to create and record an image of the object's shadow (Castrejón-García et al., 2011). A shadow image (shadowgram) is a two-dimensional projection of the entire object onto a recording sensor. It can be processed swiftly to detect particles and obtain relevant statistics.

When it comes to the instruments using shadowgraph imaging in cloud microphysics, one can name Cloud Particle Imager (CPI) and Two-Dimensional Cloud (2D-C) probes (see Fig. 1.8). They have been used routinely during airborne measurements since the early 1970s (Knollenberg, 1970).

The 2D-C probe was originally equipped with a 32-photodiode linear array, which was later upgraded to a 64-photodiode, where each photodiode represents 25 µm pixel in the image. It records the two-dimensional shadow cast by a hydrometeor as it passes through a laser beam (see Fig.1.9). The image of the shadow is focused onto a flat surface that contains a linear

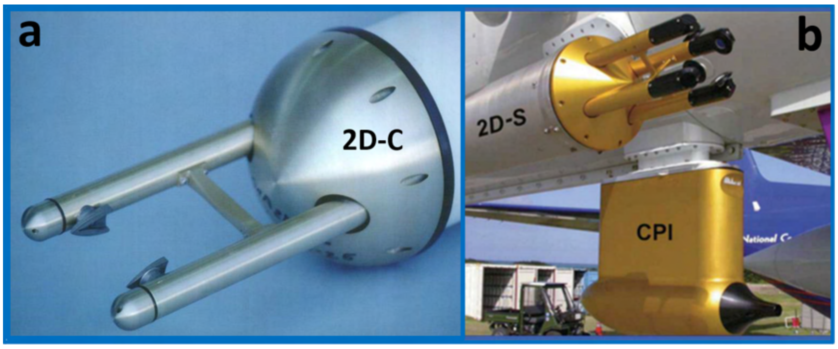

Figure 1.8: Example of instruments using shadowgraph imaging technique for in situ cloud microphysical measurements: (a) 2D-C probe (source: EOL, b); (b) 2D-S and CPI probes installed on NCAR C130 research aircraft (source: SPEC Inc.).

photodiode array. The status of these array elements (illuminated or not) is recorded at a rate that enables image reconstruction. Using the reconstructed images, one can obtain the size distribution and associated quantities of hydrometeors. Moreover, with further non-standard processing, it is also feasible to classify images and recognize the hydrometers' habits.

In theory, the pixel size, equal to 25 µm, could be considered also as a minimum size for droplet detection by a standard 2D-C probe. However, the minimum droplet size, which is detected within the sample volume at any arbitrary point, is practically larger than 25 µm. It must be noted that the optical depth of field (DOF) is smaller than the distance between the arms of the probe for hydrometeors smaller than about 150 µm. (Baumgardner and Korolev, 1997).

The new version of the 2D-C probe, called 2D-S (Stereo) probe, was manufactured by SPEC Inc. and is equipped with two 128-photodiode linear arrays working independently. Improvement encompasses the sample volume boundaries and sizing of small particles (<100 µm) and made the 2D-S

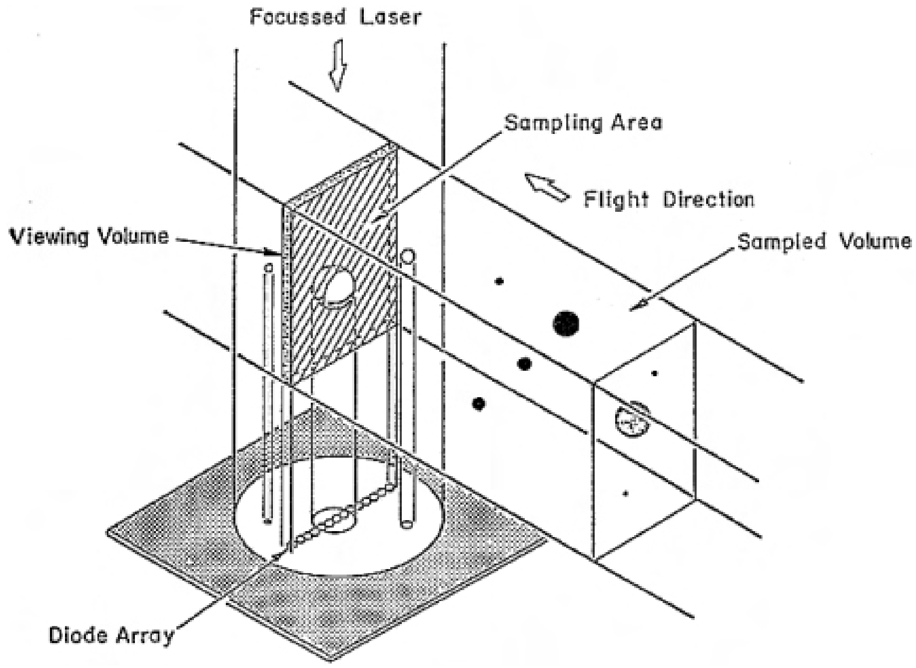

Figure 1.9: Optical Diagram of a 2D-C probe. Additional mirrors and lenses are not shown here. The shadow of the hydrometeor passes over the diode array as the aircraft moves in the flight direction, so rapid sampling of that array records the image of the hydrometeor(source: Baumgardner and Korolev, 1997).

probe more precise than its predecessor. As a result, the new probe delivers 2D images of particles as small as 10 microns passing through a sample volume where two laser beams overlap. Figure 1.10 shows examples of images captured by 2D-S, 2D-C, and CPI probes in a mixed-phased upslope cloud investigated by the NCAR C-130 research aircraft (Lawson et al., 2006).

Another significant improvement of imaging/shadowgraph probes was made by the same company - SPEC Inc. - in the late 1990s. The new probe was called CPI and has served cloud physicists for over two decades in order to separate water drops from non-spherical ice particles in mixed-phased clouds (e.g., Lawson et al., 2001; Stith et al., 2002) or identify ice particle habit in cirrus clouds (e.g., Lawson et al., 2010; Woods et al., 2018). It can

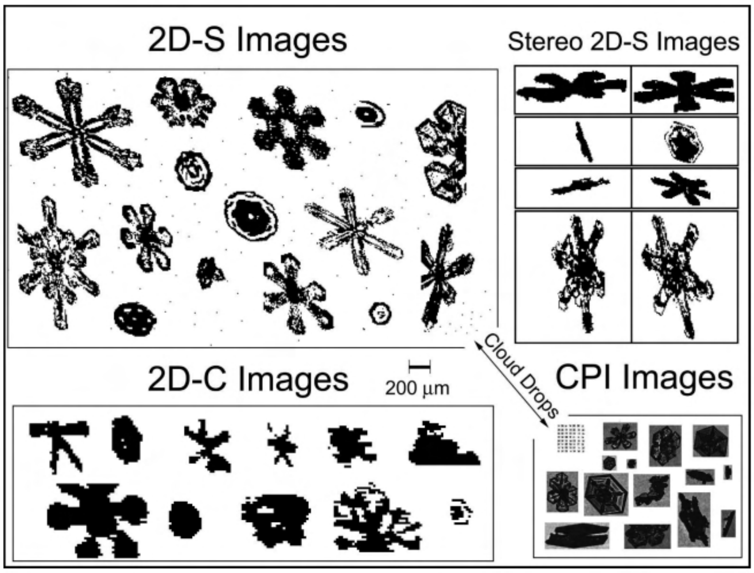

Figure 1.10: Examples of images captured by 2D-S, 2D-C, and CPI probes in a mixed-phased upslope cloud investigated by the NCAR C-130 research aircraft. All of the particle images in this figure have been hand-picked and placed using a graphic tool; i.e., the spatial relationships of the particles are not as observed by the probes (source: Lawson et al., 2006).

provide high-resolution ($2.3\,\mu m\,pix^{-1}$) shadowgrams of cloud droplets and precipitation particles over the size range of 2.3 – 2300 µm (Woods et al., 2018).

In the first version of CPI, two Particle Detection Systems (PDS) were used to detect the particles passing through a sample volume where PDS lasers overlap (see Fig.1.11-a). A CCD camera was triggered with the PDSs to capture the shadow images of particles almost simultaneously. Further developments in CPI led to increased precision of measurements and tuned-up detection efficiency of particles smaller than 100 µm (see Fig.1.11-b). The new probe series was called 3V-CPI. The enhancement was achieved by replacing the PDS detectors with two 128-photodiode linear arrays (similar to 2D-S probe).

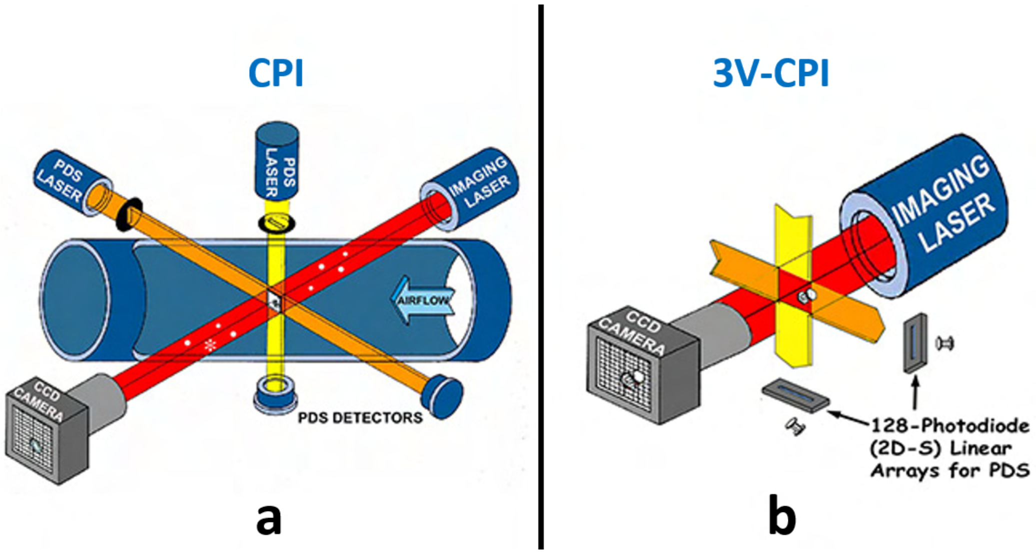

Figure 1.11: Schematic representation of the CPI (a) and 3V-CPI (b) where two PDS detectors in CPI are replaced by two 128-photodiode linear arrays in 3V-CPI probe (Source: SPEC Inc.).

Lawson et al. (2001) used the CPI for the first time during an Arctic air-borne campaign in 1998. However, the CPI could not be used alone to calculate reliable size distributions or number concentrations. It is because its camera is triggered with the PDS, and when there are more particles, the likelihood of triggering is higher than in low-concentration regions. Hence, the local concentration is biased towards the denser volumes, where the concentration is highest. Subsequently, in regions with low particle concentrations or highly inhomogeneous clouds, the local concentration can be many orders of magnitude greater than the average concentration.

Thus, the CPI size distributions must be scaled to the average concentration. The PMS-FSSP[1] with a size range of 3 - 45 µm, and the PMS-260X (40 - 640 µm) or the 2D-C (25 - 800 µm; whenever data were available) were used to scale CPI size distributions and compare the number concentrations.

[1]PMS: Particle Measuring System

Later, Stith et al. (2002) used the CPI during a tropical airborne campaign mainly to capture images of drizzle and ice particles, while the 2D-C probe was used to measure the DSD and DNC.

During 2006-2007, once again (Lawson et al., 2010) used the CPI in a couple of tropical air-borne campaigns to study cirrus clouds. They were the first measurements in which a single cloud particle probe reliably covered the size range from about 10 µm to 3 mm. The previous studies had typically blended together measurements from two instruments, a scattering probe, the FSSP (or the CAS), and an imaging probe, the 2D-C (or the CIP). The FSSP and CAS probes are known for overestimating the number of small particles. It occurs due to the occasional shattering of large ice pieces on their inlets. The 2D-C and CIP have significant sizing and counting errors for particles with sizes less than about 200 µm at the airspeed of jet aircraft (Lawson et al., 2010).

The next occasion of using the CPI in airborne measurements was between 2011-2015 for cirrus clouds measurements in the tropical tropopause layer (Woods et al., 2018). Those measurements were conducted using the following instruments; a Fast Cloud Droplet Probe (FCDP) and a Hawkeye probe (combination of FCDP, 2D-S, and CPI). They covered the droplet sizing and number concentration measurements within the range of 1 - 1280 µm (droplets between $1-50$ µm measured by the FCDP, and $10-1280$ µm by the 2D-S). The CPI also provided high-resolution cloud particle images (2.3 µm pix^{-1}) over the size range of $2.3-2300$ µm used for habit identification. However, no results from droplet sizing or concentration measured by the CPI were provided by Woods et al. (2018).

The FCDP utilizes forward scattered laser light by each particle that enters the sample volume to provide particle concentration and diameter sizing between 1 and 50 µm, with an approximately 2 µm resolution. The Hawkeye CPI is triggered by the 2D-S to record high-resolution images (2.3 µm pix^{-1}) of the particles and serves to identify ice particle habits. For each particle image, the particle focus, length, width, perimeter, area, and harmonics are determined, with a maximum uncertainty in the sizing of in-focus particles about 5 µm (Woods et al., 2018).

In general, instruments other than the CPI have been used for the DSD and DNC measurements in aforementioned studies (e.g., PMS-FSSP and PMS-260X in Lawson et al. (2001), 2D-C in Stith et al. (2002), 2D-S and CAS in Lawson et al. (2010), and FCDP in Woods et al. (2018)).

In addition to the airborne measurements, some intriguing laboratory experiments have been also conducted adopting shadowgraphy to study droplet collisions in turbulent flows (e.g., Bordás et al., 2013; Bewley et al., 2013) or icing in wind turbines (e.g., Rydblom and Thörnberg, 2016).

In 2003, a shadowgraph imaging technique called Particle/Droplet Imaging Analysis (PDIA) capable of sizing particles of arbitrary shape and size was introduced by Kashdan et al. (2003). It was originally designed for the diagnosis of agricultural and industrial sprays. The PDIA can measure the size of defocused droplets based on the degree of image blur using two threshold limits on their greyscale intensity profiles to differentiate between the dark inner area and the grey halo area around it (see Fig. 1.12).

Kashdan et al. (2003) investigated the relative uncertainties of various parameters such as the depth-of-field dependence on droplet diameter, threshold

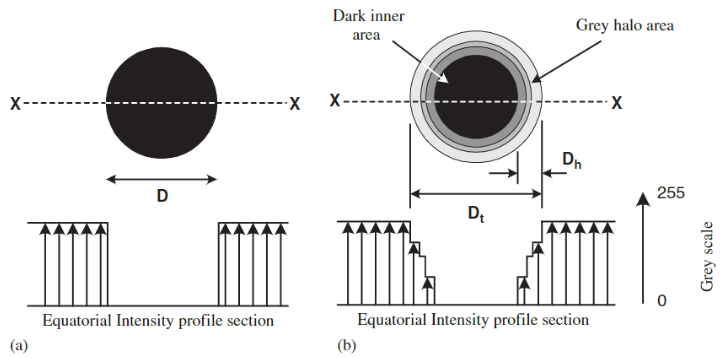

Figure 1.12: Schematic representation of the threshold method showing shadow images of two sample droplets – an in-focus droplet (left) and a defocused droplet (right) – above greyscale intensity profiles illustrating the applied thresholds (source: Kashdan et al., 2003).

level sensitivity, and image signal-to-noise issues and their effects on measurement accuracy. The image processing routine was verified with calibration data of known particle sizes which revealed that the depth-of-field varied with object diameter approximately linearly in the measured range 18 to 145 µm. The calibration data was subsequently incorporated into the PDIA processing algorithm for defocused droplets or particles, enabling their true diameter to be estimated by analyzing the droplet image properties.

The second part of their study, Kashdan et al. (2004), focused more on the application of the PDIA technique. Its capability was assessed for the characterization of small-diameter, high-speed two-phase flows produced by a pressure-swirl atomizer. Subsequently, they compared droplet size data obtained from a hollow-cone spray with similar data measured via phase Doppler anemometry (PDA), where an excellent agreement was observed between the two techniques for droplets larger than approximately 25 µm in diameter (Kashdan et al., 2007).

Sijs et al. (2021) compared shadowgraph imaging with phase Doppler particle analysis (PDPA) and laser diffraction technique (Malvern Spraytec) in spray droplet size measurements. The shadowgraph tool was the commercially available Oxford Laser VisiSizer P15. It also works based on the PDIA technique, using short, double light pulses to image an ensemble of droplets, followed by software analysis of the snapshot (frame) to determine the droplet sizes.

In the PDPA instrument manufactured by TSI, two laser beams are focused such that they intersect each other. The measurement point is defined by this intersection, where the laser beams interfere and generate a set of parallel equidistant fringes. As a droplet passes the fringes, it scatters light. The receiving optics placed at a well-chosen off-axis location project a portion of the scattered light onto multiple detectors. Each detector converts the optical signal into a Doppler burst with a frequency proportional to the particle velocity. The phase shift between the Doppler signals from different detectors is proportional to the particle's diameter.

For the laser diffraction technique, a Malvern Spraytec with a 750 mm lens was used that could detect droplets from 2 µm to 2000 µm. In this method, a laser beam hits the droplets, followed by reflection, diffraction, or absorption. The diffraction angle is inversely proportional to the size of the droplet, and so the light diffraction pattern allows us to obtain the droplet size distribution using Mie theory or Fraunhofer diffraction light theory and assuming that the droplet has a spherical shape.

During their data analysis, Sijs et al. (2021) distinguished the spatial and temporal distribution. The former is related to capturing images or determining droplet concentrations by processing all droplets within a snapshot of the spray. Shadowgraph imaging or laser diffraction methods can provide spatial distributions. On the other hand, with the PDPA, the temporal distribution of droplets can be produced as the flux of drops passes across an imaginary surface during a certain time interval. In this case, the velocity of drops in the spray is also important along with the drop concentration.

Given that in the main analysis Sijs et al. (2021) used the distribution from the raw VisiSizer data disregarding the built-in software corrections, the shadowgraph imaging, and PDPA techniques agreed very well for droplet sizes in the range from 10 µm up to ∼400 µm overall. There was only 0.7% discrepancy between measured volume mean diameters by these two methods.

As mentioned above, from (Kashdan et al., 2004, 2007; Sijs et al., 2021), the PDIA shadowgraph technique performed satisfactorily in measuring small droplets in high-speed sprays during lab experiments. However, it had not been tested to measure droplets in atmospheric clouds in spite of having more or less similar size ranges as laboratory sprays. Hence, the main motive of the current study was to investigate the applicability of the PDIA shadowgraph technique to measure the microphysical properties of atmospheric clouds, such as the DSD, DNC, and LWC which is elaborated on in the next chapters.

1.2 In-situ measurements at Schneefernerhaus

Airborne measurements can sometimes be impractical due to the weight or complexity of the setup. However, mountain observatories facilitate in situ measurements for such experiments while providing opportunities for the long-term sampling of cloud properties. The environmental research station Schneefernerhaus (in German: Umweltforschungsstation Schneefernerhaus, UFS) can be a nice example of such mountain observatories. The UFS is a former hotel in the Alps that is now Germany's highest research station. It was constructed at a height of 2650 m (47°25'00" N, 10°58'46" E) into the southern flank of the Zugspitze summit, the highest mountain in Germany (2962 m a.s.l.), approximately 300m below the peak.

Figure 1.13 illustrates the topography near the UFS which looks over a large, flat area bordered to the north, south, and west by a mountain ridge. As is shown in Fig. 1.13-c, the mountain ridge named "Schneefernerkopf" located in west of the UFS has an eroded part over 200m long, known as "wind hole" which directs the westerly wind over the UFS like a funnel (Risius et al., 2015).

For over 20 years, many different institutions have been working at the UFS on a variety of permanent studies on an inter- and trans-disciplinary basis (Beck and Neumann, 2020). There have been several recent atmospheric studies including in situ measurements and remote sensing of aerosols as well as greenhouse gases conducted at the UFS e.g. (Klanner et al., 2018; Ghasemifard et al., 2019; Wang et al., 2019, 2020). It has also been used as the measurement site in several campaigns on cloud research e.g. (Siebert and Teichmann, 2000; Wirth et al., 2012; Risius et al., 2015).

Siebert and Teichmann (2000) investigated the influence of liquid water content (LWC) on the behavior of sonic anemometers through an intercomparison experiment at the UFS, where the results obtained under different conditions (dry/cloudy) give no significant hint on such an influence. More-

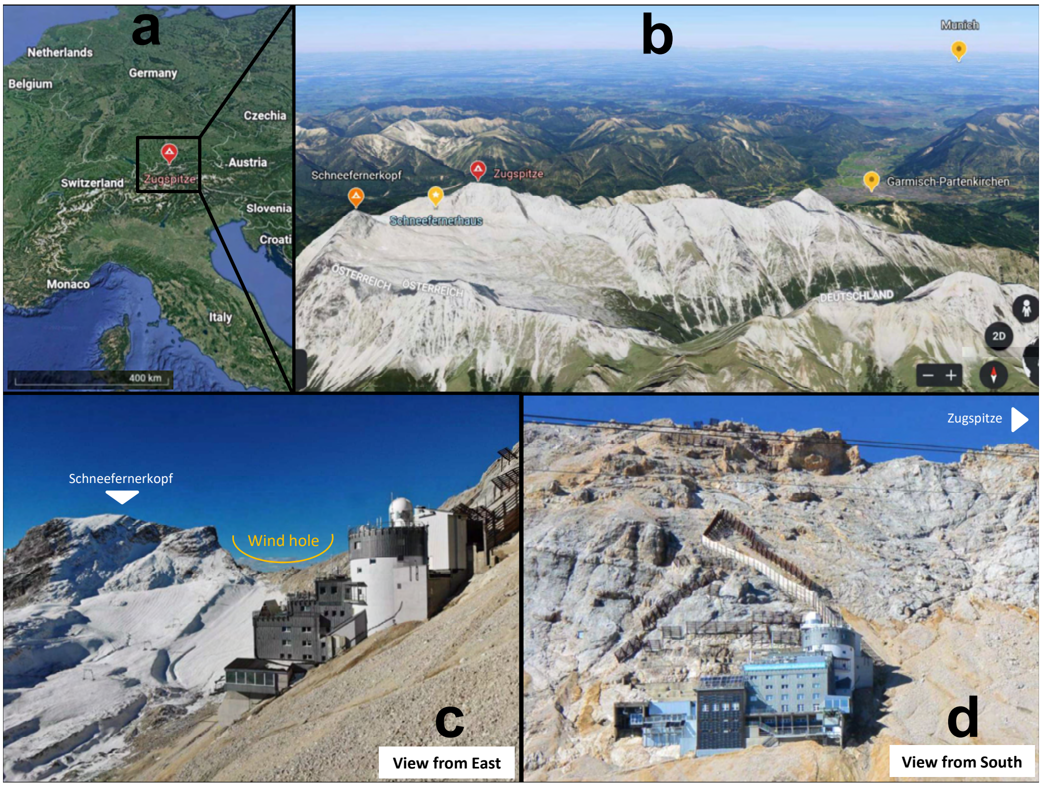

Figure 1.13: Topography near the UFS: (a,b) The UFS is located near the German-Austrian border, immediately south-west of Mountain Zugspitze in the German Alps (source: Google Earth); (c) View of UFS from the east during summer, showing also the Schneefernerkopf, a mountain ridge at the west of the UFS with its low spot named "wind hole"; (d) View of UFS from the south during summer where all 12 floors of the building, as well as the direction of Zugspitze summit, are shown (Credits: UFS GmbH, source: schneefernerhaus.de).

.

over, Wirth et al. (2012) chose Zugspitze for their systematic observations of banner cloud events. Later, using the meteorological data collected by the German Weather Service (DWD) from 2000 to 2012 as well as turbulence measurements recorded by multiple ultrasonic sensors in 2010, the UFS has been introduced as a well-suited station for cloud-turbulence research, especially for measurements that would be difficult to obtain from an airborne system (Risius et al., 2015; Siebert et al., 2015).

Figure 1.14 - from Risius et al. (2015) - shows the PDFs of the horizontal wind direction and the wind speed. As it is apparent, the winds at the UFS are mainly in the east-west direction while westerly winds can often have higher speed. The dominance of preferred wind direction can facilitate measurements with fixed instruments like cloud droplet size analyzers (Risius et al., 2015).

Moreover, in Figure 1.15 - from Risius et al. (2015) - fraction of time when the UFS is covered by clouds is shown for different months of a year. The chance of observing clouds at the UFS is higher during the summer, and especially in July with an average 30% probability of having the UFS covered in clouds. In addition, almost through the whole year (except for April), the westerly clouds have higher fraction values than easterly ones.

Siebert et al. (2015) used a PDI device to measure the DSD and the DNC of warm clouds. The data showed wide variation in the DNC with an almost uniform value of droplet size, clearly suggesting a prevalence of inhomogeneous mixing. The analyses of measured data, such as time series of the DNC, LWC, energy dissipation rate, etc., were performed in a manner similar to data recorded in prior airborne measurements (Siebert et al., 2006) in

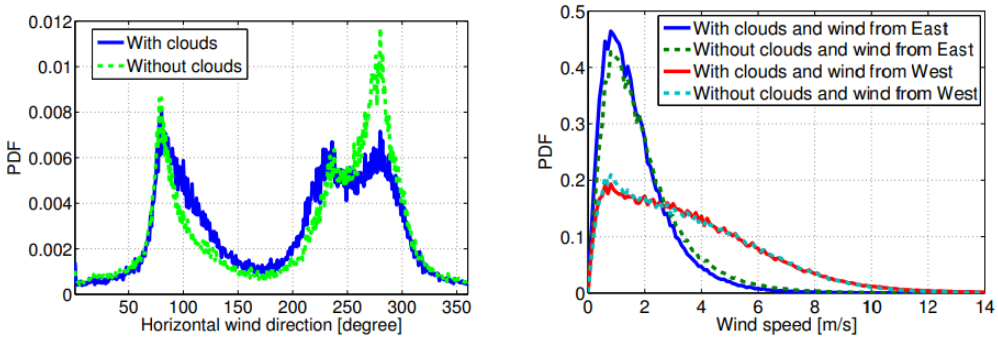

Figure 1.14: PDFs of the horizontal wind direction (left panel) and the wind speed (right panel). In the plot of the horizontal wind direction,0° corresponds to the wind coming from the north, and 90 and 270° correspond to the wind from the east and the west, respectively. The condition for "clouds" is that the relative humidity be above 99% (source: Risius et al., 2015).

order to compare the two approaches. Consequently, the results supported the argument that the UFS is a suitable location for detailed Lagrangian measurements of cloud droplets in turbulence.

Following the above-mentioned research, Bertens et al. (2021) performed a series of in situ particle tracking experiments on top of the UFS during summer 2019 in order to study turbulence-cloud droplet interactions. A Lagrangian particle tracking (LPT) experimental setup used in this study probes a volume of $\sim 40\times 20\times 12$ mm^3 with a spatial resolution of 5 µm and a temporal resolution of 0.1 ms which measures accelerations to within 0.1 m s^{-2}. They managed to compensate for the mean wind by sliding the setup, including three high-speed cameras, over a set of rails, driven by a linear motor up to 7.5 m.s^{-1}. This allowed them to study various dynamical quantities, such as the velocity auto-correlation, or the dynamics of clustering. Cloud droplets brightness as they passed through the sample volume was registered by each individual camera in addition to their positions as a function of time.

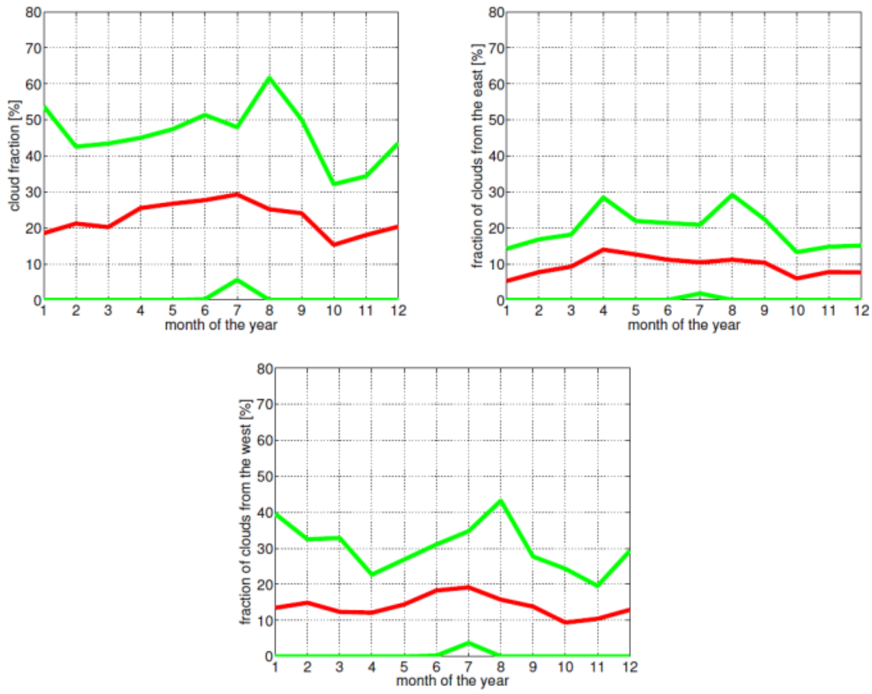

Figure 1.15: Fraction of time during which the UFS is covered by clouds during any month of the year. The red curve is the average cloud fraction, and the green curves are the maximum and minimum monthly values over the period of data analyzed. From the top to the bottom, the three panels are the total fraction of cloud covering, the fraction of clouds from the east and the fraction of clouds from the west (source: Risius et al., 2015).

This allowed for deducing each individual droplet size.

The results of droplet sizing with the LPT experiment compared to the data collected with a phase Doppler interferometer probe (PDI-FPDR) manufactured by Artium Tech Inc (see Fig. 1.16). For droplets larger than 35 µm in diameter, the sizes could be accurately estimated by a simple quadratic fit to the dependence of scattered light on droplet size. Although the LPT size distribution results indicated some oscillations below 35 µm, the comparison with the PDI-FPDR for droplets smaller than 14 µm showed different behaviors between the two instruments. The LPT experiment resulted in

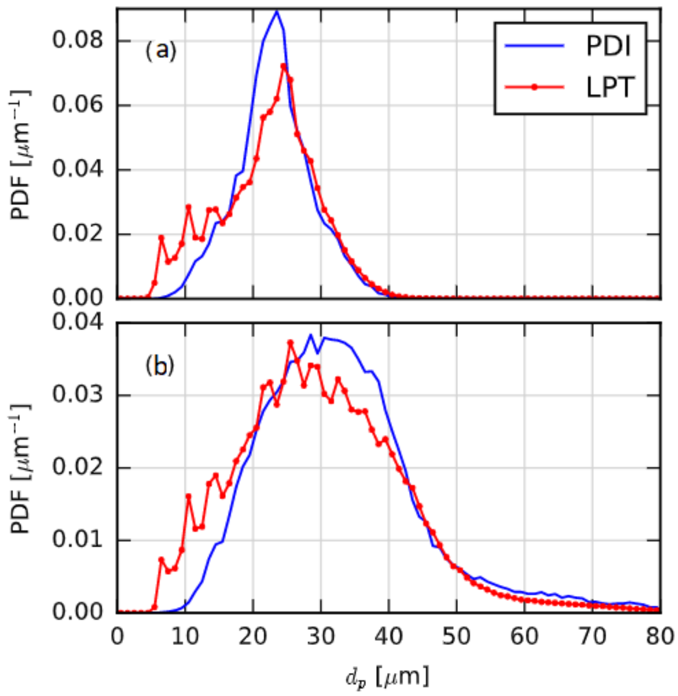

Figure 1.16: Comparison of inferred cloud droplet size distributions with those obtained with an Artium dual range flight probe phase-Doppler interferometer (PDI-FPDR). The size distributions compare well for both narrow (a) and broad (b) size distributions (source: Bertens et al., 2021).

higher values in small droplets size range ($d_p < 14$ µm) for both narrow and broad size distributions. Nevertheless, for diameters below 35 µm, the effects of Mie scattering must be taken into account for better accuracy (Bertens et al., 2021).

2

Instrumentation and methodology

In the current chapter, the main instruments, and methods used during this study to collect data on cloud droplets and precipitation particles are introduced. First, a description of the VisiSize D30 shadowgraph system is presented. Then, in the second part, the PDI-FPDR probe and laser optical Disdrometer, OTT Parsivel^2, are briefly described. These two instruments were used together with the VisiSize D30 during different measurements. A summary of the first part was already published in Nowak et al. (2021) while the PDI-FPDR probe description from the second part can also be found in Mohammadi et al. (2022a). More details regarding the modifications applied to the algorithms used in VisiSize D30 and PDI-FPDR in order to increase the accuracy of results are available in Appendices, Sects. A and B.

2.1 VisiSize D30 shadowgraph system

VisiSize D30 (hereafter called the VisiSize) is a complete shadowgraph system manufactured by Oxford Lasers Ltd. The VisiSize is capable of characterizing particles/droplets in various suspensions. A wide range of droplet information, such as droplet size, velocity, and shape provided by VisiSize makes the device potentially suitable for atmospheric research purposes, especially cloud microphysical measurements. However, its common industrial applications include the characterization of agricultural sprays, paint sprays, consumer aerosols, fire extinguishers, and automotive fuel injectors.

Figure 2.1-a shows a schematic of the system configuration taken from the instrument manual. The two main parts of the set-up are an infrared diode pulse laser with a diffuser and a high-resolution digital camera with suitable lens objectives as shown in Fig. 2.1-b. The lens magnification can be changed manually to adjust the resolution and extent of the sample volume to the object of study. For three selected options, instrument calibration was performed by the supplier. The instrument specifications and properties for these settings are listed in Table 2.1.

Table 2.1: Properties of the VisiSize D30 shadowgraph system for three different lens magnification settings provided by Oxford Lasers Ltd.

VisiSize D30 Specifications			
Sensor [pix × pix]	1952 × 1112		
Camera pixel [µm]	5.5		
Frame rate [fps]	30		
Wavelength [nm]	808		
Laser pulse duration [µs]	0.1 - 5.0		
Lens setting	×1	×2	×4
Magnification	1.49	2.97	6.12
Effective pixel size [µm]	3.69	1.85	0.90
Resolution [µm]	6.9	3.7	2.0
Field of view [mm × mm]	7.20×4.10	3.62×2.06	1.75×1.00
Depth of Field [mm]	50.0	16.6	5.2
Sample volume [cm^3]	1.48	0.123	0.0092
Volume rate [cm^3s^{-1}]	44.3	3.71	0.28

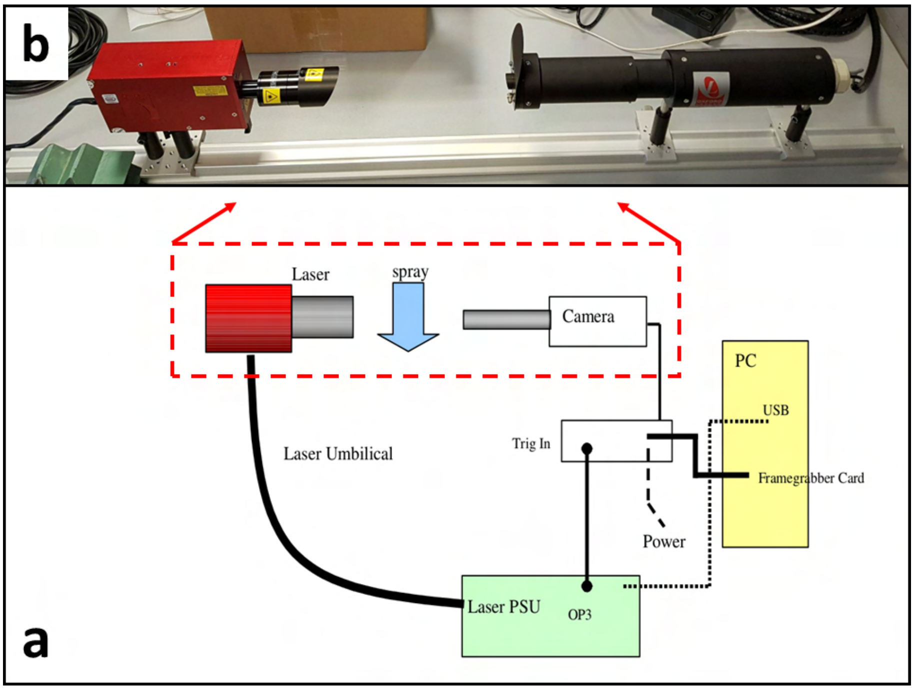

Figure 2.1: (a): A schematic of the system configuration for sizing; (b): Main components of the VisiSize, an infrared pulse laser with a diffuser (left) and a CCD camera with lens objective enclosed in a water-proof housing (right).

2.1.1 Droplet sizing

The VisiSize uses the PDIA shadowgraphy method which was first introduced by Kashdan et al. (2003). In this method, the region of interest is illuminated from behind by a diffused (incoherent) expanded laser light beam. Then, shadow images (shadowgrams) of droplets passing through the measurement volume are captured with a high-resolution digital camera at up to 30 frames or pairs of frames per second (fps).

The laser and the camera are jointly triggered so that a single laser pulse "freezes" the motion of droplets present within the measurement volume during each frame capture. Droplets detected inside the depth of field (DOF) are then measured based on their shadow images, and statistics regarding concentration or size distribution are built by processing a series of images. The captured images are either processed in real-time to determine particle position and size (live mode) or stored as graphic files (capture mode). In the former case, the output is only a list of droplets together with their properties (droplet file). Specific quantities included in the droplet file are explained in Table 2.2. The second complementary output file contains system settings used and a measurement summary with some basic statistics of the recorded droplet set (summary file).

For the capture mode, one can analyze captured images later tuning some parameters or access the raw genuine view of the particles. However, then the total time of uninterrupted measurement is limited by available computer RAM. Figure 2.2 shows an example shadowgram of cloud-like droplets produced in the laboratory and captured by the VisiSize in capture mode.

As mentioned, a built-in algorithm used in VisiSize software to process the

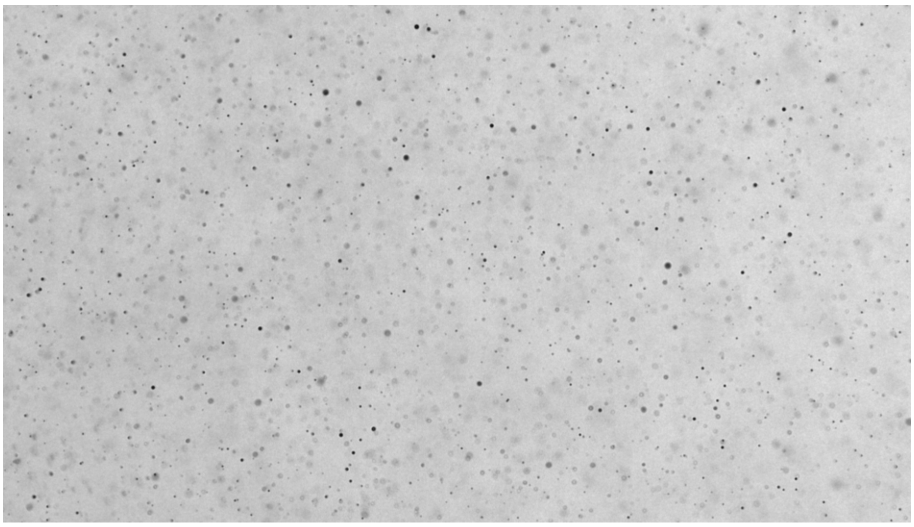

Figure 2.2: A typical shadowgram of droplets produced by an ultrasonic droplet generator in the laboratory and captured by the VisiSize. The image was taken during laboratory tests with a camera lens magnification settings of $\times 2$.

Table 2.2: Explanation of the parameters reported in output droplet file together with corresponding symbols used to denote them in the text.

Parameter	Symbol	Units	Description
Frame	j	-	Number of the image containing current particle
Particle ID	i	-	Particle number, unique across dataset
Area	A	µm^2	Estimated cross-sectional area, calculated from D
Diameter	D	µm	Estimated particle diameter, calculated based on A_p and A_h
Shape Factor	S_f	-	Measure of sphericity equal to the ratio of the principle moments of inertia of the shadow, taking values from 0 to 1, with 1 representing a perfect circle
X	x	pix	Horizontal position in camera plane
Y	y	pix	Vertical position in camera plane
Pixel Area	A_p	pix^2	Number of pixels in particle shadow with brightness below threshold T_p
Pixel Halo	A_h	pix^2	Number of pixels in particle shadow with brightness between thresholds T_h and T_p where $T_h < T_p$
Distance to Focal Plane	z	µm	Estimated axial position in the sample volume, calculated based on A_p and A_h; insensitive to direction, thus always positive

shadowgrams is based on the PDIA method. It stems from a basic observation that with increasing defocus (particle displacement out of the focal plane of the camera lens) the image of the object is more and more blurred which hinders the proper estimation of the size of the shadow. On the other hand, the range of axial positions guaranteeing acceptable sharpness of the shadow is usually quite limited. As a consequence, the probability of detecting particle inside such restricted sample volume might be often insufficient to collect meaningful statistics of the suspension in reasonable time.

To overcome the above-mentioned difficulties, Kashdan et al. (2003) applied a method compensating for the effects of imperfect focus. Basically, the displacement from the focal plane is estimated from the degree of image blurring, specifically the gradient of brightness at the edge of inner dark shadow. In their implementation, two threshold limits are determined for each analysed picture based on the histogram of pixel brightness. Both of them lie between the background intensity and the level corresponding to dark centers of droplet shadows as is shown in Fig. 2.3.

The upper threshold T_p separates the background from the particle image. All pixels below this value are assumed to belong to effective total particle image area A_p (with the equivalent diameter D_p). The lower threshold T_h distinguishes between the dark shadow interior and an outer gray “halo”. Pixel with intensities between T_h and T_p are counted to produce the estimate of particle halo area A_h (with the equivalent width D_h). Therefore, A_h belongs to A_p and has to be smaller.

With increasing defocus distance, the total area of particle image grows due to blurring until at some point it fades away into background making the object no longer distinguishable. Worth to mention, halo area A_h grows faster than total area A_p because it extends both into outer and inner direction, taking over respectively the background and the interior pixels. Ideally, for object standing exactly in the focal plane A_h should tend to zero. However, it is never the case due to intrinsic diffraction caused by finite aperture of the lens. This effect might be particularly important for small object of the size close to the optical resolution of the system.

Particle total area A_p and halo area A_h can be regarded as directly measured

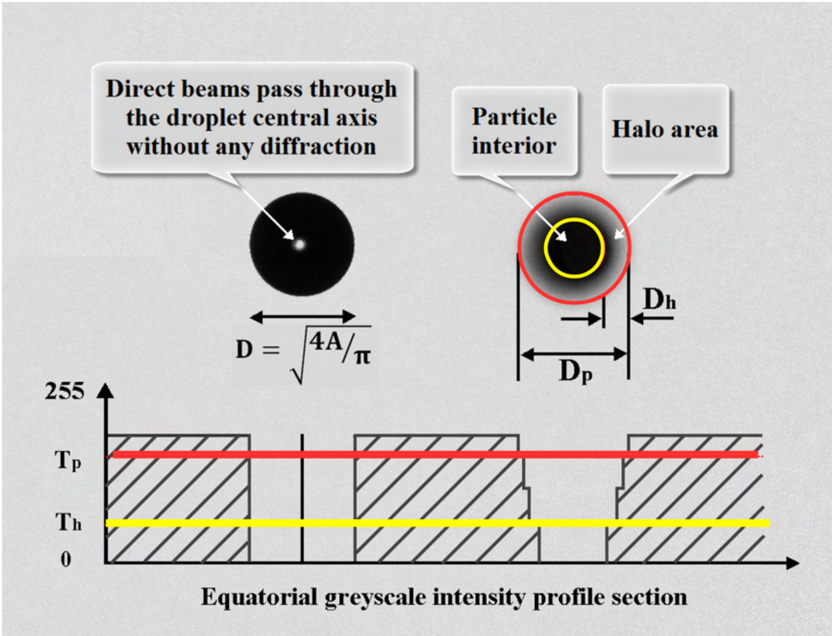

Figure 2.3: Illustration of the thresholds used in PDIA method, showing two actual sample droplets captured by the VisiSize: in-focus droplet [left] and defocused droplet [right]. The grayscale intensity profiles below them illustrates applied thresholds as well.

quantities. Both true particle diameter D and estimated defocus distance z are derived from them. The exact conversion is determined with experimental calibration, separately for each lens setting. The pictures of calibration targets of known sizes are taken at known distances away from the focal plane. Applying the sizing algorithm to the collected data, some function is fitted to approximate the relationship $A_p(D, z)$ and $A_h(D, z)$. For the present VisiSize D30 model, calibration was performed by Oxford Lasers for three possible lens magnification settings ($\times 1$, $\times 2$ and $\times 4$) and incorporated into the software.

In principle, for perfect focusing the halo area A_h should tend to zero, since then the image consists only of a dark disk with sharp edge around. Certainly A_h grows with the distance between actual particle position and the focal plane. The halo is formed exactly around the dark interior of the shadow, i.e. each point on an initially very sharp edge spreads equally in all directions, smoothing the intensity gradient and creating halo of area which scales with the perimeter length and the amount of defocus. For objects with shape close to a circle, the perimeter is proportional to the diameter which leads to a scaling $A_h \sim Dz$. However, even a point source, while being out of the focal plane is mapped to a circle of confusion in image plane (camera chip). Therefore A_h should be growing function of z even in case of size D tending to zero. The simple linear relation satisfying the above properties is as follows:

$$A_h = a_1 D z + a_2 z \tag{2.1}$$

where a_1 and a_2 are calibration constants for a given lens magnification.

As described above, with increasing defocus distance z, halo around the dark interior develops at the cost of both the background pixels and the inner shadow pixels. The whole A_h is included in total particle pixel area A_p, so only the outward growth affects the value of A_p. Outward part of the shell is larger than inward one, hence the proportionality factor would be close to but slightly higher than 0.5. Obviously, in focal plane the image area is dependent on the true cross-section of the physical object, but A_p is composed of pixels of finite size which disturbs the perfect representation of smooth shapes. Consequently, effective diameter length might be diminished by the amount of the order of pixel size.

Moreover, even for the focal plane diffraction comes into play and hinders perfect imaging - objects always appear slightly larger than in reality which is important especially for small droplets. The enlargement of diameter due to diffraction should be of the order of the optical resolution of the lens system. All the effects can be taken into account in the formula of the form below:

$$A_p = a_3 A_h + \frac{\pi}{4} \frac{(D + a_4 + a_5)^2}{\mathrm{pix}^2} \tag{2.2}$$

where the constants a_3, a_4, a_5 and pix describe halo blurring, pixelization, diffraction and effective pixel size, respectively. Note that A_p is specified as the number of pixels, hence the unit conversion factor pix^2 is needed. Having the values of A_h and A_p obtained from the image of the specific droplet, both the diameter D and the defocus distance z can be calculated by inverting Eqs. (2.1) and (2.2).

2.1.2 DNC calculations

In order to calculate the DNC, the effective sample volume for the VisiSize must be determined first. According to Eqs. (2.1) and (2.2), the halo grows linearly with droplet diameter whereas the total image area grows quadratically. This means that for a given defocus distance z, the halo should constitute a larger fraction of the whole image for small droplets than for large ones. With increasing z, the halo fills the image much sooner for small objects, and their shadows fade more quickly into the background, meaning that they are no longer detectable. Such qualitative reasoning explains the intuitive fact that the range of z within which the object can be detected depends on the object size. For instance, the sample volume depends on the cloud droplet diameter, which in turn affects the measurement of the DSD. Kashdan et al. (2003) showed that, to a reasonable accuracy, the range of possible defocus distances (depth of field, DOF:$[-z_{\texttt{def}}, +z_{\texttt{def}}]$) grows linearly with particle diameter(D_i):

$$z_{\texttt{def}} = a_6\, D_i \tag{2.3}$$

where the proportionality factor a_6 comes from experimental calibration. The sample volume is then equal to the product of the default DOF and the effective area of the camera sensor S (i.e. field of view, FOV):

$$V = 2\, a_6\, D_i S \tag{2.4}$$

The FOV is calculated from the formula below:

$$S = (L_x - D_i)(L_y - D_i) \tag{2.5}$$

where L_x and L_y denote the size of the FOV in µm.

Hence, the default sample volume for the kth size bin is obtained as:

$$V_k^{\texttt{def}} = 2\, z_{\texttt{def}}|_{D_k}(L_x - D_k)(L_y - D_k)\ . \tag{2.6}$$

The droplet number concentration normalized by size can be calculated for each size bin from the formula below:

$$N_{\texttt{VD}}^{\texttt{def}}\langle k\rangle = \frac{M_k}{F\, \Delta D_k\, V_k^{\texttt{def}}} \tag{2.7}$$

where $M_k = |\{i : D_k \leq D_i < D_{k+1}\}|$ is the number of counts within bin k, $\Delta D_k = D_{k+1} - D_k$ is the bin width, and F is the number of frames included in the analysed series.

Finally, the total DNC can be calculated by suitable integration with respect to the whole range of diameters, which is in practice a sum over the size bins:

$$N_{\mathtt{V}}^{\mathtt{def}} = \sum_{k} N_{\mathtt{VD}}^{\mathtt{def}} \langle k \rangle \, \Delta D_k \; . \tag{2.8}$$

2.1.3 Velocimetry

The VisiSize software is by default in diameter mode, where only droplet sizes are recorded and analyzed. In order to also enable the velocimetry, one must choose the velocity mode. After adjusting some additional settings (e.g. maximum search radius, maximum deviation angle, and flow direction), droplet size and velocity can be measured simultaneously in velocity mode by using either of the following two methods.

"Image pairs" is a method where pairs of consecutive frames are processed and after detecting a droplet within both images, the droplet velocity is calculated according to its position change between the frames. Another way to measure velocity is called "double exposed" in which during every camera exposure, two pulses are sent from the laser. Hence, every detected droplet should cast two shadows in each frame.

According to the manufacturer, the latter method is not recommended whenever it is possible to use the former one, in order to avoid saturation of the camera. Properly adjusting the above-mentioned settings in the velocity mode is crucial for obtaining accurate velocity. Otherwise, the device may find a false droplet, within the second frame or in the same frame as the second shadow (based on the selected method).

2.2 Other instruments alongside VisiSize

2.2.1 Phase Doppler Interferometer Probe

The Phase Doppler Interferometer, Flight Probe - Dual Range (PDI-FPDR; hereafter called PDI probe) is a droplet spectrometer constructed by Artium Technologies, Inc. The PDI is a laser-based diagnostic instrument for simultaneously measuring size and velocity of individual spherical droplets in poly-disperse flow environments.

The instrument utilizes the well-known technique of phase Doppler interferometry. The technique is based on the fact that the phase shift of the light scattered from two intersecting beams, as spherical droplet passes through them, is proportional to the droplet size as shown in Fig. 2.4. The theoretical description of the method and details regarding the PDI probe have been already provided in the literature (e.g. Bachalo, 1980; Bachalo and Houser, 1984; Chuang et al., 2008; Bachalo and Sankar, 2016). Hence, we add just a brief explanation in this section.

Droplet sizing and velocimetry

A diode-pumped solid-state (DPSS) laser with 532 nm wavelength is used as a light source for the PDI. The dual size range version combines two PDI instruments (channels) for small and large size ranges in a compact package (see Fig. 2.5-b). According to the manufacturer, the PDI channel 1 is able to measure size and velocity of droplets from 0.5 to 100 µm whereas the channel 2 can cover up to 1000 µm.

The droplet velocity is measured by the method typically used for laser

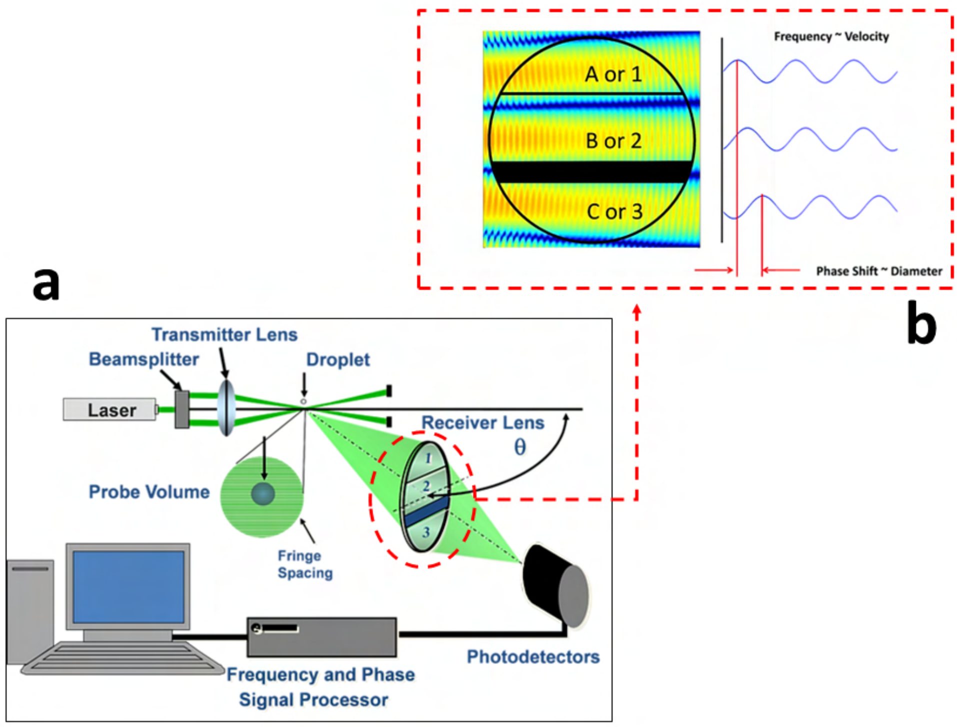

Figure 2.4: (a): Configuration of a basic phase Doppler interferometer (PDI) system; (b): Calculated interference fringe pattern with the segmented receiver placed over the pattern showing how the fringe spacing can be measured using the phase shift information (Source: Artium Tech. Inc.).

Doppler velocimetry. That is, as a particle crosses the interference fringes created by the two intersecting coherent laser beams, it refracts or reflects the local light intensity onto the receiver. The light intensity pattern projected onto the receiver and directed to the photo multiplier tubes produces a typical Doppler burst signal whose frequency is directly related to the velocity of the droplet (see Fig. 2.4-b).

The droplet magnifies the interference fringe pattern onto the receiver. The degree of the magnification is related to the droplet size, and is measured by comparing the spacing of these fringes on the receiver detectors (spatial

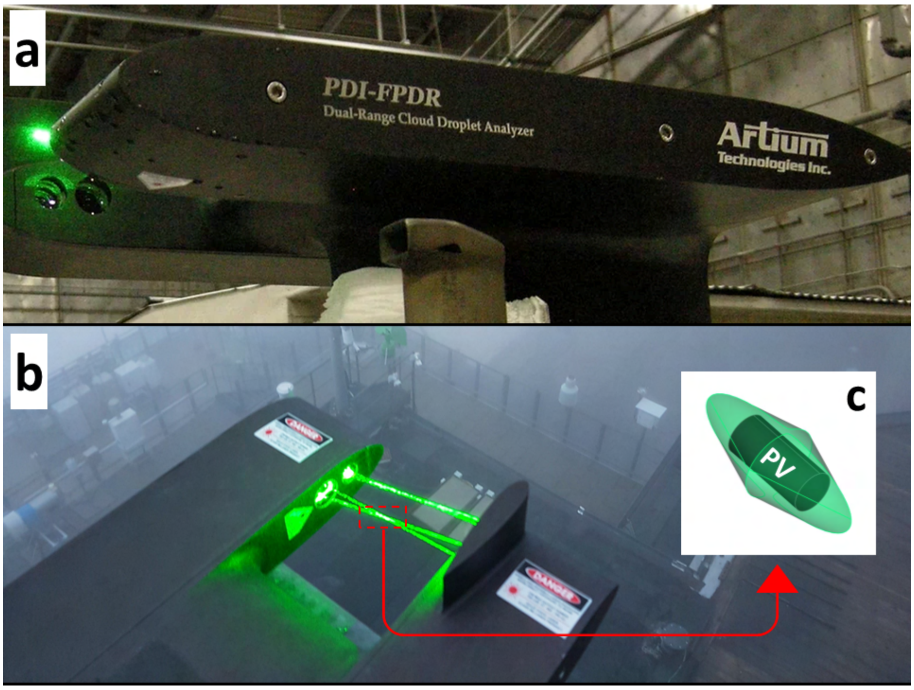

Figure 2.5: (a) The PDI probe manufactured by Artium Tech. Inc.(Source: Artium Tech. Inc.); (b) The photo was taken during a ground-based cloud measurement in the UFS while both PDI channels were on; (c) A magnified schematic illustration of the cylindrical probe volume (PV) within the intersection of two laser beams.

wavelength) and the fringe spacing (see Fig. 2.4-b). A spatial wavelength is determined by using the phase shift of the signal between the detectors in the time domain along with the calibrated spacing of the detectors.

Any cloud droplet, in order to be measured by a PDI system, must pass through the probe volume (PV), which is defined by the diameter of the Gaussian focused laser beam as well as the slit aperture width in the receiver. The shape of the probe volume can be estimated as a cylinder with oblique ends (see Figure 2.5-c). While the cylindrical height of PV is assumed to be constant, the diameter of PV base is enlarged by increasing the droplet size. The larger the droplet is, the better it scatters, and therefore the less incident light it requires to be detected. Hence, taking into account the Gaussian intensity profile of laser beam, the PDI have larger PV for larger droplet sizes.

Figure 2.6 demonstrates how size and position can affect the scattered light from a droplet, and consequently its detection by the PDI. While droplets D_1 and D_2 have different size and position in the yz plane, both can be detected by the PDI as they pass through their size-dependent PV or in other words, they scatter enough light back to the receiver. However, droplet D_3 with the same size as D_2, but at a further distance from the yz plane, cannot be detected by the PDI as it scatters lower intensity than minimally required.

Since the PV is size-dependent, the number of droplets in each size class of the distribution is multiplied by the probe volume correction (PVC) factor to reflect the change in sampling volume with droplet size. The PVC factor is simply the ratio of the probe area (PA) for the maximum droplet size bin to the probe area of each individual size bin D. In order to calculate the probe area, the following formula can be used:

$$PA(D) = \beta\omega\sqrt{log(\frac{D}{D_{\text{min}}})}\ , \tag{2.9}$$

where β is a constant based on the aperture and the angle of detector, and equals twice the height of PV. ω is the laser beam waist, and D_{min} is the effective minimum diameter for which $PA(D_{\text{min}}) = 0$. Any droplet smaller than D_{min} will not be detected by the PDI even if it passes through the center of the probe area (with the highest light intensity). The values for ω and D_{min} are calculated by the PDI software after each measurement by fitting a model to the raw data.

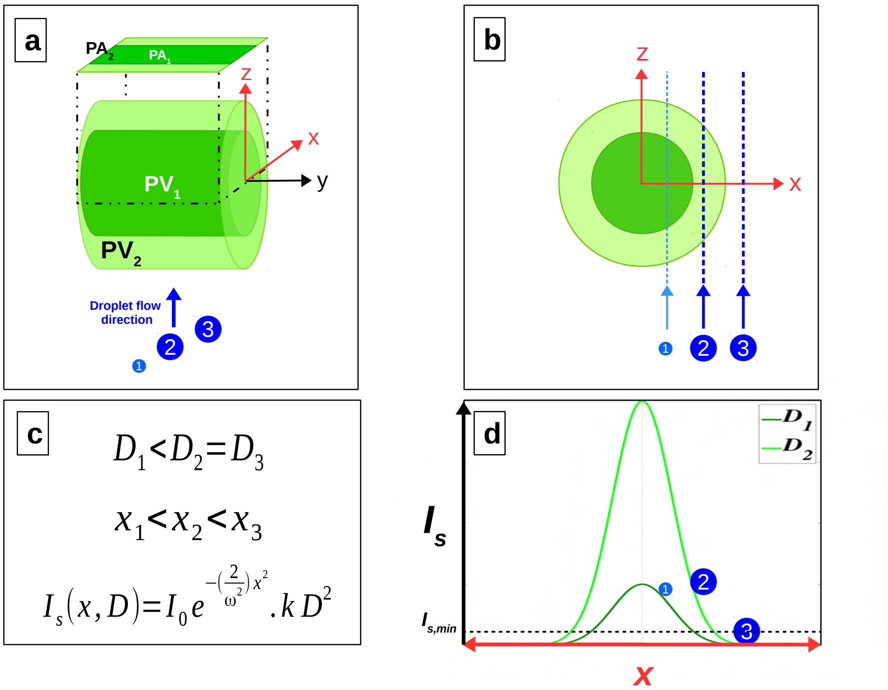

Figure 2.6: (a): Schematic representation of the cylindrical effective probe volume (PV) and probe area (PA) of the PDI for two different sizes of three passing droplets; (b): side view of the panel (a) showing trajectories of the droplets located at different positions (x) from the yz plane; (c): relations between size (D) and position (x) of the droplets along with the formula of scattered intensity (I_s) as a function of x and D (where k is an instrumental constant); (D): qualitative graphs of $I_s - x$ illustrating the scattered intensity of each droplet based on its x and D as well as minimum I_s below which the droplet cannot be detected.

DNC calculations

There are two methods used by PDI software in order to compute the DNC, which are referred to as ”swept volume” and ”transit time” methods in the instrument manual. In the former one, the total corrected count (corrected for probe volume) is divided by the swept volume to calculate the DNC and is given as:

$$N_V^{SV} = \frac{1}{(PA)(t_{Tot})} \sum_i \frac{n_{c(i)}}{\overline{|v_i|}} \; . \tag{2.10}$$

A separate average absolute velocity is calculated for each size bin i to eliminate the velocity biasing on the sampling statistics and is given as:

$$\overline{|v_i|} = \frac{\sum_j |v_{i,j}|}{n} \; , \tag{2.11}$$

where $v_{i,j}$ refers to the velocity of j-th droplet within the i-th size bin. j and i are the droplet and size bin indices, respectively.
In transit time method, the DNC is determined using the transit times for the droplets as they pass the sample volume. The transit time is the amount of time that the droplet spends within the probe volume. This method uses the computed ratio of time duration when there is a droplet in the probe volume, to the total sample time for the measured distribution at that point. Transit time ratio divided by the probe volume yields the DNC, and given by:

$$N_V^{TT} = \frac{1}{t_{Tot}} \sum_i \frac{\sum_j Tt_{i,j}}{PV_i} \; , \tag{2.12}$$

in which $Tt_{i,j}$ refers to the transit time of the j-th droplet from the i-th size bin. This method is applied for each size class to accommodate the size biasing of the probe volume as a function of droplet size.

Both methods rely on an accurate probe area calculation. The transit time method will work best as long as the beams are partially Gaussian at the intersection. The swept volume method works well if the trajectories of the droplets are in the direction of the velocity component measured for a one-component system.

2.2.2 Laser optical disdrometer

OTT Parsivel^2 (hereafter called Parsivel) is a laser-optical disdrometer, manufactured by OTT Hydromet GmbH, for capturing particle size and velocity of the liquid and solid precipitation. When it comes to in situ measurements of precipitation, disdrometers are considered the primary instruments. They measure the DSD of raindrops and precipitation particles at a given location. The first impact disdrometer was used by Joss and Waldvogel Joss and Waldvogel (1967). Later, the 2-Dimensional Video Disdrometers (2DVD) Kruger and Krajewski (2002) and optical disdrometers Hauser et al. (1984); Löffler-Mang and Joss (2000) were developed. The optical disdrometers are relatively inexpensive, long-lasting, and reliable instruments that are particularly well suited for use in a network to study the small-scale variability of DSD Jaffrain and Berne (2011); Tapiador et al. (2010). So far, Parsivel has been used for snowfall measurements in several studies (e.g., Egli et al., 2012; Löffler-Mang and Blahak, 2001; Tokay et al., 2007; Yuter et al., 2006) because of its ability to distinguish between solid and liquid precipitation. Its measurement technique was already described in detail by Löffler-Mang and Joss (2000).

As is shown in Fig. 2.7, the Parsivel uses a laser-optical sensor to measure

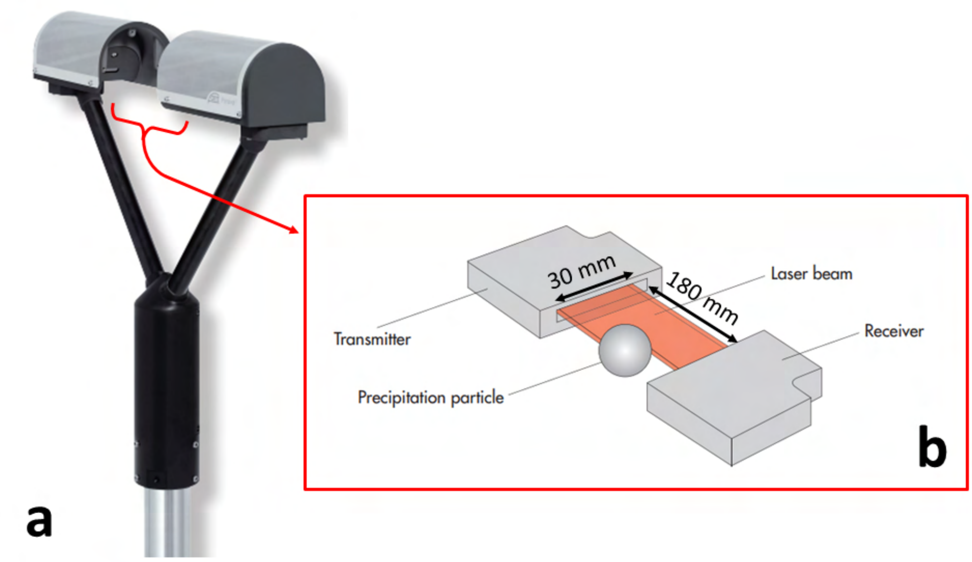

Figure 2.7: (a): A photo of OTT Parsivel^2 Laser-Optical disdrometer showing its symmetrically arranged measuring heads; (b): A schematic illustration of the functional principle of the disdrometer showing the measuring area between the transmitter and receiver.

precipitation. The transmitter unit of the sensor generates a flat, horizontal beam of light that the receiver unit converts to an electrical signal. This signal changes whenever precipitation falls through the beam anywhere within a measuring area equal to 180×30 mm (= 54 cm^2). The diameter and velocity of a precipitation particle are then determined by measuring the shadow it casts and how long it casts that shadow (i.e. the extinction signal duration; Löffler-Mang and Joss, 2000). The splash protection attached to the sensor head prevents precipitation particles from deflecting off the housing, falling into the laser beam, and thus falsifying the measurements (Source: OTT GmbH).

The Parsivel divides the precipitation into classes for velocity and diameter and records the number of hydrometeors measured per class over an integration time. From collected data on the size and velocity of precipitation particles, other parameters such as Size spectrum, type of precipitation, Kinetic energy, radar reflectivity, etc. can be derived. Hence, the Parsivel can be used not only in precipitation measurements, but also for monitoring road conditions, early flood warning, and erosion modeling (Source: OTT GmbH). The size range of measurable hydrometeor starts from 0.25 mm and goes up to 8 mm for liquid precipitation particles, and 25 mm for solid precipitation particles. Technical data of the Parsivel disdrometer provided by OTT HydroMet are listed in Tab. 2.3.

Table 2.3: Technical data of OTT Parsivel^2 Laser-Optical disdrometer provided by OTT HydroMet.

OTT Parsivel^2 Specifications	
Optical sensor, laser diode:	
Wavelength	650 nm
Output power (peak)	0.2 mW
Laser Class	1 (IEC/EN 60825-1:2014)
Measuring surface (W×D)	180×30 mm (54 cm^2)
Measuring ranges:	
Particle size	0.2 - 8.0 mm (liquid phase)
	0.2 - 25.0 mm (solid phase)
Particle velocity	0.2 - 20.0 m.s^{-1}
Classification	32 classes
Measurement accuracy*	± 1 size class (0.2-2.0 mm)
	± 0.5 size class (>2.0 mm)
Types of precipitation	8 types: drizzle, drizzle/rain, rain, mixed rain/snow, snow, snow grains, sleet, hail

* Proof under laboratory conditions using an OTT test system with reference particle simulation of 0.5 mm, 1.0 mm, 2.0 mm and 4.0 mm

3 Laboratory experiments with monodisperse droplets

This chapter is dedicated to a series of laboratory experiments with the VisiSize at the Turbulence Laboratory of Max Planck Institute for Dynamics and Self-organisation (MPIDS) in Goettingen, Germany. The tests were carried out by me using a monodisperse water droplet generator to characterize the instrument performance in terms of particle sizing which affects the relevant statistics of cloud droplets including the droplet mean diameter and droplet size distribution (DSD). The results are already published in Nowak et al. (2021). Moreover, it is worth noting that prior to these experiments, another series of tests with the VisiSize on polydisperse cloud-like droplets were performed by my colleague, J. L. Nowak at the Fluid Mechanics Lab of Institute of Geophysics, University of Warsaw (IGF-UW). That experiment together with its key findings are briefly presented in Appendix A.

3.1 Experimental set-up

Monodisperse water droplets were generated with Flow Focusing Monodisperse Aerosol Generator 1520 (FMAG) manufactured by TSI Inc. and measured with the VisiSize. The FMAG uses a periodic mechanical vibration to break a narrow jet of a liquid into droplets of the desired size (within the range of 15 to 72 µm in diameter). Efficiency and accuracy of droplet generation are enhanced by aerodynamic flow focusing and charge neutralizer making FMAG a common tool applied for calibration of aerosol spectrometers and droplet sizing instruments (Duan et al., 2016).

Table 3.1: Settings of the FMAG droplet generator used during sizing experiments.

FMAG 1520 settings			
Inlet air [psi]	10.0		
Dilution air [$L\,min^{-1}$]	5.0		
Focusing air [psi]	1.0		
Flow rate [$mL\,h^{-1}$]	2.0	8.0	18.0
Vibration frequency [kHz]	130	70	50
Droplet size [µm]	20.13	39.25	57.55

During the experiment, pressurized N_2 (1.0 psi) was used as the flow-focusing gas and ultra-purified H_2O as the liquid. Droplet size was controlled by adjusting two parameters: liquid flow rate and vibration frequency. Three different settings were applied resulting in droplet diameters of 20.13, 39.25, and 57.55 µm as obtained with the formula provided by the manufacturer (see the settings listed in Table 3.1). The geometrical standard deviation among the generated droplet population is supposed to be 1.05 or smaller (Duan et al., 2016). The smallest diameter was chosen to ensure a relatively narrow spectrum as I observed significant broadening for high vibration frequency which is necessary to generate smaller droplets. Presumably, this results in less accurate breakage of the fluid stream or more frequent collisions.

The experimental setup was arranged in two different configurations (see Fig. 3.1). The first was without a cylindrical case over the nozzle, with the VisiSize sample Volume (SV) as close as possible to the nozzle head

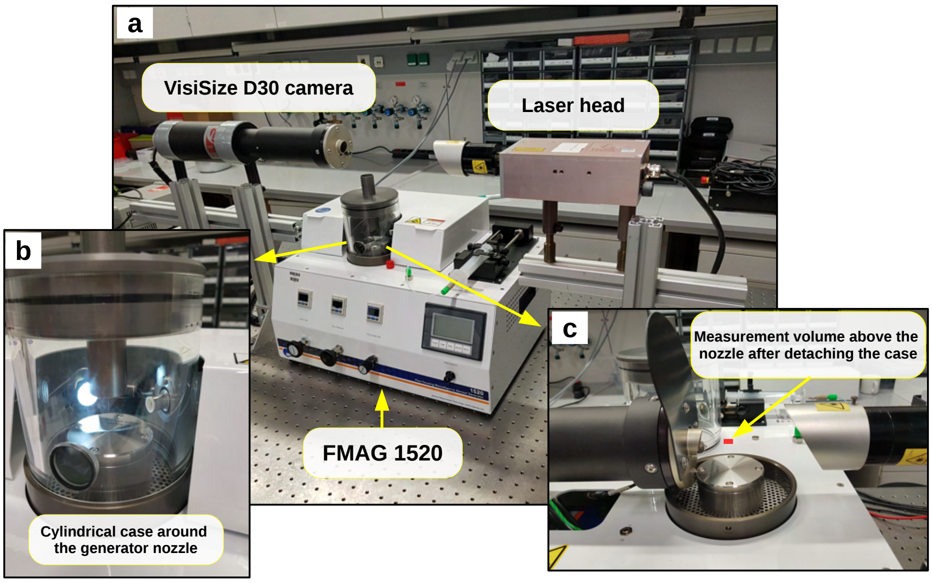

Figure 3.1: Experimental setup for studying sizing performance of the VisiSize; (a) The VisiSize D30 is located above the exit of the FMAG droplet generator to measure droplets; Two different configurations are used: (b) with the cylindrical case above the nozzle or (c) without the cylindrical case.

($\sim$ 4.5 cm). The second was with the case and the dilution air (flow rate of 5 L min^{-1}) forcing the droplets to leave the cylinder. The SV of VisiSize was then located above the cylinder exit ($\sim$ 18.5 cm over the nozzle head).

3.2 Results and discussion

Sample shadow images of droplets produced by the FMAG and captured by the VisiSize are reproduced in Fig. 3.2. The configuration of the setup was as in panel (c) of Fig. 3.1, i.e. without the case covering the nozzle. Despite the population of droplets supposed to be monodisperse, one can see the range of sizes. For each droplet size specified by the parameters of FMAG, a series of images was taken by the VisiSize with three different lens magnification settings ($\times 1$, $\times 2$, and $\times 4$).

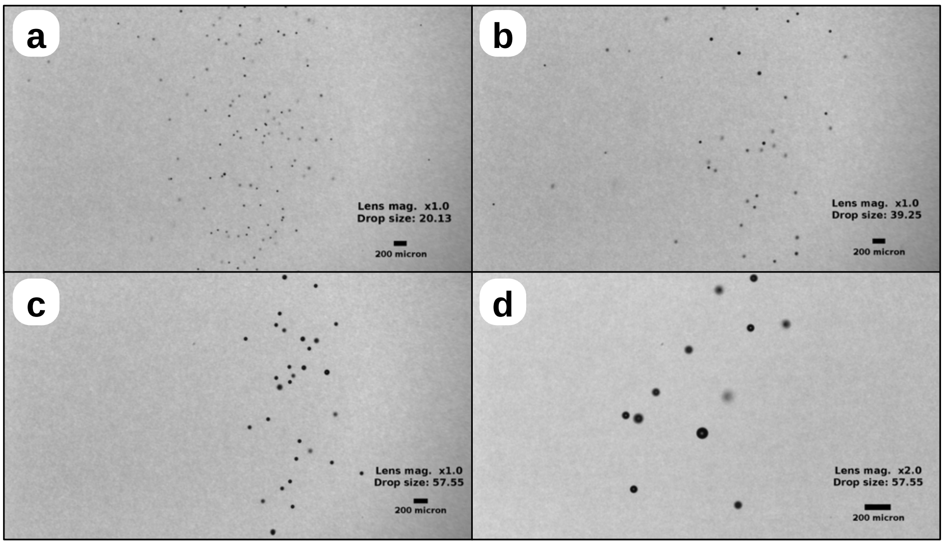

Figure 3.2: Sample shadow images captured with the VisiSize D30 showing droplets of different sizes generated with the FMAG.

Results are presented in Fig. 3.3 in the form of probability density function (PDF $\equiv N_{\mathtt{VD}}/N_{\mathtt{V}}$; see Sect. 2.1.2). Such measure was chosen in order to compare the DSD between different magnifications and measurements substantially different in total droplet concentration which itself is not a quantity of interest in the current analysis.

Surprisingly, all histograms contain multiple peaks which suggest quite frequent collisions between droplets on their way from the nozzle to the measurement volume. The position of the first peak corresponds well with the generated droplet size in most cases. Its width can be attributed to the inevitable spread of actual generated droplet diameters as well as to the

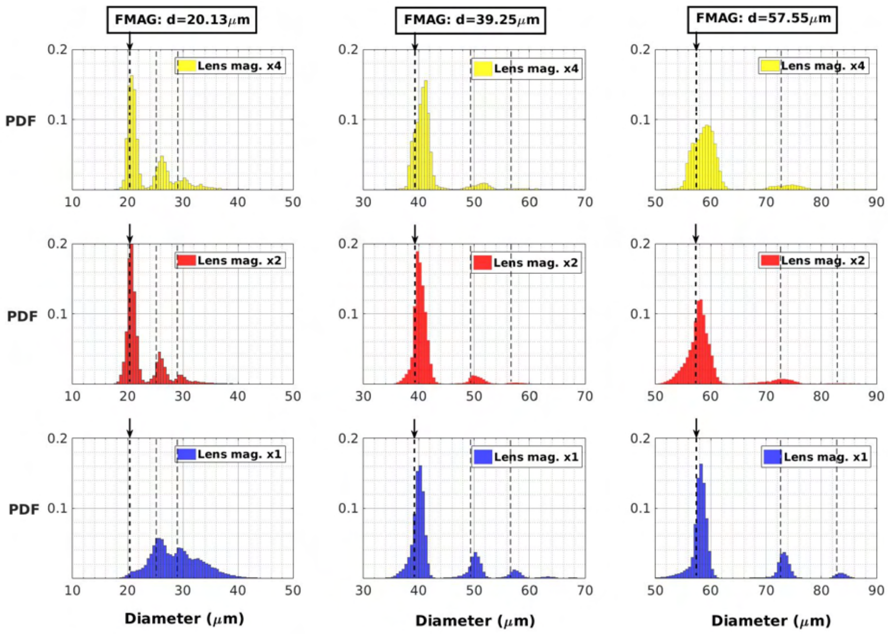

Figure 3.3: Probability distributions of droplet size measured by the VisiSize D30 in the configuration as in fig. 3.1 panel (c) (distance between sample volume and nozzle head is $\sim 4.5\,\mathrm{cm}$), for different camera lens magnifications and different FMAG output droplet sizes. The initial size of the generated droplets as well as the size after double and triple collisions are marked with vertical lines.

imperfect imaging and sizing of droplet shadows. Moreover, comparing the positions of the second and third peaks with the diameters of droplets formed after the collision of two and three smaller droplets, hereafter called double and triple collision respectively, shows reasonable agreement.

Left-side skewness of the tails suggests partial evaporation. Although in general the effect of evaporation is expected to be more significant for small droplets, the skewness is evident for 39.25 and 57.55 μm measured with the lens settings $\times 1$ and $\times 2$. It can be related to the size of sample volume which increases with the effective pixel size (decreases with magnification) as well as with the particle size (i.e. from the top-left to the bottom-right panel in Fig. 3.3).

The position of the nozzle exit was adjusted so that the center of the FMAG-generated droplet stream is as close as possible to the focal plane of the VisiSize. The droplets more distant from the central axis of the stream are more likely partially evaporated because of the longer travel and exposure to the dry air blown from the area around the nozzle. Those could be detected when a large Sample volume is available but would be missed in case of having a smaller sample volume (e.g. in lens magnification settings ×4). Of course, this is only one of the effects which could have contributed to the observed result together with the ambient air properties, the velocity of the droplets, or some interactions among them.

Taking into account the geometric standard deviation of generated droplets (1.05), histogram bin width (0.5 µm), and evaporation, the sizing by the VisiSize seems pretty accurate. Only in case of smallest droplets (20.13 µm) and lowest lens magnification (×1), the reported diameters seem to be significantly biased. This issue is probably of instrumental origin and might correspond to non-uniform illumination of the FOV which also caused inhomogeneity of detection of relatively small objects for that particular lens settings (Sect. 3.5 from Nowak et al., 2021).

In Fig. 3.4 - top, flow rate (Q) and average droplets velocity between the measurement cases with FMAG are compared with each other while in the bar chart below it, the percentage of detected droplets for each corresponding case is shown, categorized in three groups of single droplets, drops after a double collision, and drops after a triple or more collision. As mentioned earlier, these categories are constructed based on the observed peaks in the DSD histograms so that the droplets with a volumetric size twice larger than the size of generated droplets by FMAG are considered double collisions, and so on.

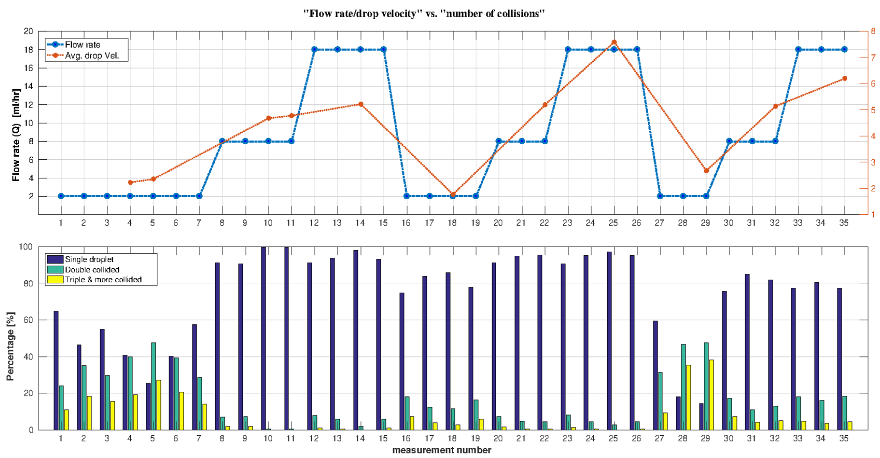

Figure 3.4: All analyzed measurement cases from the second series of lab experiments with the VisiSize D30. Top: Comparison of generated flow rate (Q) with the FMAG and the measured average droplet velocity by the VisiSize among the analyzed cases. Bottom: Corresponding percentage of each droplet size category in the measurements based on DSD histogram peaks (single droplet, double collision, and triple & more collision).

It can be seen in Fig. 3.4 that the flow rate increases the average droplet velocity also increase, while the percentage of collided drops falls. For those cases, The majority of detected droplets (above 80%) are considered single droplets which is not surprising if we notice that by increasing the flow rate the droplets pass the path from the nozzle head to the sample volume faster, and there is less opportunity for collision between them before they reach to the sample volume and captured by the VisiSize camera.

The droplet collisions phenomenon during the experiments is further corroborated with measurements conducted in the configuration as in Fig. 3.1 panel (b), i.e. with the cylindrical case over the nozzle and longer distance

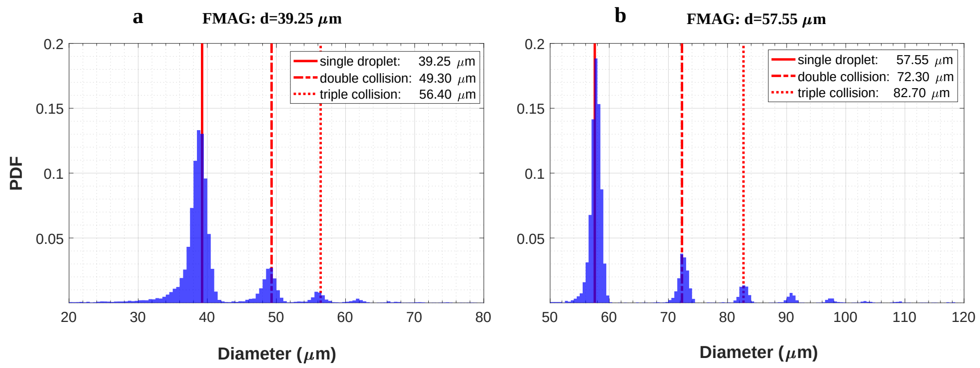

Figure 3.5: Probability distributions of droplet size measured by VisiSize D30 in configuration as in fig. 3.1 panel (b) (distance between sample volume and nozzle head is $\sim 18.5\,\mathrm{cm}$), for camera lens magnification setting $\times 1$. The initial size of the generated droplets as well as the size after double and triple collisions are marked with vertical red lines.

between nozzle exit and the shadowgraph sample volume (~ 18.5 cm). A longer path enhances the chance of collisions and the effects of evaporation. The former can be clearly seen in histograms presented in Fig. 3.5.

Consecutive peaks correspond to single generated droplet, double collision, and triple collision as calculated simply by summing the volumes. Here, lens magnification setting $\times 1$ was selected due to the largest sample volume, and subsequently, the best statistics it can provide. This gives a better estimation of less frequent events in the probability distribution. More distant peaks can be traced better in the case of the largest droplet size suggesting the probability of high - order collisions might increase with size. This can be expected by recalling extensive studies on cloud droplets collision kernels (Devenish et al., 2012; Grabowski and Wang, 2013). Left - skewed tails are also visible, particularly for the first peak, which is the consequence of evaporation on the way of 18.5 cm from the nozzle.

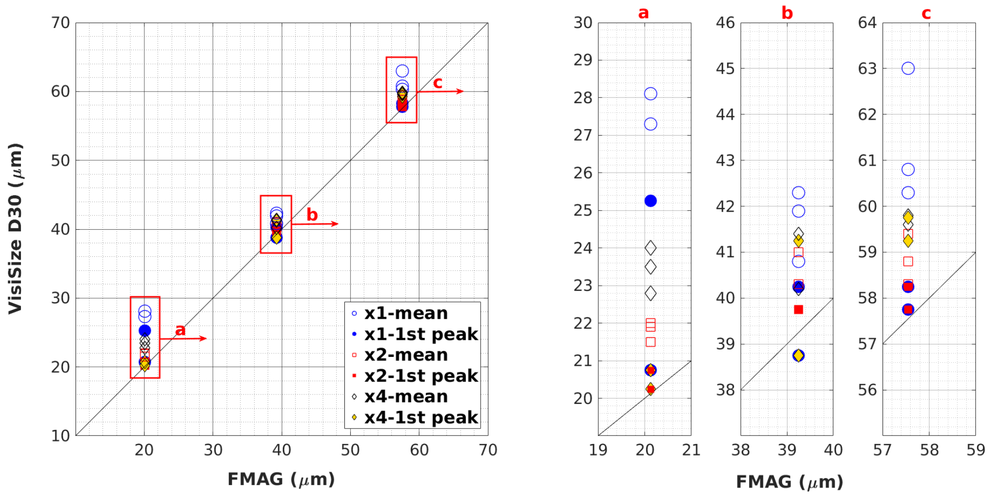

Figure 3.6: Comparison of droplet sizing between VisiSize D30 and FMAG: scatter plot illustrating the position of the first peak in size histogram and arithmetic mean diameter with respect to FMAG generated droplet sizes for different lens magnification settings (left). Red boxes (a, b, c) are enlarged in panels on the right. Each pair of points (filled and empty) represents a single measurement.

Finally, the accuracy of sizing is evaluated more quantitatively in a scatter plot in Fig. 3.6 which compares the initial droplet size as specified on FMAG with the results obtained with the VisiSize, mean droplet diameter reported by the software and the position of the first significant peak in the size histogram. Obviously, the mean diameter is larger than the first peak as it includes the contribution of collided droplets.

Excluding the problematic case of magnification ×1 for size 20.13 µm, the position of the first peak deviates up to 2.0 µm from the original value and the relative error ranges up to roughly 5%. However, with regard to the accuracy of the VisiSize shadowgraph instrument, it is only an estimation of the upper bound for those quantities, as the generated size is also subject to intrinsic uncertainty. Hence, as far as the comparison with FMAG allows, the sizing by the VisiSize is indeed pretty accurate, apart from small droplets observed with magnification $\times 1$, for which uniform illumination of the scene proved difficult (Sect. 3.5 from Nowak et al., 2021)

Interestingly, the first peak estimation is mostly higher than the FMAG one while the opposite can be expected due to evaporation effects. This suggests that the VisiSize slightly overestimates the sizes with respect to the FMAG-generated droplet sizes in most cases.

3.3 Summary

A series of laboratory tests with the VisiSize were conducted using a monodisperse droplet generator, FMAG 1520. It was aimed to characterize the performance of VisiSize in terms of particle sizing which influences the relevant statistics of cloud droplets, such as the droplet mean diameter and size distribution. Substantial effects of droplet collisions and evaporation were observed in the size histograms obtained with the VisiSize. However, after filtering out collisions by selecting the first major peak, the results indicated reasonable agreement between the diameters reported by the VisiSize and those assumed to be generated by the FMAG. The difference was no larger than 2µm or 5%, except for the measurements with the lens magnification setting $\times 1$, for which uniform illumination of the scene was proved to be difficult.

4 Field measurements of cloud droplets

This chapter is dedicated to simultaneous in situ measurements of cloud droplets with the VisiSize and PDI probe at the Schneefernerhaus environmental station (UFS). First, a brief introduction to the measurement campaign is provided. Then, the results from the two instruments are compared to each other for different microphysical properties, such as droplet size distributions, mean droplet sizes and velocities, the DNC, and the LWC. The measurements were mainly performed by me with the help of colleagues from IGF-UW and MPI-DS institutes, while I analyzed the results which are already published in (Mohammadi et al., 2022a).

4.1 Zugspitze measurement campaign

As mentioned in Sect. 1.2, the UFS research station, which is located just below the peak of Zugspitze, is a suitable location for in situ cloud measurements. On the other hand, the configuration of the VisiSize setup (see Figs. 2.1 & 3.1) makes it difficult to perform any airborne measurement with the device. Considering this condition, we decided to conduct the first field experiment with the VisiSize at the UFS.

The UFS consists of 12 floors constructed into the southern flank of the

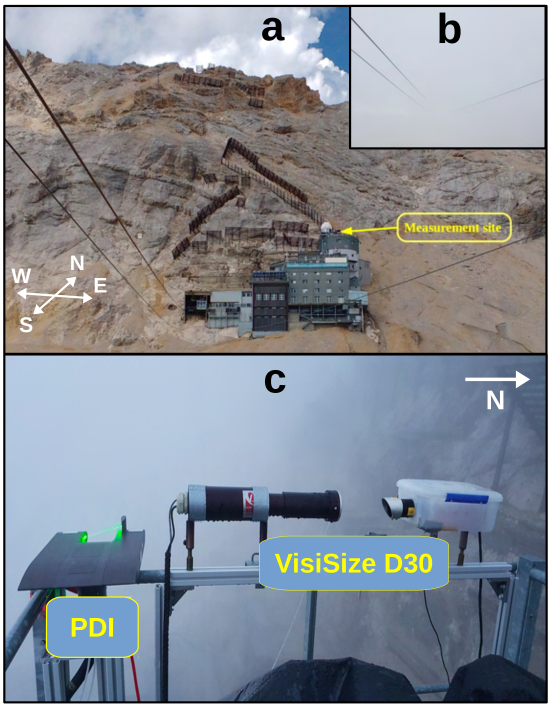

Figure 4.1: Cloud field experiment at the Schneefernerhaus: (a) View of the UFS from Zugspitzplatt on a sunny day, pointing out the measurement site on the 9th-floor rooftop; (b) The same view while the UFS is immersed in clouds; (c) Main instruments: the VisiSize, and the PDI probe mounted next to each other, while clouds are approaching the UFS from the west side.

Zugspitze and frequently is immersed in clouds as shown in Fig. 4.1. In west of the UFS, there is a wind hole on Schneefernerkopf mountain ridge (see Fig. 1.13-c) which directs the westerly wind over the UFS. Hence, the main parts of the VisiSize (the laser head and camera) were mounted on an aluminum stand alongside the PDI probe as they both faced the wind hole to the west as shown in Figs. 4.1-c & 4.2. The whole setup was placed on a steel platform, located on the western side of the 9th-floor rooftop.

Measurements took place during a three-week long campaign in July-August 2019. Over the campaign period, there were nine days of successful

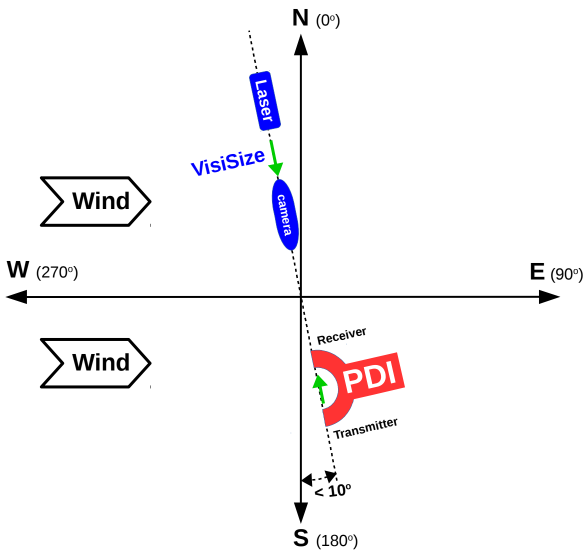

Figure 4.2: The schematic representation of the experimental setup orientation during the Zugspitze measurement campaign at the UFS. This configuration allows to optimally measure the clouds coming with the wind from the "wind hole" located on the Schneefernerkopf in west of the UFS.

measurements of cloud events, with both instruments often running simultaneously. The measurements were run consecutively with 15 minutes running time. Therefore, the data were recorded for each 15-min long segment of measurements separately. Hereafter each of these segments is called a measurement case. Sometimes during the experiment, either one of the instruments did not function properly. Therefore, in order to make a comparison later, I excluded all those cases from the analysis. Consequently, 133 cases were selected in which data from both instruments were available over the entire measurement case period.

The selected cases include measurements with the lens magnifications ×2 and ×4 for the VisiSize, in live diameter or velocity mode. Based on the results of laboratory experiments with the VisiSize (explained in Chapter 3 and Appendix A), it was decided not to use lens magnification ×1 for cloud droplet measurements. As listed in Table 4.1, most of the selected cases are conducted with the VisiSize ×2 lens magnification in diameter mode. Thanks to the larger sample volume when using this magnification, we could collect as many cloud droplets as possible during each measurement case. Nonetheless, using magnification ×2 in diameter mode caused lack of velocity information, and sometimes missing the smallest droplets ($D < 6$ µm) in those measurements.

Table 4.1: Statistics of the VisiSize measurements at the UFS during 2019 campaign listing the number of selected measurement cases for different modes and lens magnification settings.

Selected measurements		133	
Lens setting		×2	×4
VisiSize mode	Diameter	84	26
	Velocity	18	5

The PDI probe also measured cloud droplets simultaneously for all selected cases. However, PDI channel 1 did not work properly during the campaign. It could not collect enough large samples in any of the selected cases (details are explained in Appendix C). Hence, to compare the instruments, I only used the data collected with PDI channel 2 with an adjustment to the sizing range according to the instrument manual.

The sizing filter was applied to both instruments so that they could record droplets from the minimum of their detection range (e.g. 1 µm for PDI channel 2, and 2 µm for VisiSize mag. ×4) up to 80 µm in diameter. The upper size limit helped to avoid mistakenly recording raindrops during the measurements. Moreover, the typical range of droplet counts during the measure-

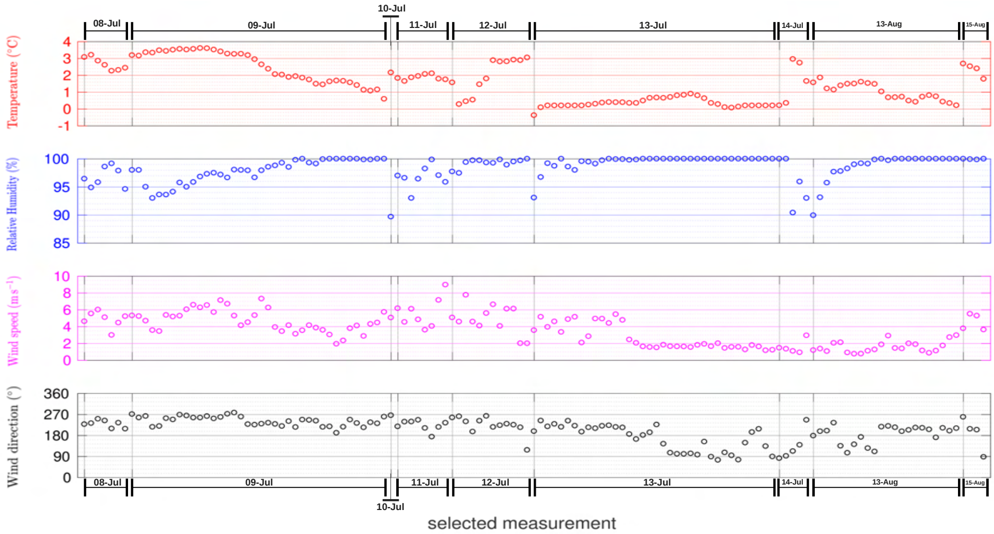

Figure 4.3: Local weather conditions at the UFS, obtained from recordings by German Weather Service (Deutscher Wetterdienst, DWD) during the measurement campaign including temperature, relative humidity, wind speed and wind direction. Each single point in the plots represents a mean of DWD data collected during a selected measurement case (over a 15 minute interval). The selected cases in each day are shown in chronological order from left to right, however, all two adjacent points do not necessarily represent two consecutive measurements. Wind direction is measured relative to the northerly orientation, with easterly, southerly, and westerly winds being assigned 90°, 180°, and 270° angle respectively.

ments was between 560–10463 with the VisiSize and between 6330 – 118330 with the PDI. Subsequently, the Poisson sampling uncertainties for the average (arithmetic mean) count with the VisiSize and the PDI are estimated to be $\sim 1.3\%$ and $\sim 0.4\%$, respectively.

Figure 4.3 shows the local weather conditions at the UFS during the measurements, obtained from recordings by the German Weather Service (DWD). Each individual point on these diagrams represents a mean of DWD data measured with 1-minute time resolution during a selected case (over a 15-minute interval). The average temperature during the measurements typically changed between 0 and 4°C and relative humidity usually varied between 95 and 100%. Wind speed was more variable ranging from ∼1 to over 8 $\mathrm{m\,s^{-1}}$, mostly coming from the southwest direction (between 180 and 270°).

The orientation of instruments allowed for ideal measurements of clouds coming from the west. However, as shown in Fig. 4.3, about 20% of the measurement cases were performed during easterly wind events (below 180°). Analyzing data revealed that the wind direction effects on the results were negligible. Consequently, no cases with respect to their wind direction were excluded from the data analysis presented in the next section. The seasonal meteorological conditions as well as cloud and turbulence properties at the UFS have been already available in detail by Siebert et al. (2015) and Risius et al. (2015) and briefly described in Sect. 1.2.

4.2 Results and discussion

The result of data analysis of Zugspitse campaign is provided in this section. First, a sample measurement with the VisiSize and the PDI probe is investigated. The functionality of both instruments can be compared according to the size range of detected droplets in the sample measurement. Then, the effectiveness of modifications and various additional filters (defined in Appendices A & B) at reducing the discrepancy between the two instruments' outputs are analysed.

The outputs include "raw data" of detected droplets' size and velocity as well as the result of live internal data processing by the instrument software during each measurement (e.g. arithmetic means, DNC, and LWC).

Moreover, what is obtained after applying the modifications and filters to the raw data is called "modified data". To distinguish between different data processing methods, I use the terms: default (def.) or corrected (cor.) sample volume for the VisiSize, and original (org.) or modified (mod.) DNC methods for the PDI probe (see Appendices A & B for detailed definitions).

4.2.1 Sample measurement case

Table 4.2 demonstrates the instruments' outputs regarding a measurement conducted on 13th of July 2019 between 15:36 and 15:51. According to the DWD data (shown in Fig. 4.3) during this cloud event, the wind was blowing with the average speed of ∼4.5 $\mathrm{m\,s^{-1}}$ from southwest (average direction of ∼225°), while the average temperature and relative humidity were ∼0.4°C and 100% respectively.

The camera lens magnification ×2 was used for the VisiSize during this measurement. Different mean diameter values compared in Table 4.2 are arithmetic mean ($\bar{D}$), surface mean (D_2) and volume mean (D_3) which are calculated as follows:

$$\bar{D} = \sum_k \frac{D_k}{n} \ , \tag{4.1}$$

$$D_2 = [\sum_k \frac{{D_k}^2}{n}]^{1/2} \ , \tag{4.2}$$

$$D_3 = [\sum_k \frac{{D_k}^3}{n}]^{1/3} \ , \tag{4.3}$$

where D_k refers to the diameter of *k-th* measured droplet, and n is the total count.

Table 4.2: Comparison between the cloud droplet measurement data from the VisiSize and PDI probe collected on 13th July 2019 15:36' - 15:51'.

Instrument	**VisiSize (×2 lens mag.)**	**PDI**	
$\bar{D}$ [µm]	10.23	13.08	
D_2 [µm]	10.45	13.26	
D_3 [µm]	10.67	13.46	
Method	-	**transit time**	**swept volume**
DNC [cm^{-3}]	348	185	350
LWC [$g\ m^{-3}$]	0.22	0.23	0.44

Comparing the mean diameter values, a $\sim 3\,\mu m$ difference between the results of the two instruments can be observed in this measurement. The PDI calculates the DNC and the LWC from two different methods (explained in Sect. 2.2.1) which both were listed in Table 4.2. The DNC value reported by the VisiSize corresponded very well with the one obtained from the PDI using the swept volume method. On the other hand, the swept volume method led to the LWC value from the PDI being twice as high as one from the VisiSize, while they did agree when using the transit time method.

Figure 4.4-a shows the normalized DSD histogram of the aforementioned measurement for both instruments together with the arithmetic mean diameters displayed in the corresponding legends. The histogram was plotted using the probability density function (PDF). Consequently, it allowed for a comparison of sizing properties between the VisiSize and the PDI, while the effects of their different sample volume estimations were excluded. Besides the apparent small µm shift in distribution, the lack of droplets with diameter below $D_{\rm min}$ due to the PVC factor is also clearly visible (see Sect. 2.2.1 & Appendix B.3 for definitions).

In Fig. 4.4-b, droplets smaller than 9 m, equal to the PDI fit value ($D_{\rm min}$)

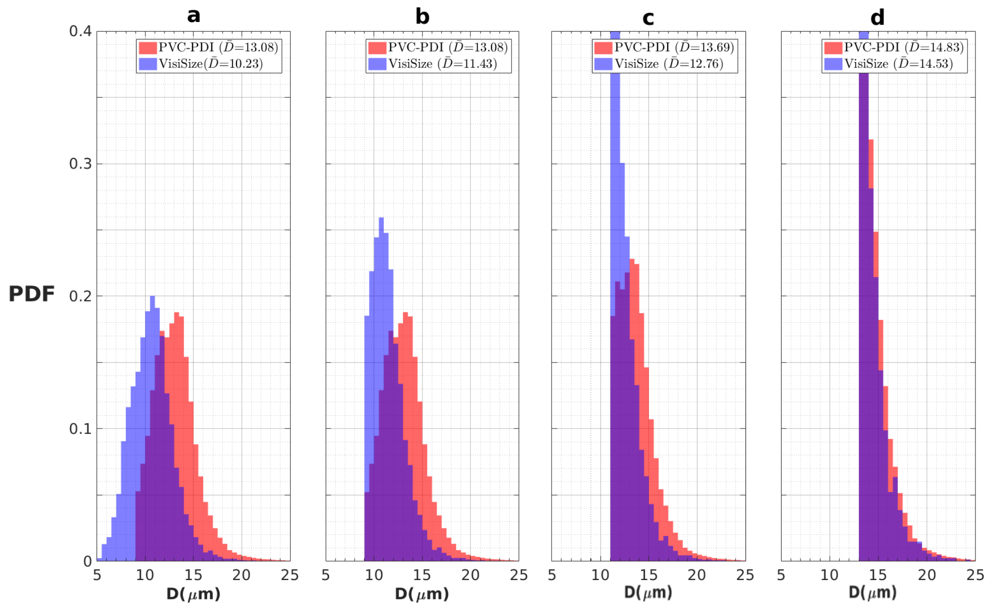

Figure 4.4: Probability distributions of cloud droplet sizes for data collected with the VisiSize and the PDI probe during measurement on 13th July 2019, 15:36' – 15:51'. The distributions have been truncated at progressively large values of droplet diameter for each plot: $(a)D > 0\,\mu\text{m}, (b)D > 9\,\mu\text{m}, (c)D > 11\,\mu\text{m}, (d)D > 13\,\mu\text{m}$. The resulting arithmetic mean diameters for each instrument are shown in the legend.

for this measurement, are filtered out for both instruments which resulted in reducing the $\bar{D}$ difference. By increasing the minimum cutoff values in the subsequent plots, the DSD histograms, as well as $\bar{D}$ ultimately reach a good agreement for droplet sizes larger than 13 µm in Fig. 4.4-d. Hence, it seems valid to conclude that the PDI is not as sensitive as the VisiSize when it comes to the droplets with diameters below 13 µm.

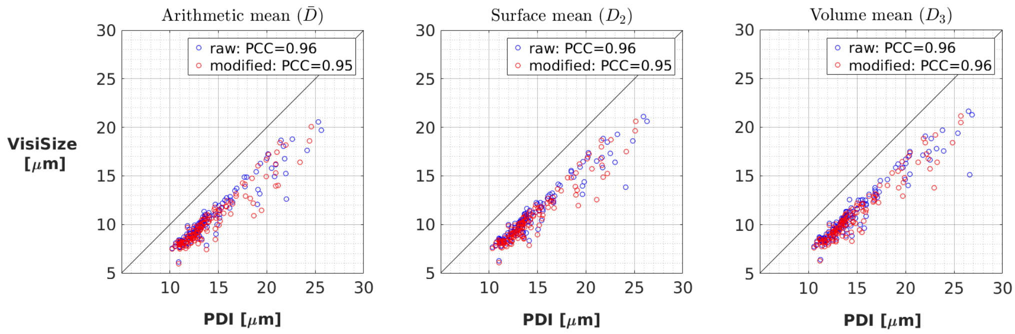

Figure 4.5: Comparison of cloud droplet mean diameter between the VisiSize and the PDI probe. Scatter plots of arithmetic mean ($\bar{D}$), surface mean (D_2) and volume mean (D_3) are shown from left to right respectively. Each pair of blue/red circles indicates raw/modified data for a selected measurement of ∼15 min long. Pearson correlation coefficients (PCC) also shown in the legend as an index of linear correlation.

4.2.2 Sizing and Velocimetry

Next, the two instruments are compared based on the mean diameter and velocity of cloud droplets measured over the whole campaign period including all selected measurement cases. The arithmetic, surface and volume means of droplets measured with the VisiSize and the PDI are shown in Fig. 4.5 from left to right respectively. Each blue circle represents a comparison between the mean diameters obtained from the VisiSize and the PDI based on the raw data of a selected measurement case, while the corresponding red circle for that measurement is obtained after applying a modification to the raw data. For the VisiSize, the sample volume (SV) was modified, while the coincidence filter was applied to the PDI raw data as a modification.

The Pearson correlation coefficient (PCC) for each scatter plot is also shown in the legend. The PCC is a normalized version of covariance showing the strength of linear relation between the two instruments here. It ranges from the perfect negative linear correlation (equal to -1) to the perfect positive linear correlation (equal to 1). Scatter plots for different types of mean diameter in Fig. 4.5 seem very similar to each other with the PCC very close to 1 showing a strong correlation. Mean diameters from the PDI are consistently between 3 and 6 µm higher than the VisiSize. Applying modifications to the data shows no visible effect on the mean diameters. However, it is expected that it would be more influential on the DNC, which is going to be investigated later in this section.

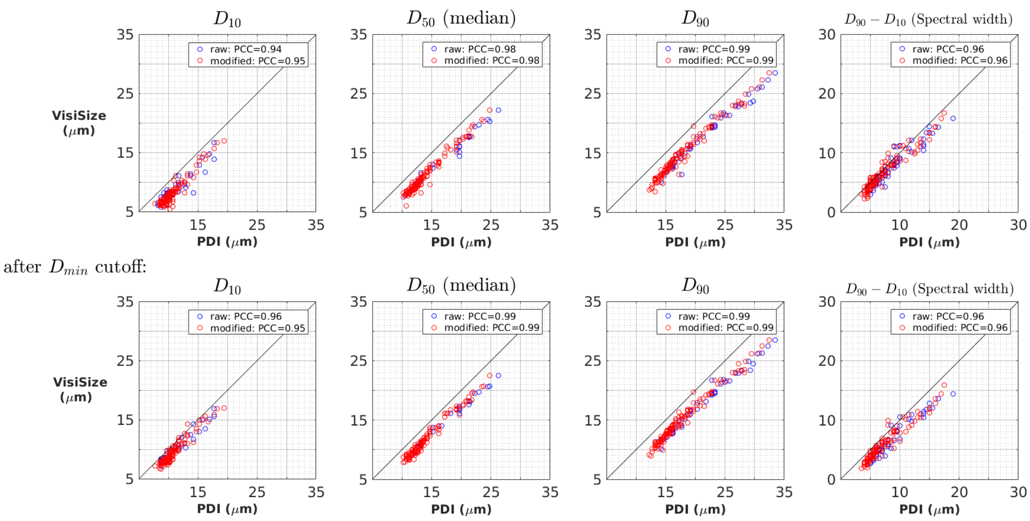

Figure 4.6: Comparison between the VisiSize and the PDI probe regarding the diameter size percentiles (D_{10}, D_{50}, and D_{90}) as well as spectral width ($D_{90} - D_{10}$) of cloud droplets. Each pair of blue/red circles indicates raw/modified data for a selected measurement of ~15 min long. Pearson correlation coefficients (PCC) also shown in the legend. The second row shows each plot after applying the D_{min} cutoff to the data.

Since in Fig. 4.4 it was already shown that the two instruments behave differently for small droplets, comparing only the diameter mean values may not be enough for this study. Therefore, in Fig. 4.6, I investigated the other size metrics for collected data on cloud droplet diameters, including the 10th percentile (D_{10}), the 50th percentile ($D_{50} \equiv$ median), and the 90th percentile (D_{90}). Moreover, the spectral width, defined as the subtraction of D_{10} from D_{90}, showing distribution breadth in each measurement case is also compared between the two devices in Fig. 4.6.

Just as in Fig. 4.5, here blue and red circles also represent raw and modified data respectively, accompanied by the PCC in the legend. In addition, a second row is added in order to demonstrate the results after applying the D_{min} cutoff on data by filtering out all droplets smaller than D_{min}, fit value for PDI data, from the analysis (same as Fig. 4.4-b).

For majority of measurement cases, the percentiles values are again higher for the PDI than the VisiSize just as for mean diameter plots, while in a few cases they are very close or even on the 1:1 line. The PCCs are also generally close to 1 with the highest linear correlation observed for the largest droplets (90th percentile). When it comes to the spectral width, the number of cases very close to or even above 1:1 line, meaning larger value for the VisiSize than the PDI, is higher than in plots for diameter percentiles. However, the difference between raw and modified data is still negligible.

By applying the D_{min} cutoff, it can be seen that scatter plots slightly shift up, especially for the smallest droplets (10th percentile). It can be a consequence of removing the tiny droplets, which were identified only by the VisiSize, from the analysis. This also affects the spectral width plot and shifts it down a bit. Overestimating droplet sizes by the PDI in comparison with the VisiSize, as illustrated in Figs. 4.5 & 4.6, was also observed in the past by Chuang et al. (2008) where the PDI was compared to the FSSP-100.

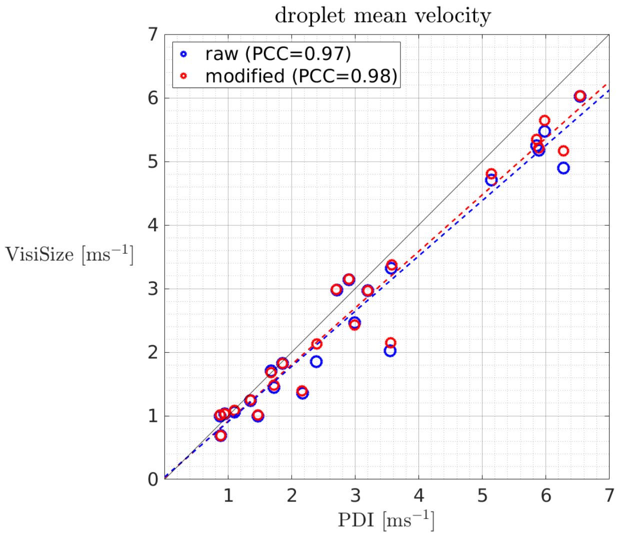

Figure 4.7: Comparing the droplet mean velocity between the VisiSize and the PDI probe. Each pair of blue/red circles indicates raw/modified data for a selected measurement of ∼15 min. The least squares regression (LSR) lines are displayed with dash, and the Pearson correlation coefficient (PCC) are shown in the legend.

In Fig. 4.7, cloud droplet mean velocity obtained from the two instruments has been compared. As is shown in Table 4.1, there are only 23 selected measurements with the VisiSize in the velocity mode where it was able to measure size and velocity simultaneously. The reason why the VisiSize was mainly used in the diameter mode is due to the fact that droplet detection rate drops significantly in the velocity mode, since a single droplet has to be identified twice to be counted. In other words, the device must find an already detected droplet again in the next or same frame depending on the selected method (explained in Sect. 2.1.3). Then, it can measure its velocity based on the position shift between the two shadow images. Therefore, the velocity mode was only used in case of dense clouds, when despite having such limit, sufficient data for further analysis still could be collected.

A reasonable correspondence between the mean velocities obtained from the two devices is observed in Fig. 4.7, especially for smaller velocities. A strong linear correlation between the results also exists according to the PCC values. However, no significant change is observed after applying the modification to the data.

Two additional dash lines were also plotted corresponding to each set of data which are “Least Squares Regression” (LSR) lines. The LSR is a line that makes the vertical distance from the data points to the regression line as small as possible. Hence, the closer LSR line to the 1:1 line would be, the better agreement between the instruments is expected.

Considering the mean velocity as the values increase, one can see a slight change in the trend. The PDI recorded higher mean velocities than the VisiSize for all cases above $5\,\mathrm{m\,s^{-1}}$. A possible explanation could be that in high-speed flows, some droplets, which pass the sample volume very fast, can be missed by the VisiSize in the second frame. This occurs due to the limit of the camera speed (maximum of 30 fps). Hence, the average velocity calculated by the VisiSize would be slightly underestimated in high-speed flows in comparison with the PDI, which does not experience such a problem.

4.2.3 DNC

Fig. 4.8 demonstrates the comparison between the VisiSize and the PDI probe based on the DNC of cloud droplets. To be able to better present and interpret the data, a logarithmic scale has been used in this figure as well as the rest of figures in the current chapter.

The first scatter plot on the top - left shows the raw data processed by the instruments, where blue and red circles represent the PDI transit time and swept volume methods, respectively. The LSR dash lines and PCC values are also included in the plots. Next, in the top - middle and top - right, the results after applying sample volume (SV) modification and coincidence filter (for PDI data) are shown. Corresponding plots after applying the D_{min} cutoff are shown in the second row.

The DNC plots are more scattered and demonstrate less linear correlation between the two instrument results than the mean diameter and velocity plots (Figs. 4.5 - 4.7). Hence, for better comparison between the instruments and methods as well as investigating the effects of applied modifications and filters, following the changes in the LSR lines and the PCC values are required.

As mentioned earlier, the VisiSize can fail in detection of the fastest droplets in velocity mode, resulting in an underestimation of the DNC, especially in cloud events with high-velocity flows. Thus, for the DNC (and later the LWC) comparison, only the measurement cases in which the VisiSize was working in diameter mode have been analyzed.

The first plot in Fig. 4.8 (top - left) shows a noticeable discrepancy between the transit time and the swept volume methods. The DNC values from the transit time method of the PDI are usually smaller than the VisiSize raw data. However, with swept volume method there are more cases with higher DNC for the PDI than the VisiSize. Subsequently, after applying the SV correction on the VisiSize data as well as modification of PDI swept volume method in the next plot (top - middle), the DNC values generally increase.

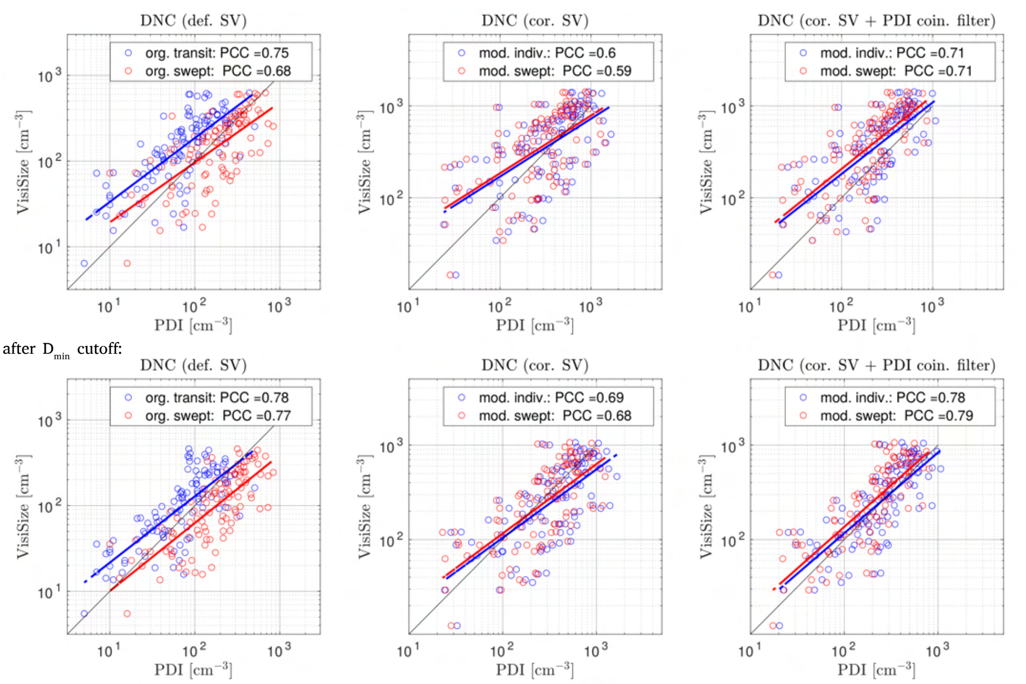

Figure 4.8: Comparison of the DNC results between the VisiSize and the PDI probe. From top - left to top - right, the plots respectively show the raw data, the data after modification, and the modified data after applying the coincidence filter to the PDI results. The scatter plots after applying the D_{min} cutoff are shown in the second row. Each PDI method for the DNC computation is shown with a different color within the plots (each pair of blue/red circles: a selected measurement of ∼15 min long). The least squares regression (LSR) lines are displayed with dashed lines blue/red, and the Pearson correlation coefficient (PCC) are shown in the legend.

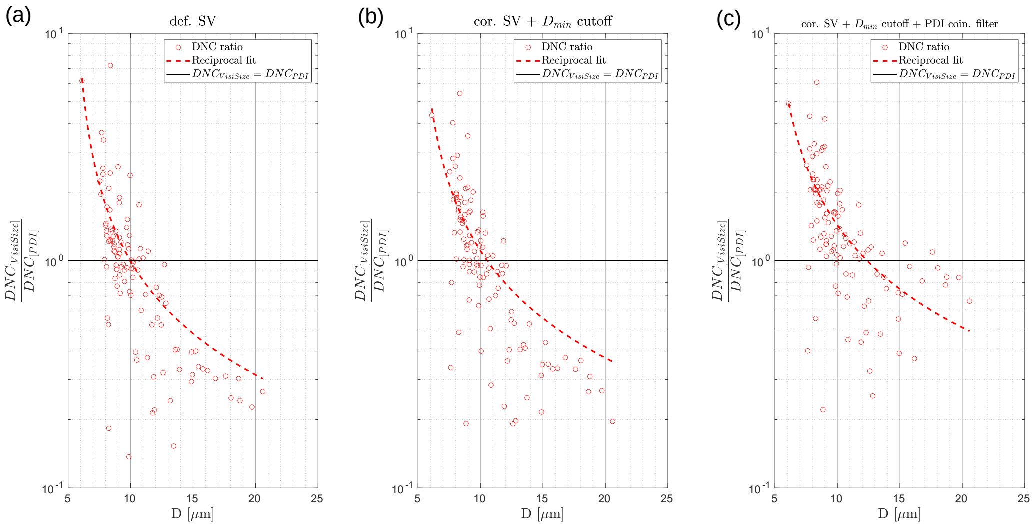

Figure 4.9: The DNC ratio of the VisiSize to the PVC-PDI as a function of arithmetic mean diameter size. Panels (a-c) show the raw data (using the default SV for the VisiSize), the results after the SV correction and the D_{min} cutoff, and the results after additionally applying the coincidence filter to the PDI data. Each circle represents a single measurement of ∼15 min. The reciprocal fit curves $(y = \frac{a}{x+b})$ and the 1:1 ratio are shown with the dashed and horizontal black lines, respectively.

Nevertheless, in most cases, especially in dense cloud events (with high DNCs), the VisiSize provides higher values than the PDI. The results' shift towards the VisiSize continues after applying the coincidence filter on the PDI. Finally, after omitting the small droplets by means of D_{min} cutoff, the LSR lines tend towards the 1:1 line, especially for the individual method of the PDI, with a slight growth in the PCC values to their highest level. This behavior after applying D_{min} cutoff agrees well with what has been observed already in Fig. 4.4.

In Fig. 4.8, it is observed that after excluding the smallest droplets, the correspondence between two instruments regarding the DNC results improved. Therefore, it is important to investigate the instruments responses to droplet size change in more detail when it comes to the DNC computation. For this purpose, the DNC ratios of the VisiSize to the “PVC-PDI” as a function of arithmetic mean diameter size are plotted in Fig. 4.9.

On the left panel, the raw data from the instruments are compared. The swept volume method from the PDI with consideration of the PVC factor is used and called PVC-PDI. Just as in previous plots, here also each circle represents a single selected measurement while a reciprocal fit curve ($y = \frac{a}{x+b}$) is also plotted to better illustrate the trend as the arithmetic mean diameter increases.

The droplet mean size for each measurement is taken from the VisiSize raw data. The 1:1 ratio lines where the DNC results from the two instruments are equal also shown within the plots. Plots after applying modifications and filters on data are shown in next panels in the middle and right side of Fig. 4.9.

For the smallest sizes the ratio is higher than 1, which means raw values from the VisiSize are actually couple of times larger than the PDI. However, as the mean size increases, there is a dramatic fall and for diameter means $\sim$10 µm there are many cases close to 1:1 line. As the mean size rises, the ratio decreases more and for $\bar{D}$ >13 µm reaches even below 0.5. Nevertheless, we observe gradual changes after applying the modifications, D_{min} cutoff, and finally coincidence filter which makes the DNCs show better correspondence, especially for larger droplets.

The effect of using different camera lens magnification settings of the VisiSize on the DNC results is investigated in Fig. 4.10. The last plot from Fig. 4.8, where the results were shown after applying all modifications and filters on data, is replotted here for measurement cases with each VisiSize lens

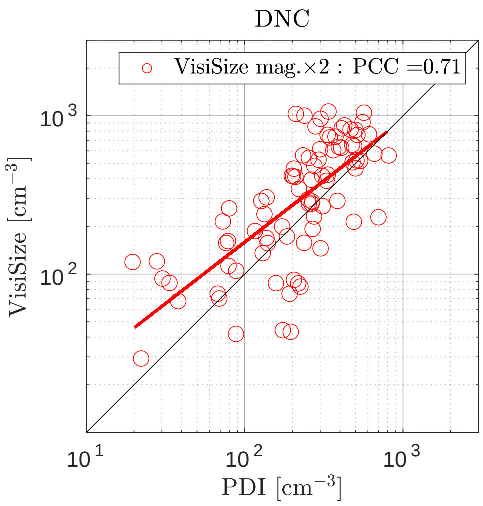

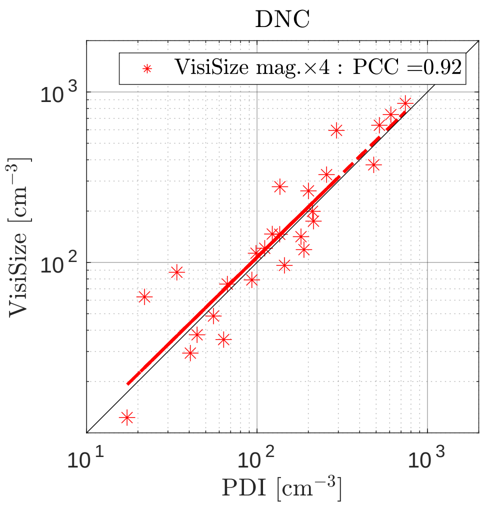

Figure 4.10: The DNC comparison between the two instruments, with cases using different lens magnification settings for the VisiSize (×2 and ×4) are plotted separately. The results after applying all modifications and filters to the data and application of PVC factor on PDI swept volume method are used here. Each circle/star represents a single measurement of ∼15 min. Dashed red lines show the LSR, and the PCC is shown in the legend.

magnification separately. In the top panel, the PVC-PDI results from the swept volume method are compared with the VisiSize results with the magnification ×2. The comparison of the measurements with the magnification ×4 are shown in the bottom panel.

In the case of using magnification ×2, the results are still generally scattered, with mostly higher DNC values from the VisiSize than from the PDI. Nonetheless, the results of using magnification ×4 interestingly show better agreement with the PDI data. The PCC value is close to 1, indicating high correlation between the two instruments, and the LSR line is almost coincident with the 1:1 ratio line in this case. However, the number of cases measured with ×4 magnification is approximately 3 times lower than those measured with ×2 magnification (see Table 4.1).

As mentioned earlier, for higher lens magnifications of VisiSize, despite the rise in sizing accuracy, the sample volume (SV) reduces significantly. Therefore, it is sometimes difficult to collect large enough sample during the course of measurements, especially for larger droplets. Thus, I often used the magnification ×2 to collect sufficient data in each measurement, while the usage of ×4 was limited mostly to the events with smaller cloud droplets.

In Fig. 4.11, the DNC results from the VisiSize and the PDI probe are again shown after applying all modifications and filters. The arithmetic mean diameter ($\bar{D}$) and the velocity standard deviation (σ_v) within the measurement cases are also illustrated by adding a colour map next to the scatter plot.

As in Fig. 4.9, for smaller droplets here, the DNCs from the VisiSize are higher than from the PDI, while with a rise in $\bar{D}$, they correspond better.

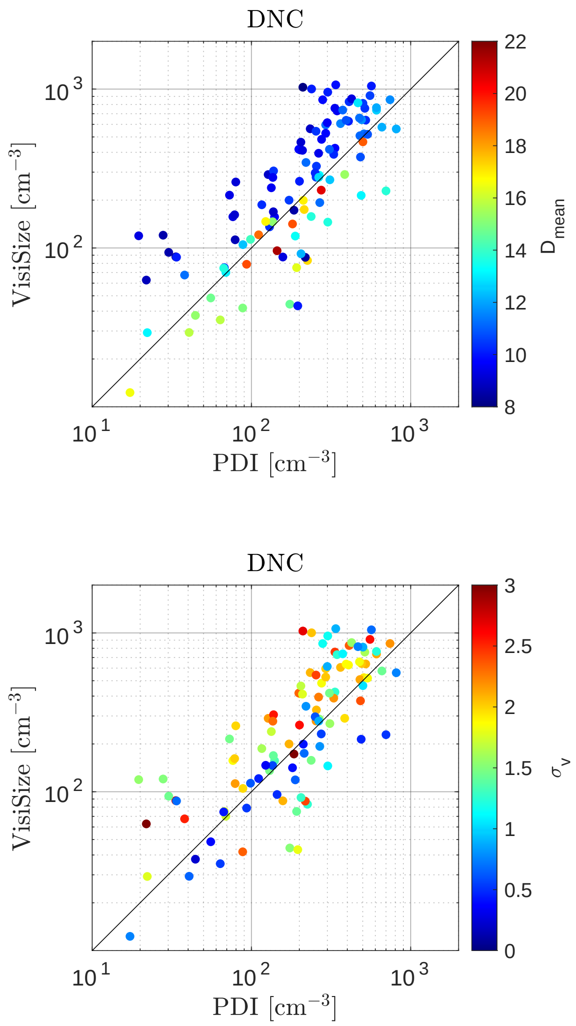

Figure 4.11: The DNC comparison between the two instruments, with the mean diameter spectra (top panel) and the standard deviation of velocity spectra (bottom panel) compared between the selected cases. The results after applying all modifications and filters to the data and with application of the PVC factor to the modified PDI swept volume method are used here. The mean diameters and the velocity standard deviations are calculated using the VisiSize and PDI data, respectively. Each circle represents a single measurement of ∼15 min.

This is also in agreement with the Chuang et al. (2008) observation where the PDI reported lower DNC than the FSSP-100 device, especially for smaller size ranges.

On the other hand, the DNC response with respect to the changes in velocity seems not to follow the same trend. The DNCs in cases with the lowest σ_v mostly agree better. This was expected since the PDI requires averaging droplet velocity over the size and time bins to compute the DNC, which can be a source of inaccuracy (see Eqs. 2.10 & 2.11). However, there are also cases with a low σ_v, where the results do not correspond well. Hence, it is difficult to draw a solid conclusion regarding the effect of σ_v on the DNC response.

As mentioned earlier, during the course of the measurements wind was blowing mostly from southwest with an average direction of $\sim 225°$, and an average speed of $\sim 4.5\ \mathrm{m\,s^{-1}}$. However, some cases of easterly wind with direction $\sim 90°$ and rather low speed ($< 2\ \mathrm{m\,s^{-1}}$) were also observed (see Fig. 4.3). In general, it was not expected that the easterly wind would affect sizing or velocimetry measurements with the VisiSize since its laser head and camera housing are off - axis. However, the velocities measured with the PDI could be slightly affected in case of easterly winds due to the probe's shape.

The effect of wind direction on measurements with the VisiSize and the PDI is investigated in Fig. 4.12. The DNC results are compared between the two instruments after applying the coincidence filter to the PDI results as well as $D_{\min}$ cutoff on both instruments (same as the last panel in Fig. 4.8). While on the right panel the cases with Easterly wind were excluded from the analysis, the changes in the result seem to be negligible. Comparing the

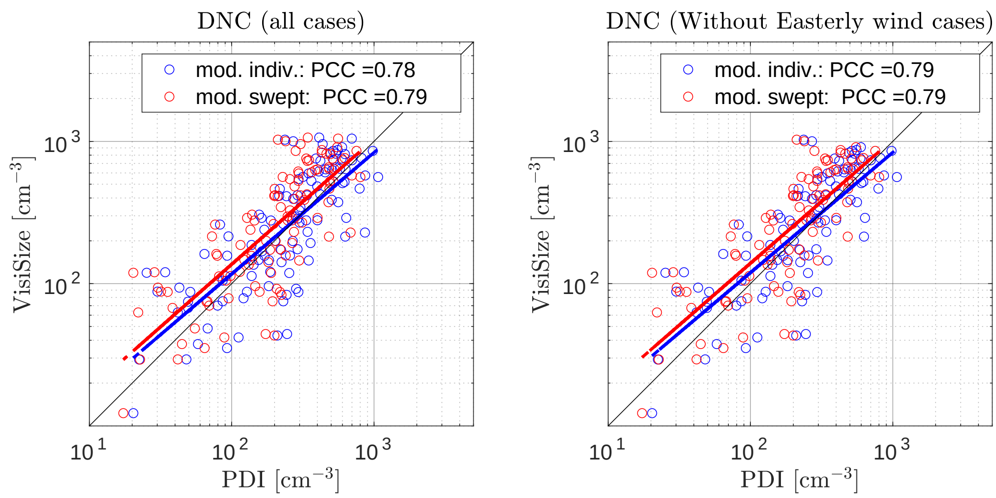

Figure 4.12: Comparison of the DNC results between the VisiSize and the PDI probe with and without data collected during easterly wind events. The modified data after applying the coincidence filter to the PDI results as well as D_{min} cutoff on both instruments are shown here.

PCC values and LSR lines slopes between the two plots show almost the same results.

It must be noted that those cases with the easterly wind did not occur often ($\sim$ 20% of all cases), and most had quite low speed (< 2 m s^{-1}) which could explain why their exclusion from the analyses did not change the final results. When the wind speed is low, the wake area behind the body of the PDI is expected to be relatively small. Hence, the instrument's sample volume is rather weakly affected by the wake area. The observation of weaker easterly winds compared to westerly winds has been also mentioned by Risius et al. (2015) (see Fig. 1.14).

4.2.4 LWC

In Fig. 4.13, the same scatter plots pattern as in Fig. 4.8 is employed to demonstrate the LWC comparison between the two instruments. Although both PDI methods report the LWC higher than the VisiSize, the discrepancy between the swept volume and the VisiSize is greater. The SV modification alone does not help with reducing this discrepancy, yet it increases the figures. However, after applying coincidence filter, the LSR line slope increases and it moves slightly toward 1:1 reference line.

Applying the D_{min} cutoff also a little increases the correlation between the two instrument results. Nonetheless, the LWC values from the PDI are still larger than from the VisiSize and in some cases unreasonably high. The typical reported LWC at the UFS (Siebert et al., 2015) and in another part of the Alps (Spiegel et al., 2012), measured by a PMV-100A, was below $1\,\mathrm{g\,m^{3}}$, which suggests an occasional overestimation of the LWC by the PDI.

Explaining why discrepancies in the LWC are generally larger than in the DNC, while applied filters are less effective in reducing them, requires considering the main variables related to the LWC. Mass of the water droplets is one of these variables which can be replaced by the droplet diameter size, assuming constant water density and spherical droplet shape. The other key component of LWC computation is the DNC itself. Therefore, the changes in the LWC are directly related to the DNC as well as the volume mean diameter (D_3).

In other words, the discrepancies in both DNC and droplet mean size facilitate a greater resultant discrepancy in the LWC. However, it is crucial to bear in mind that while the LWC changes linearly with the DNC, it

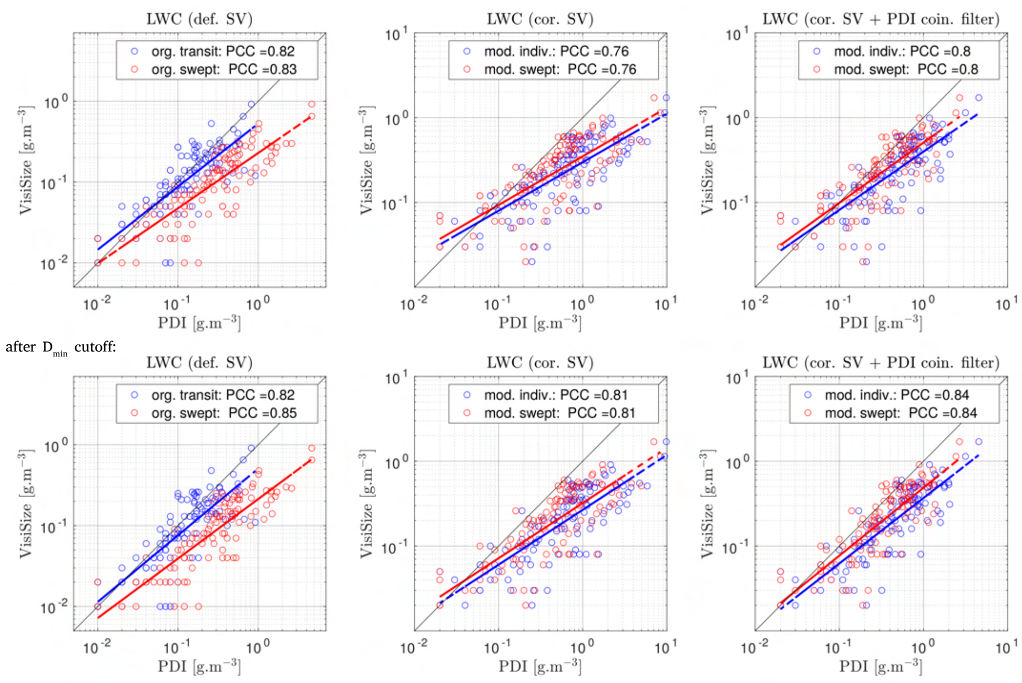

Figure 4.13: Comparison of the LWC results between the VisiSize and the PDI probe. From top - left to top - right, the plots show the raw data (based on the default sample volume for the VisiSize and the original DNC methods for the PDI), the data after modification, and the modified data after applying the coincidence filter to the PDI results. The scatter plots after applying the D_{min} cutoff are shown in the second row. Each PDI method for the LWC computation is shown with a different color within the plots (each pair of blue and red circles: a selected measurement of ∼15 min). Dashed blue/red lines show the LSR, and the PCCs are displayed in the legend.

increases cubically with a rise in mean diameter size (LWC $\propto$ DNC $\cdot$ ${D_3}^3$). Consequently, smaller droplets play less important role in the LWC estimates than the larger ones. Then, excluding the smaller droplets by applying D_{min} cutoff would also be less effective on the LWC than the DNC.

Moreover, as illustrated in Figs. 4.5 & 4.9, the PDI does not only report larger mean diameters than the VisiSize, but it also shows higher DNC values in cases with large mean diameters. Subsequently, these observations can account for some unreasonably high LWC values obtained from the PDI data given the above relationship between the LWC, DNC, and D_3.

In Fig. 4.14, the LWC from the two instruments is compared for different VisiSize lens magnifications, as shown in Fig. 4.10. There is no significant difference between the magnifications regarding the LWC results, and in both, the LWC leans toward the PDI as in Fig. 4.13. Subsequently, the comparison between the LWC from the two instruments is shown in Fig. 4.15, while the changes in the mean diameter value, as well as the velocity standard deviation, are also illustrated with the colour maps next to the plots. As is shown in the top panel, the two instruments show better agreement for smaller droplet mean values, while for larger droplets the discrepancy is higher. As mentioned earlier, it seems that the PDI overestimates the LWC in the event of clouds with large mean droplet sizes.

Although the trend here is opposite to what was observed for the DNC, it is still explicable as we consider the cubical relation between the LWC and the droplet mean size. Thus, the LWC discrepancy arises as the mean diameter size grows. On the other hand, for small droplets, the lower discrepancy in mean size, where the PDI shows larger values (shown in Figs. 4.5 & 4.6), is

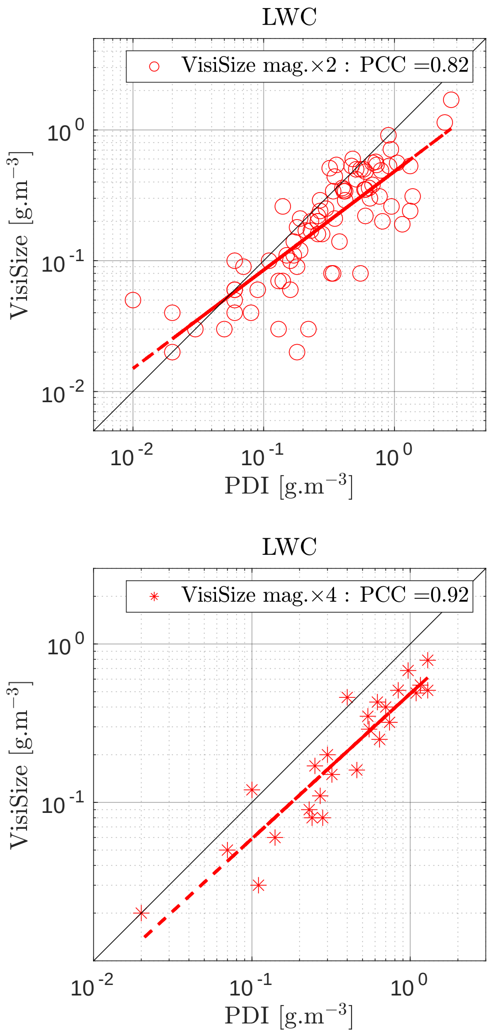

Figure 4.14: The LWC comparison between the two instruments, with cases using different lens magnification settings for the VisiSize (×2 and ×4), plotted separately. The results after applying all modifications and filters to the data, and application of PVC factor to the modified swept volume method of the PDI, are shown here. Each circle/star represents a single measurement of 15min. Dashed red lines show the LSR, and the PCC is shown in the legend.

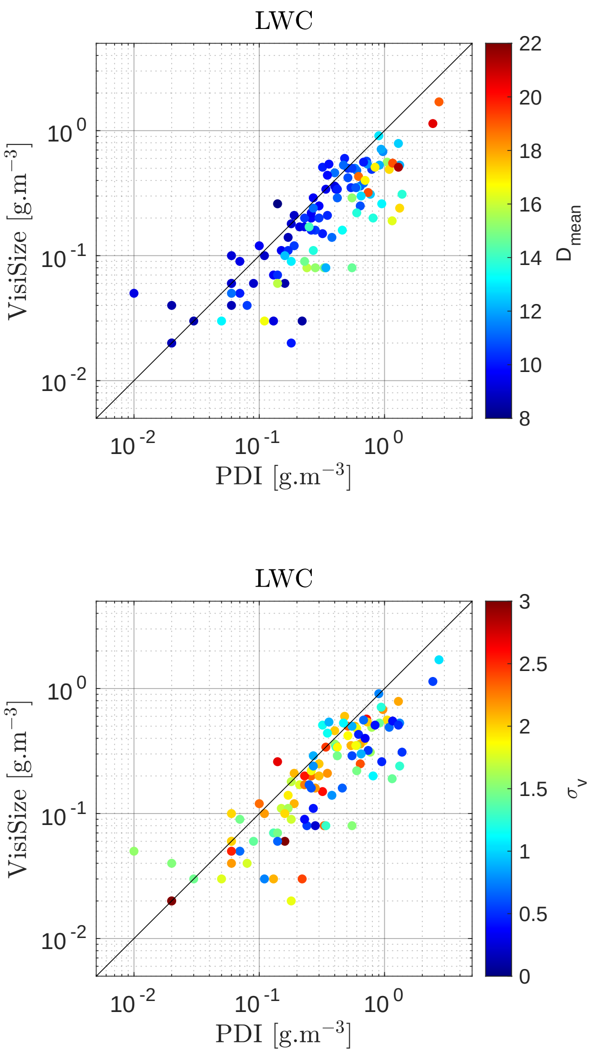

Figure 4.15: The LWC comparison between the two instruments, while the mean diameter spectra (top panel) and the standard deviation of velocity spectra (bottom panel) are also compared between the selected cases. The results after applying all modifications and filters to the data, and with application of PVC factor to the PDI swept volume method, are shown here. The mean diameters and the velocity standard deviations are taken from the VisiSize and the PDI data, respectively. Each circle represents a single measurement of ∼15 min.

canceled here by the discrepancy in the DNC, where the VisiSize values are higher (see Fig. 4.11).

In addition, it is difficult to find a clear trend by observing the bottom panel in Fig. 4.15 where the velocity standard deviation changes in the LWC scatter plot is shown. However, it seems that contrary to Fig. 4.11, cases with lower σ_v do not represent better correspondence between the two devices. The PDI mostly shows higher LWC values for these cases. It can also be because the LWC is more influenced by the discrepancy in droplet mean sizes than the DNC.

In order to further elaborate on the results, a comparison between the LWC from the two instruments is shown in Fig. 4.16 where the reciprocal fit curve in Fig. 4.9 is used to adjust the bias in the DNCs. Hence, before the LWC computation here, the DNCs from the PDI are modified based on the VisiSize results using the reciprocal fit.

Comparing this plot with the last panel of Fig. 4.13, the correlation between the two instruments is enhanced as the PCC values increased by 12% (from 0.84 to 0.94) after adjusting the DNCs from the PDI. Moreover, the LSR lines are also a little closer to 1:1 line here than in Fig. 4.13. Nevertheless, as mentioned earlier, the LWC is related to both the DNC and the volume mean diameter (LWC $\propto$ DNC $\cdot\, {D_3}^3$). Therefore, there is still discrepancy in the results due to the difference in D_3 measurements between the two instruments.

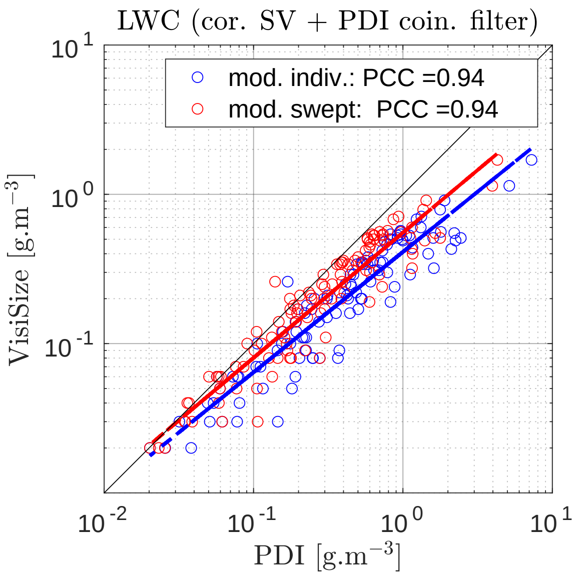

Figure 4.16: Comparison of the LWC results between the VisiSize and the PDI probe after adjusting the DNCs from the PDI using the reciprocal fit ($y = \frac{a}{x+b}$; see Fig. 4.9). The data are shown after correction of the SV, applying the coincidence filter to the PDI results, and D_{min} cutoff to both instruments' data. Each PDI method for the LWC computation is shown with a different color within the plot (each pair of blue and red circles: a selected measurement of ∼15min). Dashed blue/red lines show the LSR, and the PCCs are displayed in the legend.

4.3 Summary

Microphysical properties of cloud droplets were simultaneously measured with the VisiSize D30 and PDI-FPDR probe during a 3 - week campaign in July and August 2019 at the UFS, a mountain observatory in the German Alps. 133 measurement cases, each of them ∼ 15 minutes long, were selected for further analysis. They involved different VisiSize lens magnification settings (×2 and ×4) and running modes.

By default, correction on the size-dependent sampling volume (SV) of VisiSize was performed (see Appendix A). Moreover, the sampling volume of PDI was also modified in order to reduce the effect of velocity averaging in the DNC calculation (see Appendix B.1). Subsequently, an additional coincidence filter and then cutoff on the minimum droplet size were applied to the data in order to make a better comparison between the two instruments (see Appendices B.2 & B.3).

The DSD comparison revealed that the two instruments perform differently regarding the measurement of small droplets, while for the larger droplets ($D > 13\,\mu m$) the results correspond better. Generally, the VisiSize displayed higher sensitivity than the PDI probe in detection of very small droplets, although it has a slower detection rate since it works based on a different optical principle. Consequently, the droplet mean diameter results from the PDI were consistently between 3 and 6 µm higher than the results from the VisiSize. This was also observed by Chuang et al. (2008), where the PDI had been compared with the FSSP-100. Regarding the mean velocity of the droplets, the two instruments showed a better agreement, especially in the cases with lower mean velocity. In high-speed flows, the VisiSize seems to slightly underestimate the mean velocity due to the camera speed limit.

Comparison between the DNC results also showed a discrepancy between the two instruments similar to the Chuang et al. (2008) observations. Subsequently, by applying the SV modification, coincidence filter, and D_{min} cutoff on data, the effects of droplet size, velocity fluctuation, and lens magnification of the VisiSize on the DNC were investigated. As a result, the discrepancy between the DNCs was generally attributed to the different performance regarding smaller droplets, as well as the constraint of the PDI on velocity averaging for the DNC measurements (see Eqs. 2.10 and 2.11). The latter increases the uncertainty while we face highly turbulent clouds at the UFS.

The PDI probe was mainly designed for airborne measurements, where the velocity fluctuations are quite negligible compared to the mean flow velocity.

Moreover, the LWC measurements were also compared between the two instruments. The discrepancy in the LWC was even greater than in the DNC, and the filters were less effective. This can be due to that both discrepancies in the droplet mean size and the DNC play role in the LWC results. In addition, considering the typical reported LWC from the measurements in the Alps (e.g., Siebert et al., 2015; Spiegel et al., 2012), some unreasonably high values obtained here from the PDI suggest an occasional overestimation of the LWC by the PDI, especially when the mean droplet sizes are rather large.

In conclusion, the VisiSize D30 shadowgraph instrument was successfully applied to the cloud microphysical measurements. Furthermore, comparing the VisiSize with the PDI probe after applying the SV correction and filters to data led to a better correspondence in sizing and velocimetry than the DNC or the LWC results. Nevertheless, there are still difficulties in computing an accurate SV for a given cloud droplet size, especially for the PDI, causing discrepancies in the DNC and LWC results. Thus, it is essential to work on improving the sensors not only to remove the sizing bias but also to enhance the SV estimation accuracy.

5 In situ precipitation measurements

The results of in situ precipitation measurements with the VisiSize have been presented in this chapter. The size distributions of raindrops and precipitation particles were measured in a series of measurements during various weather events in Warsaw. The VisiSize was set up on the roof of the Institute of Geophysics, University of Warsaw (IGF-UW) alongside an "OTT Parsivel^2" laser disdrometer. I carried out both the measurements and the subsequent data analysis. The results were also accepted to be published in (Mohammadi et al., 2022b).

5.1 Precipitation measurements

As shown in the last chapter, the VisiSize functioned well during the Zugspitze campaign in terms of cloud droplet microphysical measurements. However, cloud droplets were not the only hydrometeors collected by the instrument over the course of those measurements. We encountered various weather conditions, including drizzle, freezing rain, and snow at the UFS.

Fig.5.1 shows three samples of cropped shadowgrams from a captured series during a mixed cloud-rain event at the UFS. During this measurement, the lens magnification setting $\times 2$ was used for the VisiSize. In panel (a), a raindrop of size ~ 500 µm is captured while in panels (b) and (c) a couple of cloud droplets around ~ 20 micron in diameter are detected.

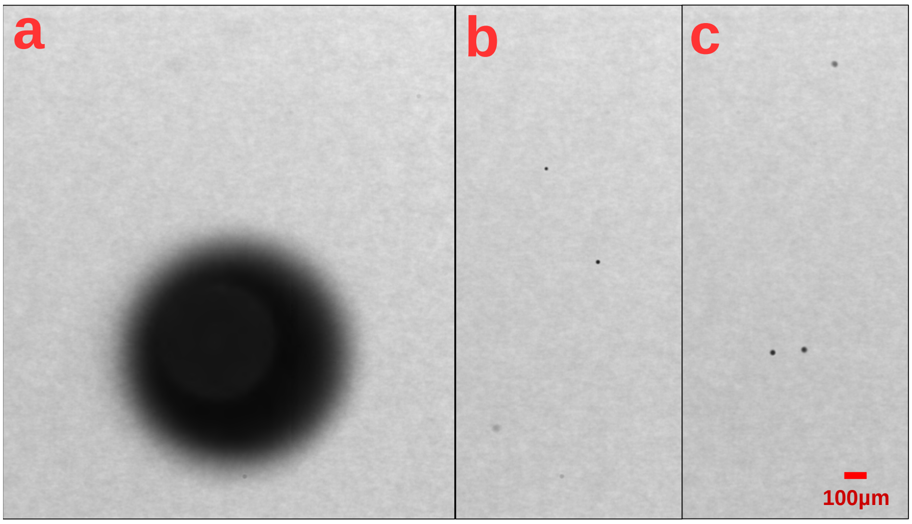

Figure 5.1: Sample shadowgrams captured during a cloud-rain mixed event at the UFS observatory on 13th of August 2019: (a) a captured rain drop; (b) and (c) a couple of cloud droplets from the same captured series.

Generally, by reducing the lens magnification settings, the field of view (FOV), depth of field (DOF), and subsequently the sample volume increases (see Table 2.1), and the VisiSize would be able to measure larger particles up to 2.25 mm. Unfortunately, during the Zugspitze campaign, there was no other instrument collecting precipitation data to be able to compare them with the VisiSize. However, I conducted another series of measurements on the roof of IGF-UW where the VisiSize was mounted next to an optical disdrometer, OTT Parsivel^2 (see Sect. 2.2.2) which could simultaneously measure raindrops and precipitation particles (see Fig. 5.2).

While the Parsivel disdrometer is a standard, fully automated instrument and collects data continuously, the VisiSize requires manual operation, the presence of the investigator in the course of the measurements, and initial

Figure 5.2: "VisiSize D30" shadowgraph instrument (front) and "OTT Parsivel^2" laser disdrometer (back) deployed next to each other at Meteo-station on the rooftop of the Institute of Geophysics, University of Warsaw (IGF-UW).

calibration between each measurement series. Thus, data collection was limited to the precipitation events when such an operation was possible. During the mixed-phase and ice-phase precipitation, I focused mainly on capturing shadowgram series and post-processing them afterward, while the automatic live processing of data was used for rain events which allowed for efficient data collection.

Figure 5.3 illustrates 10 samples of cropped shadowgrams of raindrops, ice particles and snowflakes captured with the VisiSize during the in situ experiments. As it is shown, the VisiSize is not only capable of detecting micron-sized cloud droplets, but it can also capture images of raindrops and precipitation particles up to 2.25 mm in diameter size.

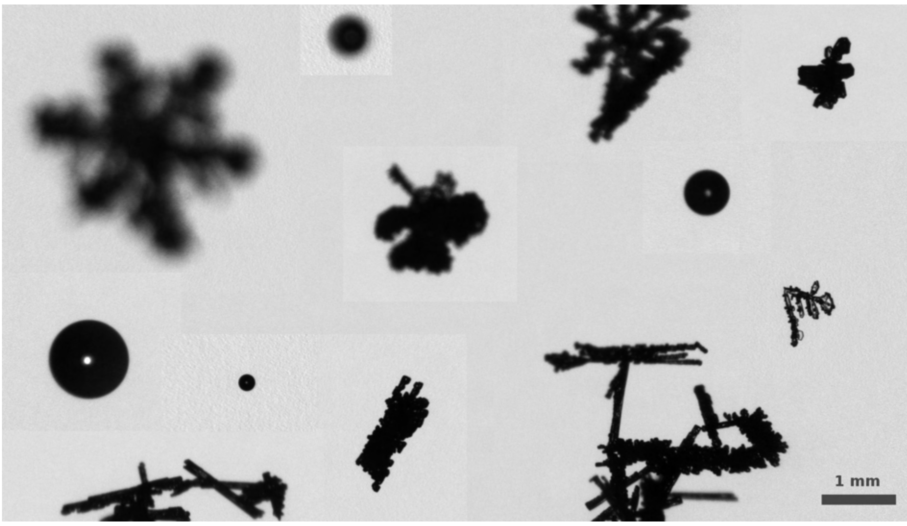

Figure 5.3: Sample cropped shadowgrams of raindrops, ice particles, and snowflakes captured during different weather events of Warsaw with the VisiSize deployed on the rooftop of IGF-UW.

5.2 Results and discussion

After initial processing of collected data, a few case studies were selected in which enough data were recorded by both instruments simultaneously. The probability size distributions were used to compare the data between the VisiSize and the Parsivel. Using probability size distribution allows for merely comparing the sizing performances between the two instruments without being influenced by their different sample volumes.

Figure 5.4 shows data collected during a rain event in Warsaw on 18th of November 2018. The detected droplet counts and arithmetic mean values are also shown below the legend. The difference in sizing range and the effect of drizzle drops on the arithmetic mean values are apparent in these histograms. The instruments' total number of counts is different due to the difference in measuring volumes (see Tables 2.1 & 2.3). Moreover, the

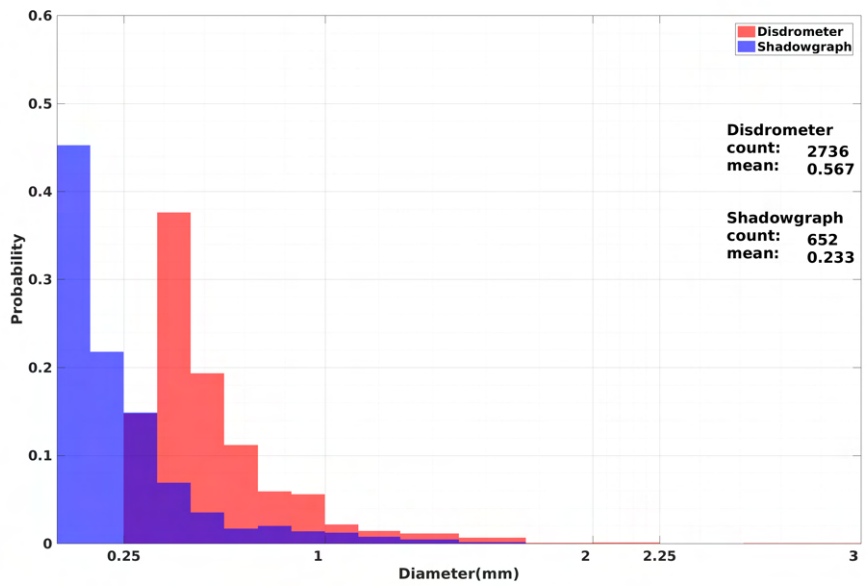

Figure 5.4: The DSD histograms of raindrops collected on the rooftop of IGF-UW on 18th of November 2018, 20:26' - 23:54'.

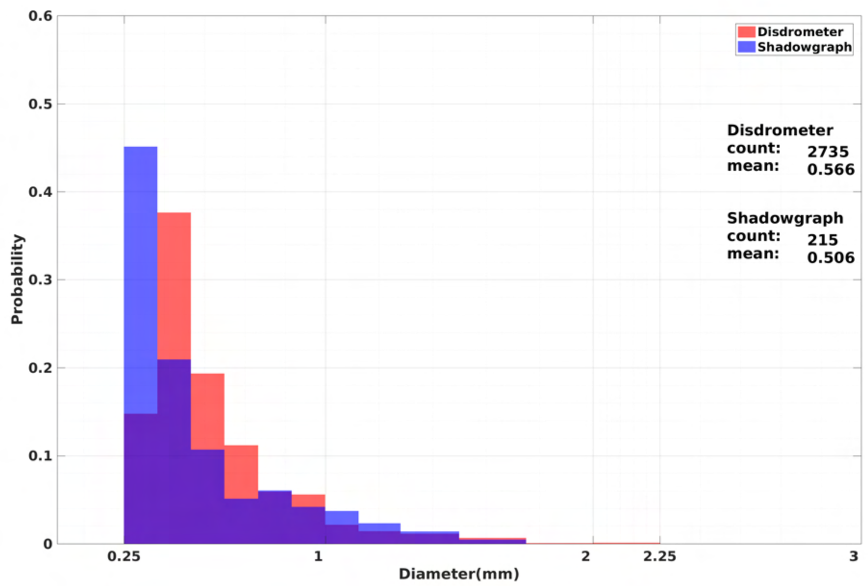

Figure 5.5: The DSD histogram of the same measurement as Fig. 5.4, while drops out of common measuring range (0.25 - 2.25 mm) were excluded.

arithmetic mean value for the VisiSize is lower than the disdrometer. It must be noted that the purple color on the graph simply represents the area where the two histograms from the VisiSize (blue) and Parsivel (red) overlap each other.

Figure 5.5 shows the same measurement data while only analyzing drops within the common sizing range of the two instruments (0.25 - 2.25 mm). Consequently, the arithmetic mean values and size distributions correspond better. However, the discrepancy between results in the smallest size bin (0.25 - 0.37 mm) does still exist, and the VisiSize data show almost three times higher value in this range which could be attributed to the inaccuracy of the Parsivel in drizzle mode.

Figures 5.6 & 5.7 also show the DSD comparison between the two instruments before and after excluding particles out of the common sizing range, respectively. The data were collected during a snow event in Warsaw on 24th of December 2018. The same trend as the previous measurement case is also observed here after limiting particle size to the common measuring range. However, the agreement between the results seems better than the previous plots. It can be thanks to having more precipitation particles compared to the drizzles and small particles in this case which not only increased the arithmetic value but also slightly weakened the effect of drizzles for the DSD.

Additional examples of simultaneous measurements with the VisiSize and the Parsivel are shown in Figs. 5.8 & 5.9. The size distributions of raindrops and precipitation particles collected with the two instruments compared with each other, excluding the drops out of the common sizing range same as Figs. 5.5 & 5.7.

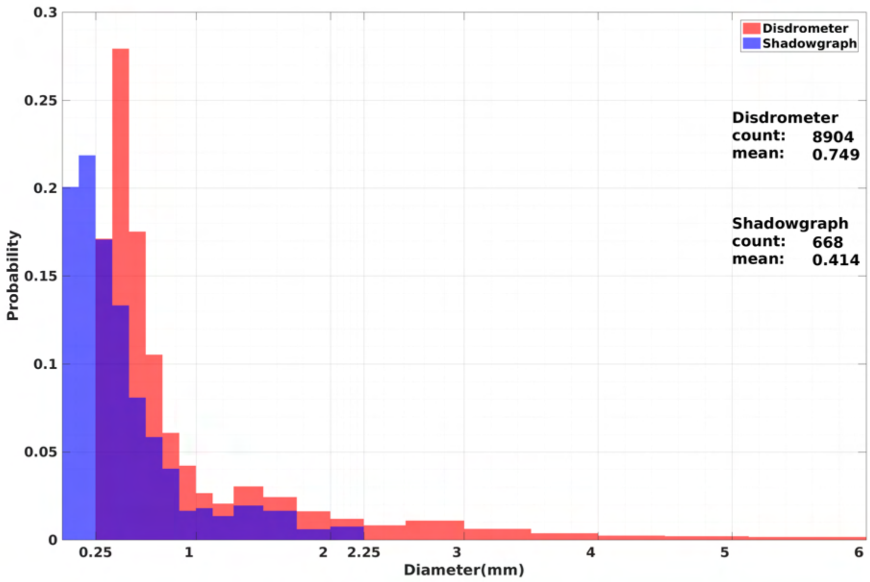

Figure 5.6: The DSD histogram of precipitation particles collected on the rooftop of IGF-UW on 24th of December 2018, 21:28' - 24:00'.

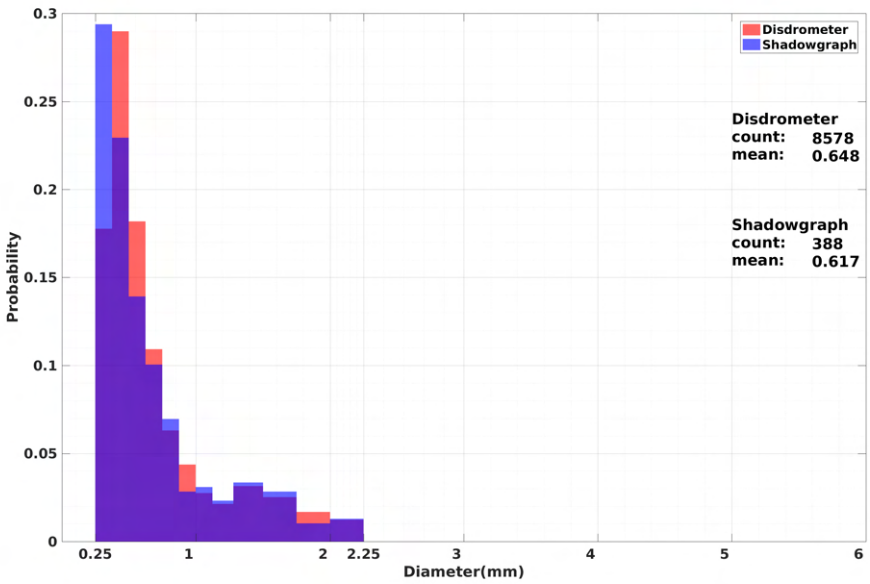

Figure 5.7: The DSD histogram of the same measurement as Fig. 5.6, while particles out of the common measuring range (0.25 - 2.25 mm) were excluded.

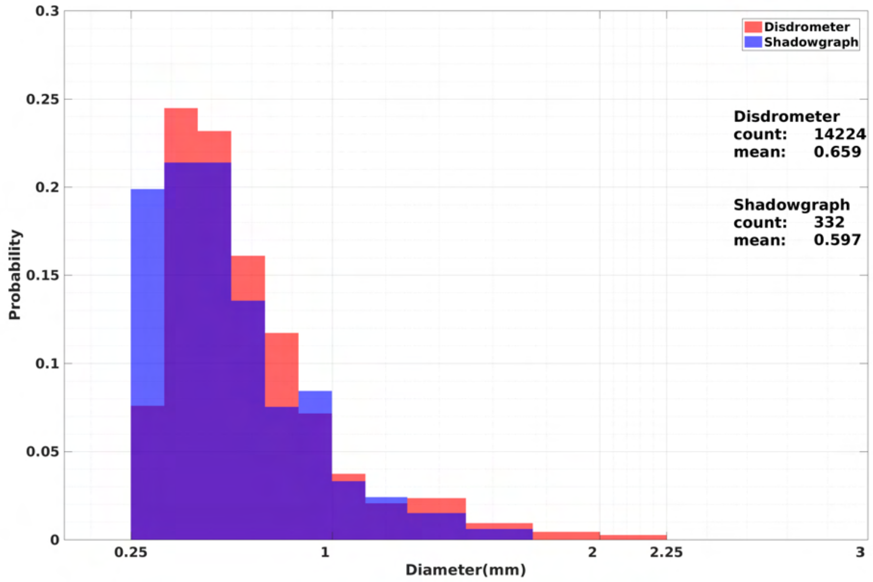

Figure 5.8: DSD histogram of raindrops collected on the rooftop of IGF-UW on 13th of November 2018, 19:27' - 24:00', while drops out of common measuring range (0.25 - 2.25 mm) were excluded.

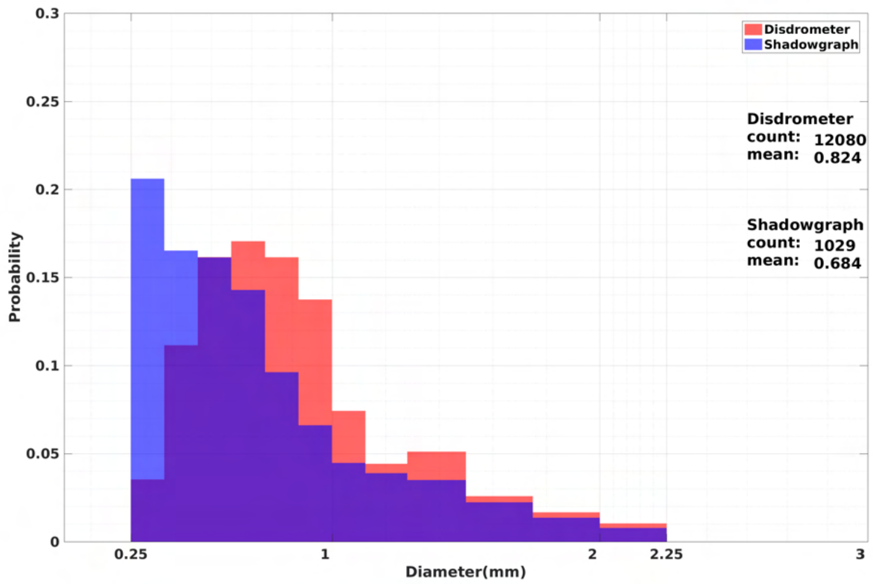

Figure 5.9: DSD histogram of precipitation particles collected on the rooftop of IGF-UW on 31st of January 2019, 11:10' - 12:46', while particles out of common measuring range (0.25 - 2.25 mm) were excluded.

5.3 Summary

The drop size distribution of hydrometeors, collected in a series of simultaneous measurements with the VisiSize shadowgraph system and the Parsivel laser disdrometer was investigated. The two instruments were deployed on the rooftop of the Institute of Geophysics, University of Warsaw. Each measurement series was planned based on the weather forecast and man resources availability. Eventually, a couple of case studies were selected including different weather events in which shadowgrams of raindrops and precipitation particles were captured by the VisiSize.

In conclusion, the VisiSize was successfully applied to precipitation measurements. Furthermore, a comparison between the VisiSize and Parsivel disdrometer showed a better correspondence in DSDs within the mid-sized range drops than in the smallest sizes (drizzle mode). Considering the capability of the VisiSize to accurately measure the drizzle mode, the discrepancies can be attributed to the difficulties in measuring drizzles with the Parsivel which were also observed in the past (see Sect. 2.2.2).

Consequently, the synergy of the two techniques can lead to more precise DSD measurements for the hydrometeors. However, the differences in measurement size ranges and sampling volumes of the two instruments for further investigations of the kinetic energy of different types of precipitation must be carefully taken into account.

6 Conclusion and outlook

During this study, a shadowgraph imaging system, VisiSize D30, manufactured by Oxford Laser Ltd. and originally designed for sizing industrial sprays, was adapted for cloud microphysical measurements.

The VisiSize works based on Particle/Droplet Image Analysis method which was introduced by (Kashdan et al., 2003). It captures shadow images of droplets at up to 30 frame per second with a high-resolution camera, counts them, and estimates droplet sizes while correcting for image blurring due to out-of-focus droplet positions. First round of laboratory tests using polydisperse cloud-like water droplets performed by J. L. Nowak resulted in developing a suitable correction method to improve estimations of droplet number concentration and size distribution with the VisiSize. The minimum droplet diameters providing uniform detection were also obtained during these tests.

Then, another series of laboratory tests with the VisiSize were conducted using a monodisperse droplet generator, FMAG 1520. In spite of encountering significant droplet collisions and evaporation during the experiments, the sizing accuracy of VisiSize was verified after filtering out collisions by selecting the first major peak of size histograms. The difference between the VisiSize reports and generated droplet sizes by FMAG was no larger than

2µm or 5%, for lens magnification settings ×2 and ×4.

Next, the VisiSize was used for the first time to measure cloud droplets during a research campaign at the UFS in the German Alps. Simultaneous measurements were also performed with a PDI-FPDR probe deployed next to the VisiSize. Cloud droplet microphysical properties, such as mean droplet diameters ($\bar{D}, D_2, D_3$), DSD, DNC, and LWC were measured. The results from the two instruments were compared after applying sample volume corrections and cutoff on the minimum droplet sizes for both instruments as well as coincidence filter on the PDI data.

Comparing the VisiSize with the PDI probe after applying the SV correction and filters to data led to a better correspondence in sizing and velocimetry than the DNC or the LWC results. With respect to the sizing comparison with the PDI, the results were similar to the observations by Chuang et al. (2008) and Bertens et al. (2021) where the PDI was compared to the FSSP-100 and Lagrangian Particle Tracking (LPT), respectively.

Performing a particle tracking experiment with the two instruments in the laboratory can be beneficial for future investigation of the DNC measurements. Nevertheless, there are still difficulties in computing an accurate SV for a given cloud droplet size, especially for the PDI, causing discrepancies in the DNC and LWC results. Thus, it is essential to work on improving the sensors not only to remove the sizing bias but also to enhance the SV estimation accuracy.

Moreover, some precipitation measurements also performed by the VisiSize together with a Parsivel laser disdrometer on the roof of Institute of Geophysics, University of Warsaw. A comparison between the VisiSize and

Parsivel disdrometer showed a better correspondence in DSDs within the mid-sized range drops than in the smallest sizes (drizzle mode). Considering the capability of the VisiSize to accurately measure the drizzle mode, the discrepancies were attributed to the difficulties in measuring drizzles with the Parsivel. Consequently, the synergy of the two techniques can lead to more precise DSD measurements for the hydrometeors. However, the differences in measurement size ranges and sampling volumes of the two instruments for further investigations of the kinetic energy of different types of precipitation must be carefully taken into account in the future.

In conclusion, the VisiSize D30 shadowgraph instrument was effectively applied to cloud microphysical measurements. It performed satisfactorily under windy, cloudy, and humid weather conditions. Moreover, it could be shown that the VisiSize, itself, can not only be used for direct measurement of hydrometeors, but also can be considered as a reliable tool to verify new droplet/particle sizing systems in atmospheric physics. It was recently used to validate a low-cost optical particle counter OPC-N3 for microphysical measurements of fog (Nurowska et al., 2022). In addition, it is meanwhile operating on a fog measurement campaign at Aerosol and Radiation Observatory (AOD) in Strzyżow, Poland.

Appendices

A
Laboratory experiments with cloud-like droplets

The first series of laboratory tests with the VisiSize are diagnostic experiments in which the effectiveness of built-in software algorithm in terms of detection probability and homogeneity which affect statistics of the DSD and DNC were investigated. These tests were performed by my colleague, J. L. Nowak at the Fluid Mechanics Lab at the Institute of Geophysics of the University of Warsaw.

Later, I used the corrections resulting from these experiments in analyzing data from real cloud droplets. Hence, in this section, a brief description along with the most significant results of these laboratory tests are provided. More details are available in Sect. 3 from Nowak et al. (2021).

A.1 Experimental set-up

A dense stream of poly-disperse water droplets was generated with the use of an ultrasonic humidifier, the same as in the study of Korczyk et al. (2012) who measured the droplet size to be mostly in the range of 2 - 20 µm in diameter (Fig. 1 there). Differences in delivery method and in ambient conditions could result in a little different spectrum. In the current setup, the cloud of droplets was delivered from the humidifier into the sample volume (SV) with 4 cm wide, 70 cm long circular plastic pipe.

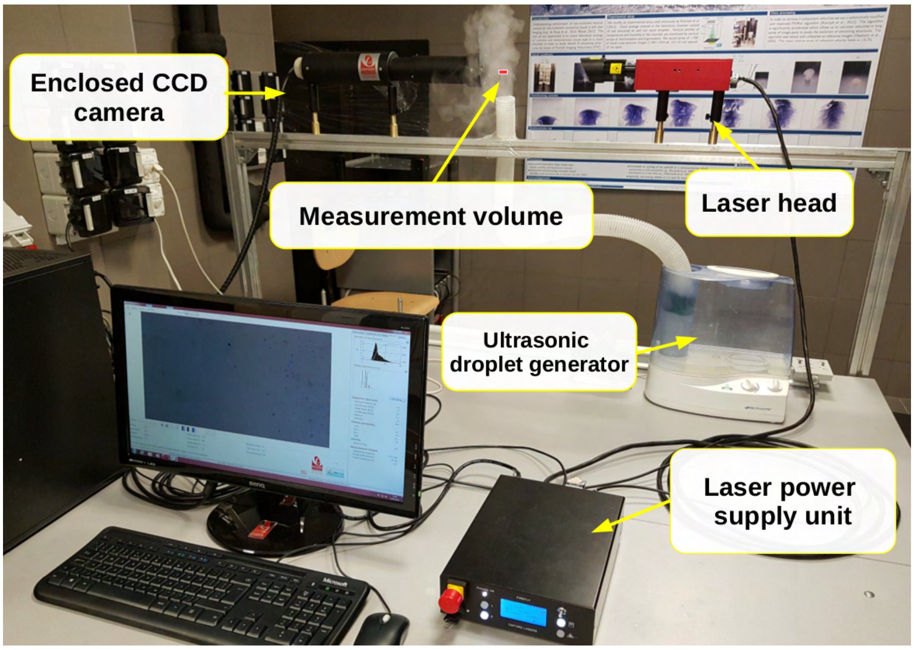

Figure A.1: Experimental setup for studying the detection properties. The main parts of the VisiSize D30 are an infrared pulse laser with a diffuser (top right) and a CCD camera with the lens objective enclosed in a waterproof housing (top left). Water droplets produced with an ultrasonic droplet generator are measured while passing through the sample volume (top middle) located close to the camera.

Care was taken to fill the whole shadowgraph SV with the stream of droplets though both the flow and the particle field were not exactly homogeneous. The flow velocity was estimated to be of the order of 10 $\mathrm{cm\,s^{-1}}$ and the direction of the flow was aligned horizontally from left to right (i.e. the direction of the pipe exit was perpendicular to what is shown in Fig. A.1. For each of the three lens settings ($\times 1$, $\times 2$, $\times 4$) laser power was adjusted to reach optimal background brightness of the pictures, and 10 min long measurement in live mode was performed.

Figure A.2 presents an example image captured during the experiment.

Statistics reported by the software for each run are listed in Table A.1.

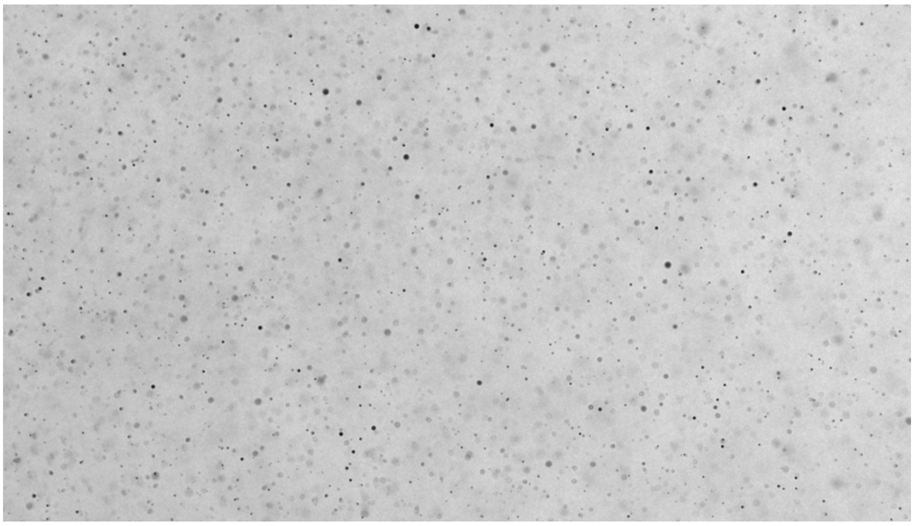

Figure A.2: A typical shadow image of droplets produced by ultrasonic droplet generator taken during laboratory tests with the camera lens magnification ×2.

Table A.1: Statistics of the laboratory experiment with poly-disperse droplets for different lens magnification settings.

Lens setting	**×1**	**×2**	**×4**
Video frames	17705	17670	17695
Empty frames	3390	4508	8156
Total counts	602232	951642	324625
Counts/frame	34.0	53.9	18.3
min. diameter [µm]	7.9	4.6	3.2

A.2 Detection properties

The sample volume within which a droplet is detectable depends on the size of the droplet because blurring caused by defocus affects images of particles with different sizes differently. This fact must always be taken into account when estimating the droplet concentration (in a unit volume). The solution implemented in the software assumes a linear relationship between the depth of field and particle diameter which is efficient for relatively large objects (D > 260 µm; the exact value depends on the lens magnification). However, for small droplets such as those in clouds, an additional focus rejection criterion imposes a much stronger limit on the acceptable depth of field.

At a sufficiently large distance from the focal plane, the particle image starts to fade into the background, meaning that it is no longer distinguishable. Simultaneously, the halo takes over almost the whole particle image. To avoid measuring objects with signal-to-noise ratios that do not permit proper sizing, a simple rejection limit is exercised by the software:

$$A_h < 0.95 A_p \tag{A.1}$$

where A_h refers to the halo area around the particle while A_P is the total particle area. Importantly, it is not possible for the user to deactivate this option in version 6.5.39 of the software. This condition imposes an upper limit on the range of values that A_h can take. Note that large values of A_h are attained only for relatively large droplets and at far defocus. Accordingly, the range of the total particle area A_p is also limited for a given diameter. It can grow with defocus distance z but only to the point where the halo constitutes 95% of the image at most. Otherwise, the particle is rejected.

Using the Eqs. (2.1)-(2.2) for replacing A_h and A_p with terms based on droplet size (D) and defocus distance (z) in the above condition for the acceptable range of defocus distance, the corrected depth of field (DOF), z_{95}, is introduced as follows:

$$z_{95} = \frac{0.95}{(1-0.95a_3)(a_1 D + a_2)} \frac{\pi}{4} \frac{(D + a_4 + a_5)^2}{\text{pix}^2} \tag{A.2}$$

The effect of the above condition is shown in Fig. A.3. For all droplets measured in the diagnostic experiment, Eq. (A.1) leads to a much stronger limit on the effective sample volume than what Eq. (2.3) does. Predicted ranges of defocus distance agree very well with values of $z_{\texttt{max}}$ found in the experimental dataset.

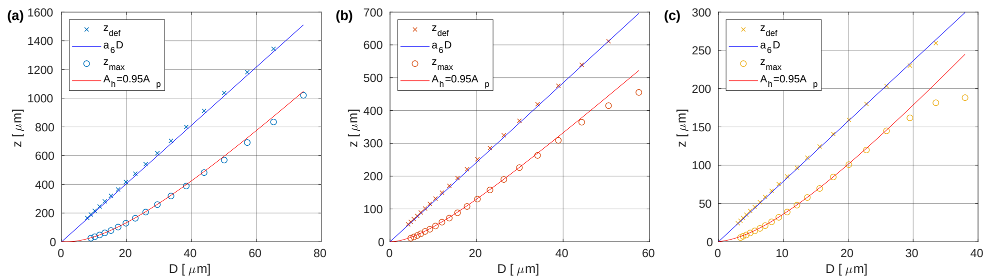

Figure A.3: Maximum range of defocus distance z for each size bin: derived from the volumes listed in summary file from VisiSize software (shown with $\times$) versus the actual maximum values $z_{\texttt{max}}$ found in the experimental data (shown with $\circ$), together with two analytical approximations - default $z_{\texttt{def}}$ and corrected z_{95}. Measurement series for lens magnification settings: (a) $\times$1, (b) $\times$2, (c) $\times$4.

As is shown in Fig. A.3, $z_{\texttt{def}}$, the default DOF based on the linear relation between the depth of field and droplet size assumed by the built-in software algorithm, overestimates the DOF. This also affects the relevant sample volume and leads to an underestimated number concentration. Therefore, instead of the default sample volume shown in Eq. (2.6), two corrected sample volume formulas based on z_{95} are introduced below alongside the default method:

$$V_k^{\texttt{def}} = 2\, z_{\texttt{def}}|_{D_k} (L_x - D_k)(L_y - D_k) \tag{A.3}$$

$$V_k^{\mathtt{cor}} = 2\, z_{95}|_{D_k}(L_x - D_k)(L_y - D_k) \tag{A.4}$$

$$V_i^{\mathtt{ind}} = 2\, z_{95}|_{D_i}(L_x - D_i)(L_y - D_i) \tag{A.5}$$

where L_x and L_y denote the size of the FOV in m and k is the size bin number. In Eq. (A.5), i is the individual droplet index as in this method a sample volume around each individual droplet is counted separately. The impact of the selected DOF limit on the effective SV around a droplet is shown schematically in Fig. A.4.

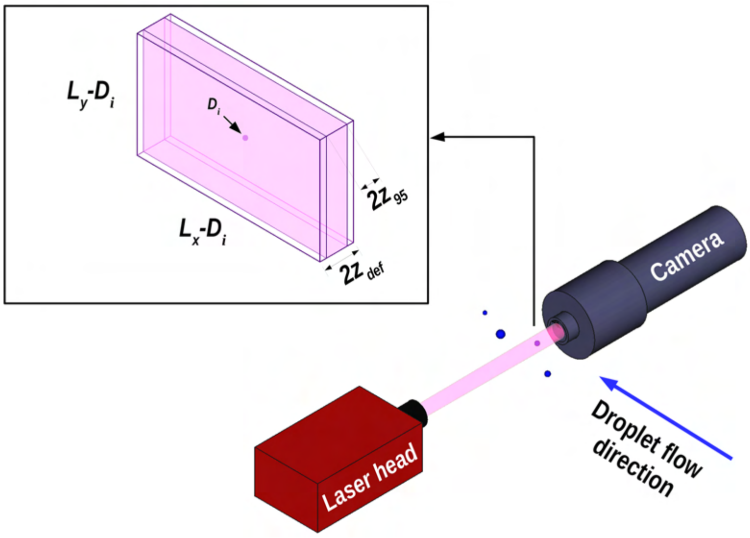

Figure A.4: Schematic illustration of the difference between the default and the corrected/individual sample volumes while having the same field of view $S = (L_x - D_i)(L_y - D_i)$, but different depths of fields ($z_{\mathtt{def}}$ vs. z_{95}).

Subsequently, the normalized droplet number concentrations by size for each size bin are calculated as follows:

$$N_{\mathtt{VD}}^{\mathtt{def}}\langle k\rangle = \frac{M_k}{F\ \Delta D_k\ V_k^{\mathtt{def}}} \tag{A.6}$$

$$N_{\mathtt{VD}}^{\mathtt{cor}}\langle k\rangle = \frac{M_k}{F\ \Delta D_k\ V_k^{\mathtt{cor}}} \tag{A.7}$$

$$N_{\mathtt{VD}}^{\mathtt{ind}}\langle k\rangle = \frac{1}{F\Delta D_k} \sum_{i:D_k\le D_i<D_{k+1}} \frac{1}{V_i^{\mathtt{ind}}} \tag{A.8}$$

where $M_k = |\{i : D_k \le D_i < D_{k+1}\}|$ is the number of counts within bin k, $\Delta D_k = D_{k+1} - D_k$ is the bin width and F simply the number of frames included in an analysed series. The total DNC can be calculated by suitable integration with respect to the whole range of diameters, which is in practice a sum over the bins for the default and corrected methods and a sum over individual counts in the case of individual method:

$$N_{\mathtt{V}}^{\mathtt{def}} = \sum_k N_{\mathtt{VD}}^{\mathtt{def}}\langle k\rangle\ \Delta D_k \tag{A.9}$$

$$N_{\mathtt{V}}^{\mathtt{cor}} = \sum_k N_{\mathtt{VD}}^{\mathtt{cor}}\langle k\rangle\ \Delta D_k \tag{A.10}$$

$$N_{\mathtt{V}}^{\mathtt{ind}} = \frac{1}{F}\sum_i \frac{1}{V_i^{\mathtt{ind}}}\ . \tag{A.11}$$

Figure A.5 indicates an important observation during the lab experiments. The DSDs obtained by using Eqs. (A.6)-(A.8) for data collected with different lens magnification settings shows that the values of $N_{\mathtt{VD}}(D)$ are considerably underestimated by the default method. It is actually expected as using Eq. (A.3) provides sample volumes larger than the true ones.

On the other hand, there is no significant difference between corrected and individual SVs. This observation suggests that even without having data for individual droplets usually contained in a particle file, still reasonable DSD can be obtained by correcting accumulated counts listed in a summary file.

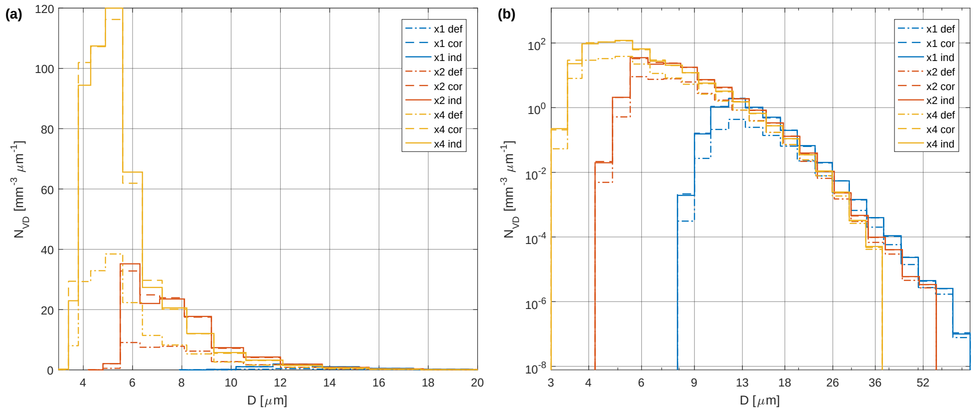

Figure A.5: Comparison of droplet size distributions obtained with three methods, default (def), corrected (cor) and individual (ind), during the three measurement series differing in lens magnification settings. The same data are plotted in (a) linear and (b) logarithmic scales.

Moreover, the analysis of detections in a dense polydisperse stream of droplets implied that the minimum droplet size for reliably uniform detection is larger than the resolution in the focal plane as shown in Fig. A.5. This minimum droplet size was estimated to be ∼6 and ∼12 µm for the camera lens magnification settings ×2 and ×1, respectively. It can potentially be enhanced by careful data conditioning, i.e. with a strong limit on the estimated distance from the focal plane, but at the cost of decreasing the sample volume.

Table A.2 summarizes the results obtained for the polydisperse stream produced by an ultrasonic generator. The DNC is about 3–4 times larger for the corrected and individual methods than for the default one. In all cases, statistics for the diameter are lower for the new methods than for the default. This can be explained by noting that the largest relative difference in SVs between the methods appears for the smallest droplets (see Fig. A.3), so it is their contribution to the DSD that changes most.

Furthermore, detection probability was found to be satisfactorily homogeneous across the field of view, except for the small magnification setting (×1). Minor issues with respect to the axial direction were revealed, which were probably caused by substantial diffraction effects on small droplets.

Table A.2: Results of the laboratory experiment with poly-disperse droplets: comparison of different methods used for estimating size-dependent sample volumes.

Lens setting	**×1**			**×2**			**×4**		
Method	**def**	**cor**	**ind**	**def**	**cor**	**ind**	**def**	**cor**	**ind**
N_V [mm^{-3}]	2.1	8.6	8.6	37.3	112.2	112.3	114.1	331.6	330.1
$\bar{D}$ [µm]	14.1	13.7	13.7	8.3	7.9	7.9	6.0	5.7	5.7
D_2 [µm]	14.5	13.9	14.0	8.6	8.2	8.3	6.4	6.0	6.0
D_3 [µm]	14.9	14.2	14.3	9.1	8.6	8.6	6.9	6.4	6.4
D_e [µm]	15.7	14.9	15.0	10.0	9.4	9.4	8.0	7.3	7.3
LWC [g m^{-3}]	3.6	13.0	13.2	14.5	37.3	37.7	19.6	45.7	46.2

$D_e = D_3^3/D_2^2$

B

Applied Modifications and Filters to PDI data

B.1 Modified swept method

As mentioned in Sect. 2.2.1, the calculation of DNC by the PDI software is based on the average velocity of the droplets passing through the probe volume. Hence, in order to improve the results reported by the PDI, the swept volume method was modified to reduce the effect of averaging the velocity as much as possible.

The first step was to split the long run of measurements into smaller time bins (1 minute or shorter periods) and apply the swept method to each period separately, which allows us to account for changes in conditions (e.g., wind speed). In addition, instead of bin edges, the bin centers were used to calculate the probe area.

Another way to modify the swept volume method is to use the inter-arrival time of each droplet to measure the air volume passing through the probe. Contrary to the default swept volume method, where all droplets within a size bin are assumed to have the same probe volume (PV), in this approach, which is called the individual method, every single droplet j has its own swept volume of air, given as:

$$V_j = \mathrm{PA}_j |v_j| \tau_j \ , \tag{B.1}$$

where PA is the probe area for the droplet, dependent on its size, multiplied by droplet velocity and its inter-arrival time, which is defined below as half of the time period between the detection of the previous and next droplet:

$$\tau_j = \frac{t_{j+1} - t_{j-1}}{2} \ . \tag{B.2}$$

Consequently, the DNC is calculated as follows:

$$N_V^{\mathrm{ind}} = \frac{n}{\sum_j V_j} \ . \tag{B.3}$$

The aforementioned modifications to the PDI DNC calculations helped to obtain more accurate results by preventing errors caused by averaging the velocity and size. However, after preliminary data processing, it was revealed that data require further corrections which are introduced below.

B.2 Coincidence filter

Typically in instruments that count droplets one by one, a measurement artifact known as "coincidence" occurs when more than one droplet is registered at the same time resulting in multiple droplets artificially measured as one droplet. It has been extensively studied for Forward Scattering Spectrometer Probe (FSSP), Cloud Droplet Probe (CDP), and Cloud and Aerosol Spectrometer (CAS) (e.g., Cooper, 1988; Burnet and Brenguier, 2002; Lance et al., 2010; Lance, 2012).

On the other hand, for the PDI as the probe volume, which is defined by the intersection of two laser beams, can be easily reduced, the occurrence of coincidence is expected to be less likely. The probe volume diameter of the PDI, which is determined by the beam diameter, laser wavelength, and transmitter focal length, has been optimized by the manufacturer to minimize the coincidence error. For instance, the probe volume for a typical cloud droplet size of 15 µm is estimated to be smaller than 10^{-5} cm^3. Considering a dense cloud with a droplet number concentration equal to 1000 cm^{-3}, the average number of droplets within the probe volume would be less than 0.005. Hence, assuming a homogeneous droplet distribution (i.e. disregarding droplet clustering), the probability of having more than one droplet in the probe volume, given by a Poisson distribution, would be less than 0.000012. Consequently, the occurrence of coincidence is presumably unlikely. Nevertheless, the effects of possible coincidence on PDI data have been discussed in Chuang et al. (2008).

During the measurements at the UFS, however, we encountered coincidence phenomena in a slightly different way than mentioned above. In raw data of cloud droplets collected by the PDI probe, simultaneously recorded counts were found with identical detection times. Their size and velocity values were similar with differences usually less than 2.0 µm and 0.1 m.s^{-1}, respectively.

Following Chuang et al. (2008), they were assumed to be actually one droplet recorded more than once by the PDI as a consequence of multiple triggering. This error is usually attributed to the noisy environment which in our case could be the cloud droplets flow passing between the transmitter and probe volume resulting in fluctuations of laser light intensity at the beam intersection.

Consequently, I have used a filter to reduce the effect of this error as much as possible. The “coincidence filter” replaces all droplets detected simultaneously with a single droplet, which possesses the average size and velocity of the multiple droplets. However, it does not correct the data for the improbable occurrence of multiple droplets simultaneously present in the PDI probe volume.

B.3 D_{min} cutoff

Another filter that is applied to the raw data is the D_{min} cutoff. As was mentioned earlier for Eq. 2.9, the PDI software obtains D_{min} value by fitting a model to raw data after each measurement run. Thus, each time D_{min} takes a different value below which the PDI cannot reliably measure droplets. The PVC factor for all size bins smaller than D_{min} is also equal to zero. Hence, their probability distributions in the DSD histogram for the PDI are zero when the PVC factor is applied.

However, over the course of our measurements, sometimes the PDI recorded droplets smaller than D_{min} within the raw data. Therefore, in order to have more accurate results, I put a D_{min} cutoff on the data, which excludes all droplets smaller than D_{min} from analysis while the data are modified. This filter is also applied to the VisiSize data to be able to make a better comparison between the instruments in Chapter 4.

C PDI channel 1

As was mentioned in Sect. 4.1, the PDI channel 1 did not function properly during the summer 2019 campaign. Hence, all PDI results presented in Chapter 4 were obtained from channel 2, which is supposed to be less sensitive in the detection of very small droplets. However, there were some data available from measurements at Zugspitze in the summer 2018, where the PDI channel 1 functioned reliably in cloud droplet measurements. Those experiments were conducted with both VisiSize and PDI channel 1 at the same measurement site in the UFS.

Nonetheless, the number of simultaneous measurements with large enough collected samples were so limited that performing comprehensive analysis on them was difficult. In addition, the available simultaneous measurements have also different lengths varied between ~ 7 - 14 minutes. Thus, I could select only 12 measurement cases to show a comparison between the VisiSize and the PDI channel 1 regarding the arithmetic mean diameter of droplets in Fig. C.1.

The result is similar to what was shown in Sect. 4.2.2 for the PDI channel 2. The arithmetic mean from the PDI channel 1 is consistently higher than the VisiSize just as it was higher from the PDI channel 2 (see Figure 4.5). However, the difference in mean values from the two instruments is lower

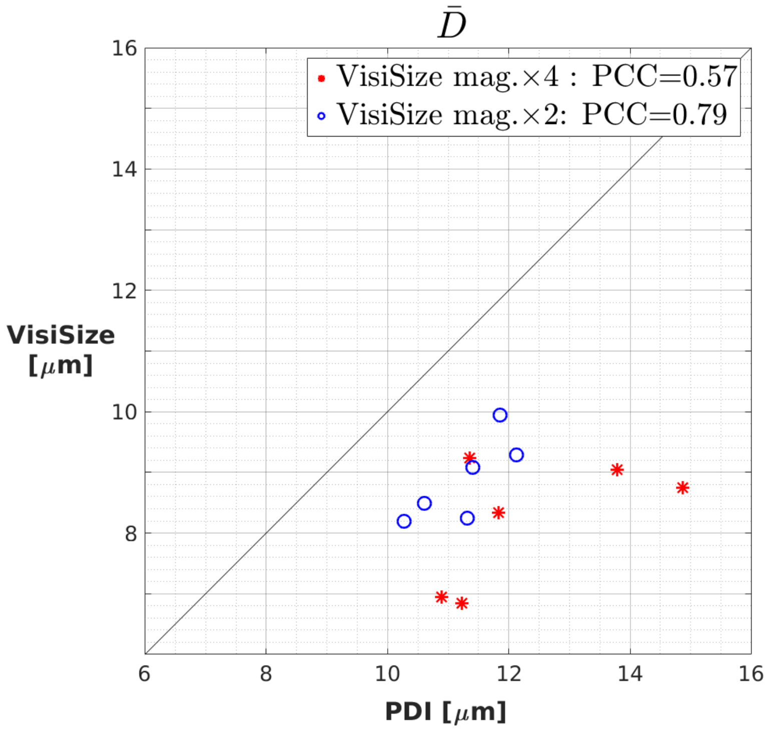

Figure C.1: Comparison of droplet arithmetic mean diameters between the VisiSize and the PDI probe channel 1. The blue circle represents measurement cases where the VisiSize lens magnification ×2 was used, while the red star shows the measurements with magnification ×4. Each measurement case was between ∼ 7 - 14 minutes long, while both instruments were collecting cloud droplets data simultaneously. The Pearson correlation coefficient (PCC) is also shown in the legend.

when the VisiSize lens magnification ×2 was used than in cases measured with ×4. The mean values from the PDI and VisiSize with magnification ×2 differ between 2 and 3 µm, while the PDI comparison to the cases with magnification ×4 shows between 2 and 6 µm difference.

As expected, the higher lens magnification in the VisiSize is more sensitive in the detection of the smallest cloud droplets which results in a lower mean value and consequently a larger difference with the PDI results. Therefore, the two instruments correspond better in sizing cloud droplets when the

VisiSize lens magnification ×2 and the PDI channel 1 were used.

References

Artium Tech. Inc. https://www.artium.com/pdi-theory-of-operation. Accessed: 2022-09-03.

AS Dept. UW. URL http://www.atmos.uwyo.edu/uwka/wcr/.

W. D. Bachalo and M. J. Houser. Phase/Doppler Spray Analyzer For Simultaneous Measurements Of Drop Size And Velocity Distributions. *Optical Engineering*, 23(5):235583, oct 1984. ISSN 0091-3286. doi: 10.1117/12.7973341.

William D. Bachalo. Method for measuring the size and velocity of spheres by dual-beam light-scatter interferometry. *Applied Optics*, 1980. ISSN 0003-6935. doi: 10.1364/ao.19.000363.

William D. Bachalo and Subramanian V. Sankar. Phase doppler particle analyzer, 2016.

T. L. Barone, E. Hesse, C. E. Seaman, A. J. Baran, T. W. Beck, M. L. Harris, P. A. Jaques, T. Lee, and S. E. Mischler. Calibration of the cloud and aerosol spectrometer for coal dust composition and morphology. *Advanced Powder Technology*, 30(9):1805–1814, sep 2019. ISSN 15685527. doi: 10.1016/j.apt.2019.05.023.

BAS. URL https://www.bas.ac.uk/polar-operations/sites-and-facilities/facility/airborne-science-and-technology/twin-otter-meteorological-airborne-science-instrumentation-masin/.

Darrel Baumgardner and Alexei Korolev. Airspeed corrections for optical array probe sample volumes. *Journal of Atmospheric and Oceanic Technology*, 14(5):1224 – 1229, 1997. doi: 10.1175/1520-0426(1997)014⟨1224:ACFOAP⟩2.0.CO;2.

Matthew J. Beals, Jacob P. Fugal, Raymond A. Shaw, Jiang Lu, Scott M. Spuler, and Jeffrey L. Stith. Holographic measurements of inhomogeneous cloud mixing at the centimeter scale. *Science*, 2015. ISSN 10959203. doi: 10.1126/science.aab0751.

Alexander Beck, Jan Henneberger, Sarah Schöpfer, Jacob Fugal, and Ulrike Lohmann. HoloGondel: in situ cloud observations on a cable car in the Swiss Alps using a holographic imager. *Atmospheric Measurement Techniques*, 10(2):459–476, feb 2017. ISSN 1867-8548. doi: 10.5194/amt-10-459-2017.

Inga Beck and Markus Neumann. The Environmental Research Station Schneefernerhaus. In *EGU General Assembly Conference Abstracts*, page 21235, 2020.

Guus Bertens, Gholamhossein Bagheri, H Xu, Eberhard Bodenschatz, and J Moláček. In situ cloud particle tracking experiment. *Review of Scientific Instruments*, 92(12):125105, 2021.

Gregory P. Bewley, Ewe Wei Saw, and Eberhard Bodenschatz. Observation of the sling effect. *New Journal of Physics*, 15, aug 2013. ISSN 13672630. doi: 10.1088/1367-2630/15/8/083051.

E Bodenschatz, S P Malinowski, R A Shaw, and F Stratmann. Can we understand clouds without turbulence? *Science*, 327:970–971, 2010. ISSN 0036-8075. doi: 10.1126/science.1185138. URL `https://science.sciencemag.org/content/327/5968/970`.

R. Bordás, Ch Roloff, D. Thévenin, and R. A. Shaw. Experimental determination of droplet collision rates in turbulence. *New Journal of Physics*, 15(4):045010, apr 2013. ISSN 13672630. doi: 10.1088/1367-2630/15/4/045010.

Jean Louis Brenguier, Thierry Bourrianne, Afranio Araujo De Coelho, Jacques Isbert, Robert Peytavi, Dominique Trevarin, and Perry Weschler. Improvements of droplet size distribution measurements with the fast-FSSP (Forward Scattering Spectrometer Probe). *Journal of Atmospheric and Oceanic Technology*, 15(5):1077–1090, oct 1998. ISSN 07390572. doi: 10.1175/1520-0426(1998).

Britannica. URL `https://www.britannica.com/science/in-situ-measurement`.

F. Burnet and J. L. Brenguier. Comparison between standard and modified forward scattering spectrometer probes during the small cumulus microphysics study. 19:1516–1531, 2002.

R Castrejón-García, JR Castrejón-Pita, GD Martin, and IM Hutchings. The shadowgraph imaging technique and its modern application to fluid jets and drops. *Revista mexicana de física*, 57(3):266–275, 2011.

P. Y. Chuang, E. W. Saw, J. D. Small, R. A. Shaw, C. M. Sipperley, G. A. Payne, and W. D. Bachalo. Airborne Phase Doppler Interferometry for Cloud Microphysical Measurements. *Aerosol Science and Technology*, 42 (8):685–703, jun 2008. ISSN 0278-6826. doi: 10.1080/02786820802232956.

William A. Cooper. Effects of Coincidence on Measurements with a Forward Scattering Spectrometer Probe. *Journal of Atmospheric and Oceanic Technology*, 5(6):823–832, dec 1988. ISSN 0739-0572. doi: 10.1175/1520-0426(1988).

Afrânio de Araújo Coelho, Jean Louis Brenguier, and Thierry Perrin. Droplet spectra measurements with the FSSP-100. Part I: Low droplet concentration measurements. *Journal of Atmospheric and Oceanic Technology*, 22 (11):1748–1755, nov 2005. ISSN 07390572. doi: 10.1175/JTECH1817.1.

N. Desai, S. Glienke, J. Fugal, and R. A. Shaw. Search for Microphysical Signatures of Stochastic Condensation in Marine Boundary Layer Clouds Using Airborne Digital Holography. *Journal of Geophysical Research: Atmospheres*, 2019. ISSN 21698996. doi: 10.1029/2018JD029033.

B. J. Devenish, P. Bartello, J. L. Brenguier, L. R. Collins, W. W. Grabowski, R. H.A. Ijzermans, S. P. Malinowski, M. W. Reeks, J. C. Vassilicos, L. P. Wang, and Z. Warhaft. Droplet growth in warm turbulent clouds, jul 2012. ISSN 00359009.

Hongxu Duan, Francisco J. Romay, Cheng Li, Amir Naqwi, Weiwei Deng, and Benjamin Y. H. Liu. Generation of monodisperse aerosols by combining aerodynamic flow-focusing and mechanical perturbation. *Aerosol Science and Technology*, 50(1):17–25, jan 2016. ISSN 0278-6826. doi: 10.1080/02786826.2015.1123213.

Luca Egli, Tobias Jonas, Thomas Grünewald, Michael Schirmer, and Paolo Burlando. Dynamics of snow ablation in a small alpine catchment observed by repeated terrestrial laser scans. *Hydrological Processes*, 26:1574–1585, 5 2012. ISSN 08856087. doi: 10.1002/hyp.8244. URL `http://www.riegl.`

EOL. https://www.eol.ucar.edu/instruments/forward-scattering-spectrometer-probe-model-100, a. Accessed: 2022-08-16.

Earth Observation Laboratory EOL. https://www.eol.ucar.edu/instruments/two-dimensional-optical-array-cloud-probe, b. Accessed: 2022-07-10.

Jacob P. Fugal, Timothy J. Schulz, and Raymond A. Shaw. Practical methods for automated reconstruction and characterization of particles in digital in-line holograms. *Measurement Science and Technology*, 20(7):75501, may 2009. ISSN 13616501. doi: 10.1088/0957-0233/20/7/075501.

H. Gerber, B. G. Arends, and A. S. Ackerman. New microphysics sensor for aircraft use. *Atmospheric Research*, 1994. ISSN 01698095. doi: 10.1016/0169-8095(94)90001-9.

H. Gerber, Glendon Frick, and Alfred R. Rodi. Ground-based FSSP and PVM measurements of liquid water content. *Journal of Atmospheric and Oceanic Technology*, 16(8):1143–1149, aug 1999. ISSN 07390572. doi: 10.1175/1520-0426(1999).

H Gerber, Szymon P Malinowski, and Haflidi Jonsson. Evaporative and radiative cooling in post stratocumulus. *Journal of the Atmospheric Sciences*, 73:3877 – 3884, 2016. doi: 10.1175/JAS-D-16-0023.1. URL https://journals.ametsoc.org/view/journals/atsc/73/10/jas-d-16-0023.1.xml.

Homa Ghasemifard, Felix R. Vogel, Ye Yuan, Marvin Luepke, Jia Chen, Ludwig Ries, Michael Leuchner, Christian Schunk, Sanam Noreen Vardag, and Annette Menzel. Pollution events at the high-altitude mountain site Zugspitze-Schneefernerhaus (2670 m a.s.l.), Germany. *Atmosphere*, 2019. ISSN 20734433. doi: 10.3390/atmos10060330.

A. Glen and S. D. Brooks. A new method for measuring optical scattering properties of atmospherically relevant dusts using the Cloud and Aerosol Spectrometer with Polarization (CASPOL). *Atmospheric Chemistry and Physics*, 13(3):1345–1356, feb 2013. ISSN 1680-7324. doi: 10.5194/acp-13-1345-2013.

S. Glienke, A. Kostinski, J. Fugal, R. A. Shaw, S. Borrmann, and J. Stith. Cloud droplets to drizzle: Contribution of transition drops to microphysical and optical properties of marine stratocumulus clouds. *Geophysical Research Letters*, 2017. ISSN 19448007. doi: 10.1002/2017GL074430.

Google Earth. https://earth.google.com/web/search/Schneefernerhaus/. Accessed: 2022-08-18.

Wojciech W. Grabowski and Lian-Ping Wang. Growth of Cloud Droplets in a Turbulent Environment. *Annual Review of Fluid Mechanics*, 45(1):293–324, jan 2013. ISSN 0066-4189. doi: 10.1146/annurev-fluid-011212-140750.

Danièle Hauser, Paul Amayenc, Bernard Nutten, and Philippe Waldteufel. A new optical instrument for simultaneous measurement of raindrop diameter and fall speed distributions. *Journal of Atmospheric and Oceanic Technology*, 1:256–269, 1984. doi: 10.1175/1520-0426(1984)001⟨0256:ANOIFS⟩2.0.CO;2. URL https://journals.ametsoc.org/view/journals/atot/1/3/1520-0426_1984_001_0256_anoifs_2_0_co_2.xml.

J. Henneberger, J. P. Fugal, O. Stetzer, and U. Lohmann. HOLIMO II: a digital holographic instrument for ground-based in situ observations of microphysical properties of mixed-phase clouds. *Atmospheric Measurement Techniques*, 6(11):2975–2987, nov 2013. ISSN 1867-8548. doi: 10.5194/amt-6-2975-2013.

IGF-UW-a. URL https://www.igf.fuw.edu.pl/en/instruments/instrument/doppler-wind-lidar-halo-na-stacji-cloudnet-w\protect\@normalcr\relax-warszawie-rs-lab-since-2021-d-37450-821/.

IGF-UW-b. URL https://www.igf.fuw.edu.pl/en/instruments/instrument/microwave-radiometer-hatpro-g2-at-the-cloudnet\protect\@normalcr\relax-site-in-warsaw-rs-lab-since-2019-e-450-8921/.

Joël Jaffrain and Alexis Berne. Experimental quantification of the sampling uncertainty associated with measurements from parsivel disdrometers. *Journal of Hydrometeorology*, 12:352–370, 2011. doi: 10.1175/2010JHM1244.1. URL https://journals.ametsoc.org/view/journals/hydr/12/3/2010jhm1244_1.xml.

Bogumił Jakubiak, Paweł Licznar, and Szymon P. Malinowski. Rainfall estimates from radar vs. raingauge measurements. warsaw case study. *Environment Protection Engineering*, 40:159–170, 2014. ISSN 03248828. doi: 10.5277/epe140212.

I Jen-La Plante, Y Ma, K Nurowska, H Gerber, D Khelif, K Karpinska, M Kopec, W Kumala, and S Malinowski. Physics of stratocumulus top (post): turbulence characteristics. *Atmospheric Chemistry and Physics*, 16:9711–9725, 2016. doi: 10.5194/acp-16-9711-2016. URL https://acp.copernicus.org/articles/16/9711/2016/.

J. Joss and A. Waldvogel. Ein spektrograph für niederschlagstropfen mit automatischer auswertung. *Pure and Applied Geophysics PAGEOPH*, 68: 240–246, 12 1967. ISSN 00334553. doi: 10.1007/BF00874898. URL `https://link.springer.com/article/10.1007/BF00874898`.

Ville A Kaikkonen, Eero O Molkoselkä, and Anssi J Mäkynen. A rotating holographic imager for stationary cloud droplet and ice crystal measurements. *Optical Review*, 27. doi: 10.1007/s10043-020-00583-y.

Julian T. Kashdan, John S. Shrimpton, and Adam Whybrew. Two-Phase Flow Characterization by Automated Digital Image Analysis. Part 1: Fundamental Principles and Calibration of the Technique. *Particle & Particle Systems Characterization*, 20(6):387–397, dec 2003. ISSN 09340866. doi: 10.1002/ppsc.200300897.

Julian T. Kashdan, John S. Shrimpton, and Adam Whybrew. Two-Phase Flow Characterization by Automated Digital Image Analysis. Part 2: Application of PDIA for Sizing Sprays. *Particle & Particle Systems Characterization*, 21(1):15–23, may 2004. ISSN 09340866. doi: 10.1002/ppsc.200400898.

Julian T. Kashdan, John S. Shrimpton, and Adam Whybrew. A digital image analysis technique for quantitative characterisation of high-speed sprays. *Optics and Lasers in Engineering*, 2007. ISSN 01438166. doi: 10.1016/j.optlaseng.2006.03.006.

Lisa Klanner, Thomas Trickl, and Hannes Vogelmann. Water-vapour measurements up to the lower stratosphere—the high power raman lidar at the schneefernerhaus. In *EPJ Web of Conferences*, volume 176, page 1026. EDP Sciences, 2018.

Robert G Knollenberg. The optical array: An alternative to scattering or extinction for airborne particle size determination. *Journal of Applied Meteorology (1962-1982)*, pages 86–103, 1970.

Piotr M. Korczyk, Tomasz A. Kowalewski, and Szymon P. Malinowski. Turbulent mixing of clouds with the environment: Small scale two phase evaporating flow investigated in a laboratory by particle image velocimetry. *Physica D: Nonlinear Phenomena*, 241(3):288–296, feb 2012. ISSN 01672789. doi: 10.1016/j.physd.2011.11.003.

Anton Kruger and Witold F Krajewski. Two-dimensional video disdrometer: A description. *Journal of Atmospheric and Oceanic Technology*, 19:602–617, 2002. doi: 10.1175/1520-0426(2002)019⟨0602:TDVDAD⟩2.0.CO;2. URL https://journals.ametsoc.org/view/journals/atot/19/5/1520-0426_2002_019_0602_tdvdad_2_0_co_2.xml.

M. Shyam Kumar, S. R. Chakravarthy, and Manikandan Mathur. Optimum air turbulence intensity for polydisperse droplet size growth. *Physical Review Fluids*, 4(7):074607, jul 2019. ISSN 2469990X. doi: 10.1103/PhysRevFluids.4.074607.

S. Lance, C. A. Brock, D. Rogers, and J. A. Gordon. Water droplet calibration of the Cloud Droplet Probe (CDP) and in-flight performance in liquid, ice and mixed-phase clouds during ARCPAC. *Atmospheric Measurement Techniques*, 3(6):1683–1706, dec 2010. ISSN 1867-8548. doi: 10.5194/amt-3-1683-2010.

Sara Lance. Coincidence errors in a cloud droplet probe (CDP) and a cloud and aerosol spectrometer (CAS), and the improved performance of a modified CDP. *Journal of Atmospheric and Oceanic Technology*, 29(10):1532–1541, oct 2012. ISSN 07390572. doi: 10.1175/JTECH-D-11-00208.1.

Michael L. Larsen and Raymond A. Shaw. A method for computing the three-dimensional radial distribution function of cloud particles from holographic images. *Atmospheric Measurement Techniques*, 11(7):4261–4272, jul 2018. ISSN 1867-8548. doi: 10.5194/amt-11-4261-2018.

R. Paul Lawson, Brad A. Baker, Carl G. Schmitt, and T. L. Jensen. An overview of microphysical properties of Arctic clouds observed in May and July 1998 during FIRE ACE, jul 2001. ISSN 01480227. URL https://agupubs.onlinelibrary.wiley.com/doi/full/10.1029/2000JD900789https://agupubs.onlinelibrary.wiley.com/doi/abs/10.1029/2000JD900789https://agupubs.onlinelibrary.wiley.com/doi/10.1029/2000JD900789.

R Paul Lawson, Darren O'Connor, Patrick Zmarzly, Kim Weaver, Brad Baker, Qixu Mo, and Haflidi Jonsson. The 2d-s (stereo) probe: Design and preliminary tests of a new airborne, high-speed, high-resolution particle imaging probe. *Journal of Atmospheric and Oceanic Technology*, 23(11):1462–1477, 2006.

R. Paul Lawson, Eric Jensen, David L. Mitchell, Brad Baker, Qixu Mo, and Bryan Pilson. Microphysical and radiative properties of tropical clouds investigated in TC4 and NAMMA. *Journal of Geophysical Research*, 115(D10), aug 2010. ISSN 0148-0227. doi: 10.1029/2009jd013017.

Miao Ling Lu, William C. Conant, Haflidi H. Jonsson, Varuntida Varutbangkul, Richard C. Flagan, and John H. Seinfeld. The Marine Stratus/Stratocumulus Experiment (MASE): Aerosol-cloud relationships in marine stratocumulus. *Journal of Geophysical Research Atmospheres*, 2007. ISSN 01480227. doi: 10.1029/2006JD007985.

Martin Löffler-Mang and Ulrich Blahak. Estimation of the equivalent radar reflectivity factor from measured snow size spectra. *Journal of Applied Meteorology*, 40:843–849, 2001. doi: 10.1175/1520-0450(2001)040⟨0843:EOTERR⟩2.0.CO;2. URL https://journals.ametsoc.org/view/journals/apme/40/4/1520-0450_2001_040_0843_eoterr_2.0.co_2.xml.

Martin Löffler-Mang and Jürg Joss. An optical disdrometer for measuring size and velocity of hydrometeors. *Journal of Atmospheric and Oceanic Technology*, 17:130–139, 2000. doi: 10.1175/1520-0426(2000)017⟨0130:AODFMS⟩2.0.CO;2. URL https://journals.ametsoc.org/view/journals/atot/17/2/1520-0426_2000_017_0130_aodfms_2_0_co_2.xml.

K M Markowicz, O Zawadzka, M Posyniak, and J Uscka-Kowalkowska. Long-term variability of aerosol optical depth in the tatra mountain region of central europe. *Journal of Geophysical Research: Atmospheres*, 124:3464–3475, 2019. doi: https://doi.org/10.1029/2018JD028846. URL https://agupubs.onlinelibrary.wiley.com/doi/abs/10.1029/2018JD028846.

Krzysztof M Markowicz and Michał T Chiliński. Evaluation of two low-cost optical particle counters for the measurement of ambient aerosol scattering coefficient and Ångström exponent. *Sensors*, 20, 2020. ISSN 1424-8220. doi: 10.3390/s20092617. URL https://www.mdpi.com/1424-8220/20/9/2617.

Greg M. McFarquhar, Junshik Um, Matt Freer, Darrel Baumgardner, Gregory L. Kok, and Gerald Mace. Importance of small ice crystals to cirrus properties: Observations from the Tropical Warm Pool International Cloud Experiment (TWP-ICE). *Geophysical Research Letters*, 34(13), jul 2007. ISSN 00948276. doi: 10.1029/2007GL029865.

M. Mohammadi, J. L. Nowak, G. Bertens, J. Moláček, W. Kumala, and S. P. Malinowski. Cloud microphysical measurements at a mountain observatory: comparison between shadowgraph imaging and phase doppler interferometry. *Atmospheric Measurement Techniques*, 15:965–985, 2022a.

doi: 10.5194/amt-15-965-2022. URL https://amt.copernicus.org/articles/15/965/2022/amt-15-965-2022.html.

M. Mohammadi, J. L. Nowak, and S. P. Malinowski. Microphysical measurements of hydrometeors using shadowgraph imaging technique. *J. Phys.: Conf. Ser.*, page Accepted for publication, 2022b.

Eero O. Molkoselkä, Ville A. Kaikkonen, and Anssi J. Mäkynen. Measuring atmospheric icing rate in mixed-phase clouds using filtered particle data. *IEEE Transactions on Instrumentation and Measurement*, 70:1–8, 2021. doi: 10.1109/TIM.2020.3035562.

MTU. https://www.mtu.edu/news/2015/10/new-holodec-study-science-using-holography-better-understand-clouds.html. Accessed: 2022-08-17.

NASA. URL https://www.nasa.gov/feature/jpl/cloudsat-exits-the-a-train.

Jakub L. Nowak, Moein Mohammadi, and Szymon P. Malinowski. Applicability of the visisize d30 shadowgraph system for cloud microphysical measurements. *Atmospheric Measurement Techniques*, 2021. ISSN 18678548. doi: 10.5194/amt-14-2615-2021.

K. Nurowska, M. Mohammadi, S. Malinowski, and K. Markowicz. Applicability of the low-cost optical particle counter opc-n3 for microphysical measurements of fog. *Atmospheric Measurement Techniques Discussions*, 2022:1–25, 2022. doi: 10.5194/amt-2022-269. URL https://amt.copernicus.org/preprints/amt-2022-269/.

OTT GmbH. https://www.ott.com/. Accessed: 2022-09-17.

Fabiola Ramelli, Alexander Beck, Jan Henneberger, and Ulrike Lohmann. Using a holographic imager on a tethered balloon system for microphysical observations of boundary layer clouds. *Atmospheric Measurement Techniques*, 13(2):925–939, feb 2020. ISSN 1867-8548. doi: 10.5194/amt-13-925-2020.

S. M.F. Raupach, H. J. Vössing, J. Curtius, and S. Borrmann. Digital crossed-beam holography for insitu imaging of atmospheric ice particles. *Journal of Optics A: Pure and Applied Optics*, 2006. ISSN 14644258. doi: 10.1088/1464-4258/8/9/014.

T. H. Raupach and A. Berne. Correction of raindrop size distributions measured by parsivel disdrometers, using a two-dimensional video disdrometer as a reference. *Atmospheric Measurement Techniques*, 8:343–365, 1 2015. ISSN 18678548. doi: 10.5194/amt-8-343-2015.

S. Risius, H. Xu, F. Di Lorenzo, H. Xi, H. Siebert, R. A. Shaw, and E. Bodenschatz. Schneefernerhaus as a mountain research station for clouds and turbulence. *Atmospheric Measurement Techniques*, 8(8):3209–3218, aug 2015. ISSN 1867-8548. doi: 10.5194/amt-8-3209-2015.

RPG GmbH. URL `https://www.radiometer-physics.de/products/microwave-remote-sensing-instruments/94-ghz-fmcw-doppler-cloud-radar/`.

Staffan Rydblom and Benny Thörnberg. Liquid water content and droplet sizing shadowgraph measuring system for wind turbine icing detection. *IEEE Sensors Journal*, 16(8):2714–2725, apr 2016. ISSN 1530437X. doi: 10.1109/JSEN.2016.2518653.

Christian Salles, Jean Poesen, and Daniel Sempere-Torres. Kinetic energy of rain and its functional relationship with intensity. *Journal of Hydrology*, 257:256–270, 2 2002. ISSN 00221694. doi: 10.1016/S0022-1694(01)00555-8.

Oliver Schlenczek. *Airborne and ground-based holographic measurement of hydrometeors in liquid-phase, mixed-phase and ice clouds*. Phd thesis, Johannes Gutenberg University in Mainz, 2017a.

Oliver Schlenczek, Jacob P. Fugal, Gary Lloyd, Keith N. Bower, Thomas W. Choularton, Michael Flynn, Jonathan Crosier, and Stephan Borrmann. Microphysical Properties of Ice Crystal Precipitation and Surface-Generated Ice Crystals in a High Alpine Environment in Switzerland. *Journal of Applied Meteorology and Climatology*, 56(2):433–453, feb 2017b. ISSN 15588432. doi: 10.1175/JAMC-D-16-0060.1.

schneefernerhaus.de. `https://schneefernerhaus.de/en/research-station/contact-and-informations/imagery/`. Accessed: 2022-08-18.

Gary S Settles. *Schlieren and shadowgraph techniques: visualizing phenomena in transparent media*. Springer Science & Business Media, 2001.

H. Siebert, R. A. Shaw, J. Ditas, T. Schmeissner, S. P. Malinowski, E. Bodenschatz, and H. Xu. High-resolution measurement of cloud microphysics and turbulence at a mountaintop station. *Atmospheric Mea-*

surement Techniques, 8(8):3219–3228, aug 2015. ISSN 1867-8548. doi: 10.5194/amt-8-3219-2015.

Holger Siebert and Ulrich Teichmann. Behaviour of an ultrasonic anemometer under cloudy conditions. *Boundary-Layer Meteorology*, 2000. ISSN 00068314. doi: 10.1023/A:1002446723575.

Holger Siebert, Harald Franke, Katrin Lehmann, Rolf Maser, Ewe Wei Saw, Dieter Schell, Raymond A Shaw, and Manfred Wendisch. Probing finescale dynamics and microphysics of clouds with helicopter-borne measurements. *Bulletin of the American Meteorological Society*, 87(12):1727–1738, 2006.

Holger Siebert, Kai-Erik Szodry, Ulrike Egerer, Birgit Wehner, Silvia Henning, Karine Chevalier, Janine Lückerath, Oliver Welz, Kay Weinhold, Felix Lauermann, Matthias Gottschalk, André Ehrlich, Manfred Wendisch, Paulo Fialho, Greg Roberts, Nithin Allwayin, Simeon Schum, Raymond A Shaw, Claudio Mazzoleni, Lynn Mazzoleni, Jakub L Nowak, Szymon P Malinowski, Katarzyna Karpinska, Wojciech Kumala, Dominika Czyzewska, Edward P Luke, Pavlos Kollias, Robert Wood, and Juan Pedro Mellado. Observations of aerosol, cloud, turbulence, and radiation properties at the top of the marine boundary layer over the eastern north atlantic ocean: The acores campaign. *Bulletin of the American Meteorological Society*, 102:E123 – E147, 2021. doi: 10.1175/BAMS-D-19-0191.1. URL https://journals.ametsoc.org/view/journals/bams/102/1/BAMS-D-19-0191.1.xml.

R. Sijs, S. Kooij, H. J. Holterman, J. Van De Zande, and D. Bonn. Drop size measurement techniques for sprays: Comparison of image analysis, phase doppler particle analysis, and laser diffraction. *AIP Advances*, 11: 15315, 1 2021. ISSN 21583226. doi: 10.1063/5.0018667. URL https://doi.org/10.1063/5.0018667.

SPEC Inc. http://www.specinc.com/. Accessed: 2022-07-10.

J. K. Spiegel, P. Zieger, N. Bukowiecki, E. Hammer, E. Weingartner, and W. Eugster. Evaluating the capabilities and uncertainties of droplet measurements for the fog droplet spectrometer (fm-100). *Atmospheric Measurement Techniques*, 5(9):2237–2260, 2012. doi: 10.5194/amt-5-2237-2012. URL https://amt.copernicus.org/articles/5/2237/2012/.

Jeffrey L. Stith, James E. Dye, Aaron Bansemer, Andrew J. Heymsfield, Cedric A. Grainger, Walter A. Petersen, and Robert Cifelli. Microphysical observations of tropical clouds. *Journal of Applied Meteorology*, 41(2):97–117, feb 2002. ISSN 08948763. doi: 10.1175/1520-0450(2002)041⟨0097:MOOTC⟩2.0.CO;2.

F. J. Tapiador, R. Checa, and M. De Castro. An experiment to measure the spatial variability of rain drop size distribution using sixteen laser disdrometers. *Geophysical Research Letters*, 37, 8 2010. ISSN 00948276. doi: 10.1029/2010GL044120. URL `https://agupubs.pericles-prod.literatumonline.com/doi/full/10.1029/2010GL044120https://agupubs.pericles-prod.literatumonline.com/doi/abs/10.1029/2010GL044120https://agupubs.onlinelibrary.wiley.com/doi/10.1029/2010GL044120`.

F Y Testik and Ana P Barros. Toward elucidating the microstructure of warm rainfall: A survey. *Reviews of Geophysics*, 45, 2007.

J. Testud, S. Oury, R. A. Black, P. Amayenc, and X. Dou. The concept of "normalized" distribution to describe raindrop spectra: A tool for cloud physics and cloud remote sensing. *Journal of Applied Meteorology*, 40:1118–1140, 2001. ISSN 08948763. doi: 10.1175/1520-0450(2001)040⟨1118:TCONDT⟩2.0.CO;2. URL `https://journals.ametsoc.org/view/journals/apme/40/6/1520-0450_2001_040_1118_tcondt_2.0.co_2.xml`.

P. Tiitta, A. Leskinen, V. A. Kaikkonen, E. O. Molkoselkä, A. J. Mäkynen, J. Joutsensaari, S. Calderon, S. Romakkaniemi, and M. Komppula. Intercomparison of holographic imaging and single-particle forward light scattering in situ measurements of liquid clouds in changing atmospheric conditions. *Atmospheric Measurement Techniques*, 15(9):2993–3009, 2022. doi: 10.5194/amt-15-2993-2022. URL `https://amt.copernicus.org/articles/15/2993/2022/`.

Ali Tokay, V N Bringi, M Schönhuber, G J Huang, D Hudak, D B Wolff, P G Bashor, W A Petersen, and G Skofornick-Jackson. Disdrometer derived zs relations in south central ontario, canada. pages 6–10, 2007.

Remko Uijlenhoet and Daniel Sempere Torres. Measurement and parameterization of rainfall microstructure. *Journal of Hydrology*, 328:1–7, 8 2006. ISSN 00221694. doi: 10.1016/j.jhydrol.2005.11.038.

C. W. Ulbrich. Natural variations in the analytical form of the raindrop size distribution. *Journal of Climate & Applied Meteorology*, 22, 1983. ISSN 0733-3021. doi: 10.1175/1520-0450(1983)022⟨1764:NVITAF⟩2.0.CO;2.

Vice. https://www.vice.com/en/article/d73a4y/this-airborne-holodec-is-a-3d-microscope-for-clouds. Accessed: 2022-08-17.

Dongxiang Wang, Iwona S Stachlewska, Xiaoquan Song, Birgit Heese, and Anca Nemuc. Variability of the boundary layer over an urban continental site based on 10 years of active remote sensing observations in warsaw. *Remote Sensing*, 12, 2020. ISSN 2072-4292. doi: 10.3390/rs12020340. URL https://www.mdpi.com/2072-4292/12/2/340.

Zhuoru Wang, Ka Lok Chan, Klaus-Peter Heue, Adrian Doicu, Thomas Wagner, Robert Holla, and Matthias Wiegner. A MAX-DOAS aerosol profile retrieval algorithm for high altitude measurements: application to measurements at Schneefernerhaus (UFS), Germany. *Atmospheric Measurement Techniques Discussions*, 2019. ISSN 1867-1381. doi: 10.5194/amt-2019-204.

V. Wirth, M. Kristen, M. Leschner, J. Reuder, and J. H. Schween. Banner clouds observed at Mount Zugspitze. *Atmospheric Chemistry and Physics*, 2012. ISSN 16807316. doi: 10.5194/acp-12-3611-2012.

Sarah Woods, R. Paul Lawson, Eric Jensen, T. P. Bui, Troy Thornberry, Andrew Rollins, Leonhard Pfister, and Melody Avery. Microphysical Properties of Tropical Tropopause Layer Cirrus. *Journal of Geophysical Research: Atmospheres*, 123(11):6053–6069, jun 2018. ISSN 2169897X. doi: 10.1029/2017JD028068.

Sandra E Yuter, David E Kingsmill, Louisa B Nance, and Martin Löffler-Mang. Observations of precipitation size and fall speed characteristics within coexisting rain and wet snow. *Journal of Applied Meteorology and Climatology*, 45:1450–1464, 2006. doi: 10.1175/JAM2406.1. URL https://journals.ametsoc.org/view/journals/apme/45/10/jam2406.1.xml.

Olga Zawadzka-Manko, Iwona S Stachlewska, and Krzysztof M Markowicz. Near-real-time application of seviri aerosol optical depth algorithm. *Remote Sensing*, 12, 2020. ISSN 2072-4292. doi: 10.3390/rs12091481. URL https://www.mdpi.com/2072-4292/12/9/1481.